

# Ultrafast drop impact dynamics on unheated and heated flat surfaces

by

Yichi Zhang

A thesis submitted in partial fulfillment of the requirements for the degree of

Master of Science

Department of Mechanical Engineering

University of Alberta

© Yichi Zhang, 2021

# Abstract

Motivated by relevant applications in spray cooling, coating, and inkjet printing, droplet impact dynamics on a solid surface is investigated both numerically and experimentally by varying several major control parameters such as impact velocity, contact angle, and surface temperature.

First, computational fluid dynamics (CFD) simulations are carried out to study a water droplet impact onto a flat and unheated surface with different surface wettability, e.g., hydrophilic, hydrophobic, and ultrahydrophobic surfaces parameterized using the droplet's static contact angle,  $\theta_w$ . In the CFD study, the governing equations consist of the Navier-Stokes equations with a level-set method used to track the interface between the two fluid phases: water and air. The corresponding Weber ( $We$ ) number, defined as the droplet's kinetic to surface energy ratio, ranges from 4 to 510. The numerical model successfully reproduces the experimental impact outcomes with good agreement, especially in the low  $We$  ( $< 30$ ) regime. The primary impact outcomes include spreading, rebound, jetting, and splashing as impact velocity  $V_I$  is increased. Most of the simulation results show a universal scaling law of maximum spreading factor,  $\beta_{\max} \sim We^{1/4}$ , especially on hydrophobic and ultrahydrophobic surfaces. The slip length  $b$ , accounting for the frictional force exerted by a flat solid surface on a droplet, is found to be a key factor controlling dissipation and thus impact dynamics and should be varied with surface wettability. As  $V_I$  increases, the generation of entrapped air bubbles, jetting, and splashing occur and are caused by the interplay between pressure variation, droplet deformation, and surface tension.

Second, we carry out experiments of water drop impact on a heated flat surface using

a high-speed camera, an Infrared (IR) camera, and thermocouples to record both ultrafast drop dynamics and temperature field. As the increase of surface temperature  $T_s$  (100°C to 450°C) and  $We$  (1.6 to 129), four specific dynamical events are observed: spreading, totally rebound, spreading with atomization, and splashing break up with atomization. The Leidenfrost effect, with an insulating vapor layer formed underneath the droplet, is observed at high  $T_s$  ( $> 350^\circ\text{C}$ ) but low  $We$  ( $< 10$ ). The droplet temperature is analyzed with the IR camera results and shows good agreement with a theoretical model at a low surface temperature region ( $T_s \approx 100^\circ\text{C}$ ). The surface temperature changing  $|\Delta T_s|$ , i.e., the surface cooling rate by impacting droplet, is analyzed from the thermocouple results.  $|\Delta T_s|$  is increased in low- $T_s$  regime but decreased in high- $T_s$  regime. Spreading is the typical event at low- $T_s$ , with similar contact area, higher  $T_s$  leads larger  $|\Delta T_s|$ . A total droplet rebound observed at high- $T_s$  regime with a vapor film underneath avoids droplet directly contact with the surface; therefore, the change of surface temperature  $|\Delta T_s|$  is small.

Our simulation and experimental results demonstrate the importance of surface wettability on high-speed drop impact dynamics on a flat and unheated surface. Furthermore, our experimental results of water drop impact on a heated, flat surface reveal the interplay of both fluid motion and heat transfer on the drop impact outcomes and the dynamic Leidenfrost point depending on  $We$ .

# Preface

The majority of the experimental and numerical work presented in this thesis was performed by Yichi Zhang under the supervision of Professor Peichun Amy Tsai. The experimental work presented in Chapter 3 and 4 is done through collaboration with Lihui Liu.

Chapter 2 is based on a manuscript recently submitted to an international journal: Yichi Zhang\*, Yukai Ren\*, Lihui Liu, and Peichun Amy Tsai, “Drop Impact Dynamics on Solid Surfaces of Different Wettability,” submitted (2021). (\*equally-contributing first authors)

Chapter 3 - 4 results are based on a manuscript, Yichi Zhang, Lihui Liu, and Peichun Amy Tsai, “Ultrafast drop dynamics and temperature variation during a water droplet impacting onto a heated flat surface,” in preparation (2021).

# Acknowledgements

I want to thank my supervisor, Dr. Peichun Amy Tsai, for giving me an opportunity to continue study and research at the University of Alberta. Her expertise, insight, and patience make me understand and gain various useful and professional skills, such as experimental designs, instrumentation, computational fluid dynamics, better ways to learn new things, critical thinking and analyses of data and results, and professional communications. I am grateful for her support and care in my studies, research, and life.

I am also thankful for the whole group of the Tsai Lab. The group is like a big family to me. Special thanks to Dr. Lihui liu and Yukai Ren, two previous visiting PhD students who collaborated with me on some projects. The year together also led to a strong friendship between us.

Finally, I want to thank my family for supporting me in studying abroad in Canada. I would not be where I am without their unconditional love.

# Contents

<b>Abstract</b>	<b>ii</b>
<b>Preface</b>	<b>iv</b>
<b>Acknowledgements</b>	<b>v</b>
<b>Contents</b>	<b>vi</b>
<b>List of Tables</b>	<b>ix</b>
<b>List of Figures</b>	<b>x</b>
<b>1 Introduction</b>	<b>1</b>
1.1 Research background and motivation . . . . .	1
1.2 Drop impact on unheated surfaces . . . . .	3
1.2.1 Spreading factor . . . . .	3
1.2.2 Splashing threshold . . . . .	7
1.2.3 Numerical simulations . . . . .	9
1.3 Drop impact on heated surface . . . . .	11
1.3.1 Experimental phase diagram . . . . .	11
1.3.2 Leidenfrost point . . . . .	12
1.3.3 Temperature change . . . . .	14
1.4 Overview of the thesis . . . . .	16

<b>2</b>	<b>Drop Impact Dynamics on Solid Surfaces of Different Wettability</b>	<b>17</b>
2.1	Introduction . . . . .	17
2.2	Numerical Simulation . . . . .	20
2.2.1	Mathematical Model . . . . .	20
2.2.2	Numerical Modeling . . . . .	23
2.2.3	Mesh-independence Examination . . . . .	24
2.2.4	Validation . . . . .	25
2.3	Results and Discussion . . . . .	26
2.3.1	Slip Length Analysis . . . . .	26
2.3.2	Effect of Impact Velocity . . . . .	28
2.3.3	Effect of wettability . . . . .	35
2.4	Conclusions . . . . .	39
<b>3</b>	<b>Drop Impact Dynamics on a Heated Surface</b>	<b>41</b>
3.1	Introduction . . . . .	41
3.2	Experimental . . . . .	41
3.3	Results and discussion . . . . .	44
3.3.1	High-speed-imaging results of drop impact dynamics . . . . .	44
3.3.2	High-speed IR recordings of drop impact dynamics . . . . .	47
3.4	Summary . . . . .	51
<b>4</b>	<b>Temperature Variation during Drop Impact on a Heated Surface</b>	<b>52</b>
4.1	Introduction . . . . .	52
4.2	Theoretical models . . . . .	53
4.2.1	Convective heat transfer model of a heating droplet when impacting on a heated surface . . . . .	53
4.3	Results and discussion . . . . .	55
4.3.1	Phase diagram of drop impact dynamics on a heated, flat surface . . . . .	56
4.3.2	Droplet contact diameter . . . . .	57

4.3.3	Droplet Temperature Change . . . . .	59
4.3.4	Surface temperature change . . . . .	60
4.4	Summary . . . . .	64
<b>5</b>	<b>Conclusions and Outlook</b>	<b>66</b>
5.1	Conclusions . . . . .	66
5.2	Future work . . . . .	68
	<b>References</b>	<b>70</b>

# List of Tables

- 1.1 Summary of various effects on possible drop impact outcomes, adapted from Rioboo et al. [15]. . . . . 4
- 1.2 Various models of spreading factor,  $\beta$ . . . . . 8
- 1.3 Summary of recent numerical simulations of water droplet impact on solid surfaces. . . . . 9
  
- 2.1 Summary of parameters for different mesh schemes. . . . . 24
  
- 3.1 Summary of IR camera measuring range and corresponding accuracy. . . . . 44

# List of Figures

1.1	Schematic of a liquid drop with a static contact angle $\theta$ , determined by the balance of three interfacial tensions with the Young's Eqn. (1.5). . . . .	3
1.2	Examples of six possible outcomes of drop impact on dry surfaces. The images are taken from Rioboo et al. [15] and adopted by Yarin. [6]. . . . .	4
1.3	Sketch of the vortical motion revealed by the presence of tracers inside the balloon. The image is from Clanet et al. [23]. . . . .	6
1.4	Prompt splash and corona splash pictured by Riboo et al. [15]. . . . .	8
1.5	Heat transfer regimes associated with a drop impinging a hot surface. The diagram is from Liang et al. [9]. . . . .	12
1.6	(a) Plain bubbles, and (b) pagoda-like bubbles in the bubble boiling regime. Pictures are from Liang et al. [9]. . . . .	12
1.7	Phase diagram for water droplet impact on a heated surface showing three separate regions: contact boiling regime (red solid diamonds), gentle film boiling regime (blue solid circles), and spraying film boiling regime (green solid squares). The diagram is from Tran et al. [66]. . . . .	13
1.8	Phase diagram of the impact outcomes of an ethanol droplet on a sapphire plate with varying surface temperature and Weber number. Four regimes are identified from the high-speed recordings: deposition (blue diamonds), bounce (green circles), contact-splash (orange squares), and film-splash (red triangles). The diagram is from Staat et al. [67]. . . . .	13

1.9	(a) Temperature distribution in the liquid drop obtained by 2cLIF imaging. (b) Temperature distribution at the solid surface measured by infrared thermography. Images are from Castanet et al. [87]. . . . .	15
2.1	Schematic of a droplet impacting at a speed $V_I$ on a solid surface. . . . .	20
2.2	Simulation results of dimensionless spreading factor, $\beta$ , changing with time for different mesh sizes, including normal, fine, finer, and extra fine mesh schemes examined. The mesh-independence check is done by comparing simulation results with experimental one (solid line) of a water droplet impacting on the hydrophilic surface of $\theta_w = 56^\circ$ , at $V_I = 0.35$ m/s. . . . .	25
2.3	Sequential images of experimental (left) and numerical (right) results of water drop impact at $V_I = 0.35$ m/s on a hydrophilic surface of $\theta_w = 56^\circ$ . Good agreement of drop shape varying in time is found. . . . .	26
2.4	Sequential simulation snapshots of water droplet impacting at $V_I = 0.35$ m/s on a wetting surface of $\theta_w = 56^\circ$ . Here, the slip-length values used are (a) $b = 5$ $\mu\text{m}$ , (b) $b = 1$ $\mu\text{m}$ (c) $b = 500$ nm, and (d) $b = 10$ nm, from top to bottom, respectively. Different $b$ values lead to distinct drop shapes and dynamics, transiting from a spreading (b-c) to a complete rebound (d) with decreasing $b$ . The length bars represent 1 mm. . . . .	26
2.5	The simulation results of spreading factor, $\beta$ , changing with time for different slip-length values ( $b$ ), compared with experimental results of a water droplet impacting on the hydrophilic surface of $\theta_w = 56^\circ$ at $V_I = 0.35$ m/s. . . . .	27
2.6	The simulation results of spreading factor, $\beta$ , changing in time with different slip-length values ( $b$ ), comparing with experimental results of a water droplet impacting on the wetted surface of $\theta_w = 110^\circ$ at $V_I = 0.5$ m/s. . . . .	28
2.7	The simulation results of spreading factor, $\beta$ , changing in time with different slip-length values ( $b$ ), comparing with experimental results of a water droplet impacting on the wetted surface of $\theta_w = 158^\circ$ at $V_I = 0.5$ m/s. . . . .	29

2.8	Phase diagram summarizing both experimental (open symbols) and simulation (filled symbols) results. The observed impact outcomes include spreading ( $\square$ , $\blacksquare$ ), complete rebound ( $\circ$ , $\bullet$ ), partial rebound ( $\triangle$ ), jetting ( $\diamond$ , $\blacklozenge$ ), and splashing ( $\star$ , $\blackstar$ ). . . . .	30
2.9	Sequential simulation snapshots of water droplet impacting on a hydrophilic flat surface (of $\theta_w = 56^\circ$ ) reveal different impact events: spreading in (a) and (b), jetting in (c), and splashing in (d), with increasing impact velocity $V_I$ , at (a) 0.35 m/s, (b) 1.0 m/s, (c) 2.0 m/s, and (d) 3.0 m/s, respectively. The length bars represent 2 mm. . . . .	31
2.10	Sequential simulation snapshots of water droplet impacting on a hydrophobic surface ( $\theta_w = 110^\circ$ ) reveal different impact events: spreading in (a), rebound in (b), jetting in (c) and splashing in (d)-(e), with increasing impact velocity $V_I$ , at (a) 0.5 m/s, (b) 1.0 m/s, (c) 2.0 m/s, (d) 2.5 m/s, and (e) 3.0 m/s. The length bars represent 2 mm. . . . .	31
2.11	Sequential simulation snapshots of water impacting on an ultrahydrophobic surface ( $\theta_w = 158^\circ$ ) reveal different impact events: rebound in (a) and (b), jetting in (c) and splashing in (d), with increasing impact velocity $V_I$ , at (a) 0.5 m/s, (b) 1.5 m/s, (c) 2.0 m/s, and (d) 2.5 m/s. The length bars represent 2 mm. . . . .	32
2.12	The pressure field (rainbow color) and normalized velocity vectors (white arrow) simulated for drop impact on ultrahydrophobic surface ( $\theta_w = 158^\circ$ ) with $V_I = 0.5$ m/s at different time (a) 5 ms, (b) 9 ms, (c) 13 ms, and (d) 14 ms. The unit of pressure is Pascal (Pa). . . . .	32
2.13	The pressure field (rainbow color) and normalized velocity vectors (white arrow) simulated of drop impact on ultrahydrophobic surface ( $\theta_w = 158^\circ$ ) with $V_I = 2.0$ m/s at different time (a) 6 ms, (b) 7 ms, (c) 8 ms, and (d) 9 ms. The unit of pressure is Pascal (Pa). . . . .	34

2.14	The pressure field (rainbow color) and normalized velocity vectors (white arrow) simulated of drop impact on ultrahydrophobic surface ( $\theta_w = 158^\circ$ ) with $V_I = 2.5$ m/s at different time (a) 1 ms, (b) 1.5 ms, (c) 2 ms, and (d) 3 ms. The unit of pressure is Pascal (Pa). . . . .	34
2.15	Sequential numerical snapshots of a falling droplet evolution at $V_I = 0.5$ m/s on surfaces with different wetting contact angles: (a) $\theta_w = 56^\circ$ , (b) $\theta_w = 110^\circ$ , (c) $\theta_w = 158^\circ$ . For different $\theta_w$ , their corresponding optimal slip length values have been investigated and subsequently used, with (a) $b = 500$ nm, (b) $b = 100$ nm, (c) $b = 10$ nm for $\theta_w = 56^\circ, 110^\circ$ , and $158^\circ$ , respectively. The length bars represent 1 mm. . . . .	36
2.16	The simulation results of spreading factor, $\beta$ , changing in time ( $t$ ) for different surface wettability ( $\theta_w$ ), under low and high Weber number situations of (a) $We = 6.9$ and (b) $We = 398$ . . . . .	37
2.17	The relation between the maximum spreading factor, $\beta_{max}$ , and $We$ for different surfaces. . . . .	38
3.1	(a) Schematic experimental setup of temperature measurements during drop impact on a heated surface. (b) Embedded thermocouple position in glass. . . . .	42
3.2	Sequential high-speed snapshots of water drop impacting at $We = 1.6$ on a flat, heated glass surface. The surface temperature is increased from top to bottom, with (a) $T_s = 100^\circ\text{C}$ , (b) $T_s = 200^\circ\text{C}$ , (c) $T_s = 350^\circ\text{C}$ and (d) $T_s = 450^\circ\text{C}$ . The length bars represent 1 mm. . . . .	45
3.3	Sequential images of high-speed recordings of water drop impact at $We = 27$ on a heated surface. The surface temperature is increasing from top to bottom that, (a) $T_s = 100^\circ\text{C}$ , (b) $T_s = 200^\circ\text{C}$ , (c) $T_s = 350^\circ\text{C}$ and (d) $T_s = 450^\circ\text{C}$ . The length bars represent 1 mm. . . . .	46

3.4	Sequential images of high speed camera results of water drop impact at $We = 129$ , on heated surface. The surface temperature is increasing from top to bottom that, (a) $T_s = 100^\circ\text{C}$ , (b) $T_s = 200^\circ\text{C}$ , (c) $T_s = 350^\circ\text{C}$ and (d) $T_s = 450^\circ\text{C}$ . The length bars represent 1 mm. . . . .	46
3.5	Sequential images of high-speed IR results of water drop impact at $We = 1.6$ , on a heated glass surface. The surface temperature is increasing from top to bottom that, (a) $T_s = 100^\circ\text{C}$ , (b) $T_s = 200^\circ\text{C}$ , (c) $T_s = 350^\circ\text{C}$ , and (d) $T_s = 450^\circ\text{C}$ . . . . .	49
3.6	Sequential images of IR results of water drop impact at $We = 27$ , on heated surface. The surface temperature is increasing from top to bottom that, (a) $T_s = 100^\circ\text{C}$ , (b) $T_s = 200^\circ\text{C}$ , (c) $T_s = 350^\circ\text{C}$ and (d) $T_s = 450^\circ\text{C}$ . . . . .	50
3.7	Sequential images of high-speed IR results of water drop impact at $We = 129$ , on a flat, heated glass surface. The surface temperature is increasing from top to bottom: (a) $T_s = 100^\circ\text{C}$ , (b) $T_s = 200^\circ\text{C}$ , (c) $T_s = 350^\circ\text{C}$ , and (d) $T_s = 450^\circ\text{C}$ . . . . .	50
4.1	Schematic diagram of droplet spreading on a heated surface. . . . .	54
4.2	Phase diagram summarizing the dynamic events of drop impact on a heated flat surface. Four typical events are observed and shown on the right: spreading (■), totally rebound (▲), spreading with atomization (●), and splashing breakup with atomization (▼) (from bottom to top). . . . .	57
4.3	Time evolution of contact diameter $d_c$ for different $We$ , (a) $We = 1.6$ , (b) $We = 27$ and (c) $We = 129$ at surface temperature $T_s = 100^\circ\text{C}$ , $200^\circ\text{C}$ , $300^\circ\text{C}$ , $350^\circ\text{C}$ , $400^\circ\text{C}$ , and $450^\circ\text{C}$ respectively. . . . .	58
4.4	Time evolution of droplet temperature $T_d$ change for different $We$ , (a) $We = 1.6$ , (b) $We = 27$ and (c) $We = 129$ at surface temperature $T_s = 100^\circ\text{C}$ . . . . .	59
4.5	Time evolution of droplet temperature $T_d$ change for different $We$ , (a) $We = 1.6$ , (b) $We = 27$ and (c) $We = 129$ at surface temperature $T_s = 300^\circ\text{C}$ . . . . .	60

4.6	The surface temperature recorded by thermocouples at $T_s = 100^\circ\text{C}$ and $We = 1.6$ . . . . .	61
4.7	The surface temperature recorded by thermocouples at $T_s = 100^\circ\text{C}$ and $We = 129$ . . . . .	61
4.8	The surface temperature recorded by thermocouples at $T_s = 450^\circ\text{C}$ and $We = 1.6$ . . . . .	62
4.9	The surface temperature recorded by thermocouples at $T_s = 450^\circ\text{C}$ and $We = 129$ . . . . .	62
4.10	Surface temperature change in two seconds after drop impact on the surface at different setting temperature. The error bar represents standard error of experiments three times per condition. . . . .	63

# Chapter 1

## Introduction

### 1.1 Research background and motivation

Drop impact on a solid surface is a ubiquitous problem that can be found in various natural phenomenon and industrial applications, such as raindrop, coating [1], spray cooling [2], metallurgy [3], and ink-jet printing [4]. Drop impact also plays a vital role in fire suppression application. Both drop impact dynamics and heat transfer during the process influence the efficiency of fire extinguishment [5]. Generally, multiple control parameters influence the drop impact dynamics on a solid surface. The interplay between the droplet, solid, and surrounding gas can generate surprising and intriguing impact dynamics. Hence, various experiments have shown several parameters and properties of the droplet (e.g., density, viscosity, size, and impact velocity), solid surface (such as wettability, roughness, structures, and temperature), and surrounding gas (e.g., pressure) affect the drop impact outcomes [6, 7, 8, 9].

Some dimensionless numbers therefore are commonly used to characterize drop impact parameters and outcomes, namely the Reynolds number ( $Re$ ), Weber number ( $We$ ), Capillary number ( $Ca$ ), and Ohnesorge number ( $Oh$ ) [7]. The Reynolds number ( $Re$ ) characterizes the inertia to viscous effect and is defined as:

$$Re = \frac{\rho U D}{\mu}, \quad (1.1)$$

where  $\rho$ ,  $U$ ,  $D$  and  $\mu$  represent the liquid density, impact velocity, droplet diameter, and dynamic viscosity, respectively. The Weber number ( $We$ ) compares the droplet kinetic to surface energy, defined as:

$$We = \frac{\rho U^2 D}{\sigma}, \quad (1.2)$$

where  $\sigma$  represents surface tension. The Capillary number ( $Ca$ ) relates viscous force to surface tension and is defined as:

$$Ca = \frac{\mu U}{\sigma}. \quad (1.3)$$

Finally, the Ohnesorge number ( $Oh$ ) compares viscous to inertia and surface tension forces:

$$Oh = \frac{\sqrt{We}}{Re} = \frac{\mu}{\sqrt{\rho \sigma D}}. \quad (1.4)$$

In addition, surface wettability is a typical term to describe the interaction between liquid and solid surfaces. Wettability is often characterized by measuring the water droplet's contact angle ( $\theta$ ) on the solid surface of interest. Small contact angles ( $< 90^\circ$ ) correspond to high wettability and vice versa [10]. The static contact angle ( $\theta_s$ ) can be experimentally measured by a force balance between various interfacial tensions at the three-phase contact line, modeled by Young in 1805 [11, 12]. Young [11] proposed that a balance of interfacial energies determines the contact angle:

$$\gamma_{SV} = \gamma_{SL} + \gamma_{LV} \cos \theta, \quad (1.5)$$

where  $\gamma_{SV}$ ,  $\gamma_{SL}$  and  $\gamma_{LV}$  are the solid-vapor (SV), solid-liquid (SL) and liquid-vapor (LV) interfacial force per unit length of the contact line, respectively, and  $\theta$  is the contact angle [11, 13], shown in Fig. 1.1. For water droplet, the surface is hydrophilic when the contact angle is less than  $90^\circ$ . On the contrary, the surface wettability is hydrophobic when  $\theta > 90^\circ$ . A surface is superhydrophobic when  $\theta > 150^\circ$ , with a small contact angle hysteresis [8].

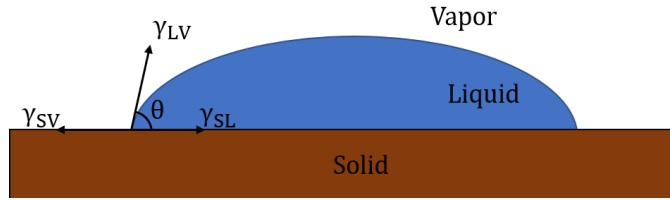


Figure 1.1. Schematic of a liquid drop with a static contact angle  $\theta$ , determined by the balance of three interfacial tensions with the Young's Eqn. (1.5).

## 1.2 Drop impact on unheated surfaces

Due to various applications in different fields and several complex parameters to control impact dynamics, the topic of drop impact has attracted numerous studies over the decades. The earliest systematic experiments date back when Worthington (1877) recorded water, alcohol, mercury, and milk droplets impacting solid surfaces [14]. With the development of computers and cameras, researchers have recorded the whole impacting process at high speed and built numerical models to simulate impact dynamics. We will review literature results regarding drop impact dynamics below.

When a droplet impacts an unheated solid surface, Rioboo et al. [15] demonstrated six possible outcomes: deposition, prompt splash, corona splash, receding break-up, partial rebound, and complete rebound (see Fig. 1.2). These drop impact outcomes depend on several factors of droplet parameters (e.g., liquid density, viscosity, surface tension, droplet size, and impact velocity) from the surface side, like material, roughness, structure, and surface temperature [6, 7]. Rioboo et al. also briefly summarized the effect of some parameters on the impact dynamics. For example, the increase of impact velocity would reduce the possibility of spreading but increase it of a splash, break up and rebound [15], as shown in Table. 1.1.

### 1.2.1 Spreading factor

During the simple spreading process, the drop spreads on the surface until it reaches the maximum radius. Hence, the maximum spreading radius (or diameter) becomes an important

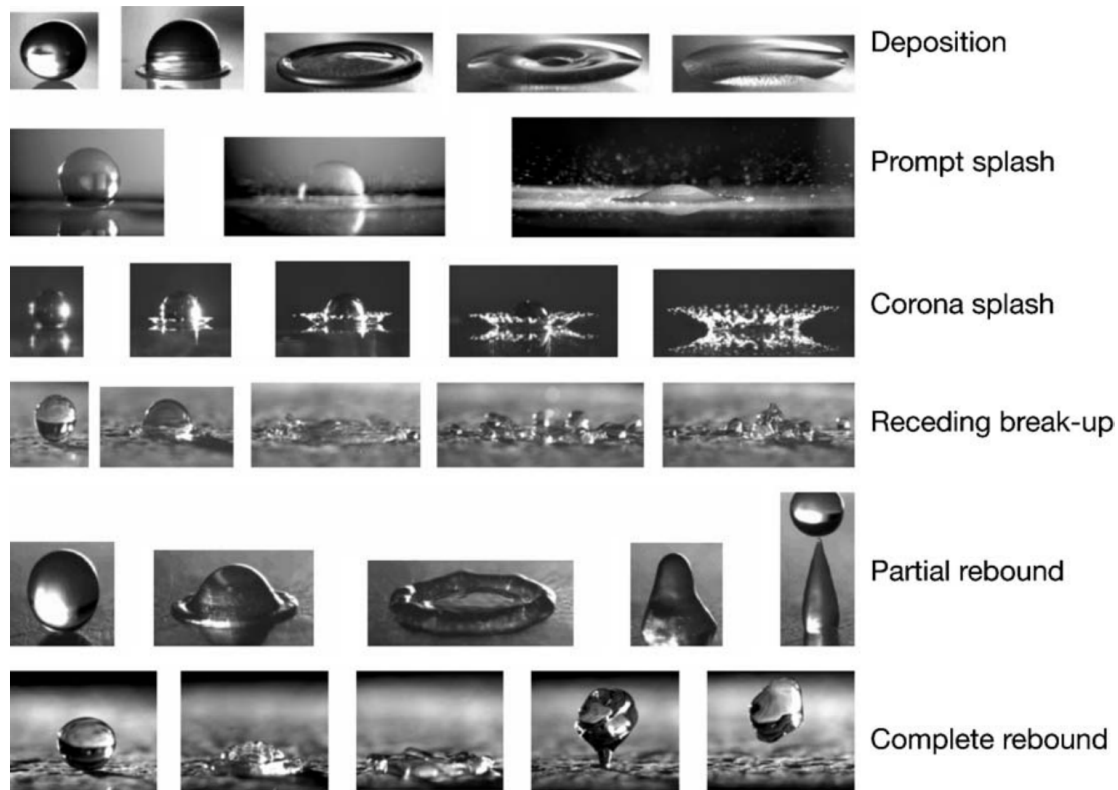


Figure 1.2. Examples of six possible outcomes of drop impact on dry surfaces. The images are taken from Rioboo et al. [15] and adopted by Yarin. [6].

Table 1.1

Summary of various effects on possible drop impact outcomes, adapted from Rioboo et al. [15].

Increase of	Deposition	Splash	Receding break-up	Rebound
Impact velocity ( $U$ )	↓	↑	↑	↑
Droplet diameter ( $D$ )	↓	↑		
Surface tension ( $\sigma$ )		↓	↑	↑
Dynamic viscosity ( $\mu$ )	↑	↓	↓	
Receding contact angle ( $\theta_{\text{rec}}$ )			↑	↑

parameter to describe the spreading dynamics and has applications in ink-jet printing [16] and forensic science [17]. Several recent studies have focused on establishing the relations between maximum spreading radius (or diameter) and the impact parameters, such as inertia, viscous, and capillary forces [18, 19, 20, 21, 22, 23, 24]. A maximum dimensionless

spreading factor is defined as:

$$\beta = \frac{D_{\max}}{D_0}, \quad (1.6)$$

the ratio of maximum spreading diameter ( $D_{\max}$ ) to the initial one ( $D_0$ ).

In the literature, several theoretical models have been developed aiming at accurate modeling of the maximum spreading factor,  $\beta$ , as discussed below. First, when the kinetic energy, ( $E_{kin} \sim \rho D_0^3 U^2$ ) is dissipated by viscosity ( $E_v \sim \phi V t_e$ , where  $\phi \sim \mu (\frac{U}{h})^2$  is dissipation per unit mass,  $V = \frac{\pi}{4} D_{max}^2 h$  is the drop volume,  $h$  is the thickness of maximal spreading drop,  $t_e \sim D/U$  is the characteristic time for deformation). Therefore,  $E_v \sim \mu (U/h) D_{\max}^3$  [25, 26, 27]. Furthermore, based on the volume conservation ( $h D_{\max}^2 \sim D_0^3$ ), the spreading factor can be simplified to [19, 23, 26]

$$\beta \sim Re^{1/5}. \quad (1.7)$$

This is so-called viscous regime, only viscous effect is taken into consideration and applicable for  $Re > 100$  [7, 26, 28, 29]. However, in the forensic domain, people usually use a model with a scaling law of  $Re^{1/4}$  in the viscous regime, rather than the  $Re^{1/5}$  scaling reported by several experimental results [19, 23, 28, 29, 30, 31].

Second, in contrast, in the inertial regime, a model considers a more complex balance including inertia, capillary, and viscous effects [7]. On superhydrophobic surfaces, the viscous dissipation is assumed to be zero, hence the kinetic energy ( $\sim \rho D_0^3 U^2$ ) is totally transferred to surface energy ( $\sim \sigma D_{\max}^2$ ), the energy conservation would yield [32]

$$\beta \sim We^{1/2}. \quad (1.8)$$

However, this is a theoretical model for  $We > 100$  [24, 33], and this scaling relation is hardly observed experimentally [3, 7].

Third, Clanet et al. [23] used a balloon full of water to simulate the interaction between the droplet and surface and found the flow motion inside the balloon as shown in Fig. 1.3. When the drop reaches its maximum spreading diameter, the droplet becomes a pancake shape. The droplet velocity reduces to zero, within the time  $t = D_0/U_0$ , and the acceleration can be represented as  $\gamma \sim U_0^2/D_0$ , where  $D_0$  and  $U_0$  are the drop initial diameter and impact

velocity, respectively. They assumed that the thickness of drop puddle is similar to capillary length,  $h \sim \sqrt{\sigma/(\rho\gamma)}$ , based on the volume conservation that  $\pi D_{max}^2 h/4 = 4\pi(D_0/2)^2/3$ , so the spreading factor can be deduced as [23]:

$$\beta \sim We^{1/4}. \quad (1.9)$$

This scaling law shows good agreement with experimental results on hydrophobic surfaces and, hence, is widely used to fit experimental data (verified for  $3 < We < 3000$ ) [7, 23, 31, 34].

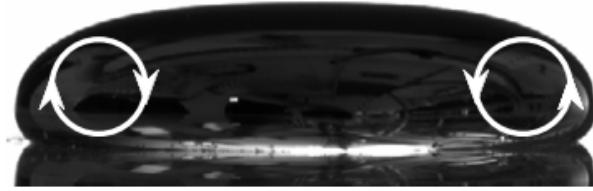


Figure 1.3. Sketch of the vortical motion revealed by the presence of tracers inside the balloon. The image is from Clanet et al. [23].

There are several other models proposed to correlate  $\beta$ , including a consideration of the effect of surface wettability. Pasandideh-Fard et al. [21] derived another energy equation by considering the total energy, i.e., before impact the kinetic energy [ $KE_1 = (\frac{1}{2}\rho U^2)(\frac{\pi}{6}D_0^3)$ ] and surface energy ( $SE_1 = \pi D_0\gamma$ ) are known. After impact, when droplet reach maximal extension, the kinetic energy is zero, and the surface energy can be modeled as  $SE_2 = \frac{\pi}{4}D_{max}^2\gamma(1 - \cos\theta_a)$ , where  $\gamma$  is the surface tension, and  $\theta_a$  is advancing contact angle. The energy lost by viscosity dissipation is calculated as  $W = \frac{\pi}{3}\rho U^2 D_0 D_{max}^2 \frac{1}{\sqrt{Re}}$ . Based on the energy balance between this two moments, i.e.,  $KE_1 + SE_1 = SE_2 + W$ , they obtained an expression of  $\beta$ :

$$\beta = \left( \frac{We + 12}{3(1 - \cos\theta_a) + 4(We/\sqrt{Re})} \right)^{1/2}. \quad (1.10)$$

This model shows a good agreement with their experimental results with an error less than 15%. If  $We \gg \sqrt{Re}$  and  $We \gg 12$ , Eq. (1.10) reduced to  $\beta = \frac{1}{2}Re^{1/4}$ . Ukiwe et al. [22]

modified previous model, introduced dynamic contact angle, and found

$$(We + 12)\beta = 8 + \beta^3(3(1 - \cos\theta_d) + 4We/\sqrt{Re}), \quad (1.11)$$

where  $\theta_d$  is dynamic contact angle. The improved model yields a error of  $5.09 \pm 5.05\%$ . Recently, dynamical models studying the time evolution of a thin liquid film on a solid substrate have provided a general framework on spreading that correctly describing the two regimes (viscous and inertial) and reconciling most of the existing models [7]. Roisman [35] introduced a viscous boundary layer combining with mass conservation, and a semi-empirical relation was obtained:

$$\beta \sim 0.87Re^{1/5} - 0.4Re^{2/5}We^{-1/2}. \quad (1.12)$$

Bartolo et al. [31] introduced an impact number  $P = We \cdot Re^{-4/5}$ . They found when  $P < 1$ , droplet inertia dominants, and Eq. (1.9) fits well with experimental data. When  $P > 1$ , viscous dominants and Eq. (1.7) matched with results. On the basis of this, Eggers et al. [24] introduced the viscous boundary layer in a similar way as Roisman [35] and derived equation relating spreading factor as a function of impact number,  $P$ :

$$\beta = Re^{1/5}f(P). \quad (1.13)$$

Lann et al. [28] further changed the definition of  $P$  to  $P = We \cdot Re^{-2/5}$  considering energy conservation instead of momentum conservation. These different models for the maximum spreading factor  $\beta$  are summerized in Table 1.2.

### 1.2.2 Splashing threshold

Splash, including prompt splash and corona splash (shown in Fig. 1.4) becomes the dominant phenomenon as impact velocity is increased. Prompt splash is observed directly at the contact line, while corona splash happens around the rim of the corona above the surface [7, 15].

Mundo et al. [36] proposed that splash is a combined effect of inertia, viscous force, and surface tension, so it should be characterized by both the dimensionless numbers of  $Re$  and

Table 1.2

Various models of spreading factor,  $\beta$ .

Author	Expression	Note
Scheller et al. (1995) [20]	$\beta \sim 0.61(Re^2 Oh)^{1/6}$	Empirical law based on experiments.
Madejski. (1976) [29]	$\beta \sim Re^{1/5}$	Based on energy conservation and only works in the viscous regime for $Re > 100$ .
Bennett et al. (1993) [33]	$\beta \sim We^{1/2}$	Analytical results in the inertial regime for $We > 100$ , but hardly observed experimentally.
Clanet et al. (2004) [23]	$\beta \sim We^{1/4}$	Based on mass and momentum balance; widely validated to $We = 300$ .
Pasandideh-Fard et al. (1996) [21]	$\beta = \left( \frac{We+12}{3(1-\cos\theta_a)+4(We/\sqrt{Re})} \right)^{1/2}$	Energy balance including contact angle.
Ukiwe et al. (2005) [22]	$(We+12)\beta = 8 + \beta^3(3(1-\cos\theta_a) + 4We/\sqrt{Re})$	Modification of the above model including dynamic contact angle with better accuracy.
Roisman (2009) [35]	$\beta \sim 0.87Re^{1/5} - 0.4Re^{2/5}We^{-1/2}$	Dynamic model of spreading involving viscous boundary layer.
Eggers et al. (2010) [24]	$\beta = Re^{1/5} f(p), p = WeRe^{-4/5}$	Similar method with the above model but including impact number $p$ .
Laan et al. (2014) [28]	$\beta = Re^{1/5} f(P), P = WeRe^{-2/5}$	Similar to the above model with a different impact number $P$ .

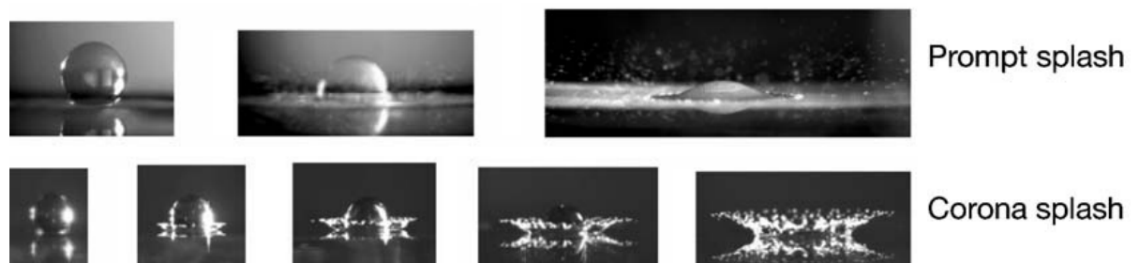


Figure 1.4. Prompt splash and corona splash pictured by Riboo et al. [15].

$We$ . They introduced a splashing parameter, which is defined as:

$$K = We^{1/2} Re^{1/4} = Oh \cdot Re^{5/4} \quad (1.14)$$

They found splash would happen when  $K > 57.7$ , but this threshold was found not so accurate by later experiments and research [25, 37]. In some other papers, the splashing

parameter shows a deviation from Eq. (1.14) [38, 39] as

$$K = We\sqrt{Re}. \quad (1.15)$$

However, both Eq. (1.14) and (1.15) are semi-empirical formulas without a clear expression of the splash mechanism. Therefore, many scholars have devoted themselves to analyze the underlying mechanism of the splash, such as air film perspective and contact angle perspective [40, 41, 42, 43]. In general, the splash phenomenon is one of the most complex phenomena in the process of droplet-wall interaction, and there is no consensus on the threshold and accurate model of the splash phenomenon.

### 1.2.3 Numerical simulations

Drop impact is a complex problem including multiphase flow and several influencing parameters, and hence it is suitable to take advantage of numerical simulations to tackle the problem systematically. The commonly used numerical simulation methods for the problem include Volume of Fluid (VOF) [44], Level Set (LS) [45], Coupled Level Set and Volume of Fluid (CLSVOF) [46], and Lattice Boltzmann (LBM) [47] methods. Recent studies on the numerical simulations of a water droplet impacting solid surfaces are listed in Table. 1.3 with essential parameters.

Table 1.3

Summary of recent numerical simulations of water droplet impact on solid surfaces.

Author	Method	Equilibrium Contact Angle (°)	Weber number( $We$ )
Visser et al. [48]	VOF	25, 90, 135	196, 312
Lee et al. [49]	VOF	61	1.1~289
Gunjal et al. [44]	VOF	40, 110	2.78, 3.08, 34.2
Oukach et al. [50]	LS	120	57
Yokoi et al. [51]	CLSVOF	90	31.7
Sun et al. [52]	CLSVOF	160	27.3
Griebel et al. [53]	CLSVOF	31, 107	12.8, 103
Zhang et al. [54]	LBM	0, 50, 96, 180	128

Like experiments, the droplet size, impact velocity, and surface wettability are usually treated as controlled parameters. Instead of static contact angle (SCA), researchers also

have used different methods to model dynamic contact angle to vary or control surface wettability. Lunkad et al. [55] have found that, for more wettable surfaces ( $SCA < 90^\circ$ ), the dynamic contact angle (DCA) model performed better in terms of predicting rebound regime. Yokoi et al. [51] found that the DCA model can describe the drop impact dynamics more accurately. However, it can only work precisely when using the experimental results of contact angle, implying that a simplified general dynamic contact angle model is not available before all experimental situations.

As for surfaces, the numerical simulation helps researchers to build some complex structures and shapes, which is not easy to achieve in real life. Wang et al. [56] studied a droplet impacting on a mixed-wettability surface composed of a hydrophilic surface and a hydrophobic strip, particularly the spreading and retraction phenomenon and splitting behavior of droplet impacting under different Weber numbers. They found the requirement of surface wettability and strip width to make droplet splitting. Sun [52] built the CLSVOF model to simulate the droplet impact on a superhydrophobic surface, and the droplet's crushing behavior is studied. The results show the relation between rebound coefficient, contact time, and impact velocity. More specifically, as the impact velocity increases, the rebound coefficient gradually decreases, but the contact time increases. In addition, the two stages of droplet crushing behavior have been identified at impact velocity equals 1 m/s, which is not very high. The first stage occurs in the edge area of the droplet, which is mainly caused by surface tension; the second stage occurs in the inner area of the droplet, mainly due to uneven internal forces.

Numerical simulations are instrumental in analyzing problems that are difficult to tackled experimentally, such as high-speed impact. Visser et al. [48] studied the high-speed (17 m/s) micro-drop impact and successfully found the scaling law of boundary layer thickness and rim diameter, which is difficult to realize from experiments. Pan [57] studied a high-speed droplet impact on a solid surface with different roughness experimentally, and he described the relationship between different splashing phenomena. The prompt splash, which is generally thought to only occur on a rough surface, could also be observed on a smooth surface as  $We$

was sufficiently large. Corona splash was observed for heptane and nonane at high  $We$ , but it was not observed for water and water-glycerol solution. Most experiments let the droplet free fall, so the maximum impact speed is about 7 m/s. However, most current numerical simulations focus on the interaction between liquid droplets and solid walls with an impact speed of less than 10 m/s. The main reason might be the lack of experimental data to validate.

Air film/bubble entrapment is another interesting perspective to analyze in drop impact [40, 58, 59, 60]. The pressure difference between liquid and gas leads to the dimple formation and, hence, a trapped air film formed underneath. An air film easily appears at high  $V_I$  due to the significant differences of velocity and intersection angle between liquid and air [61]. Both droplet size and impact velocity influence the size of the bubble entrapped. Bouwhuis et al. have demonstrated an optimum diameter and impact velocity leading to the maximum air bubble entrapment theoretically, experimentally, and numerically [62]. They found that for an ethanol droplet of 1.8 mm radius, the optimal impact velocity of 0.25 m/s achieves the maximal bubble entrapment.

### 1.3 Drop impact on heated surface

When droplet impacts on a heated surface, four distinct evaporation regimes: film evaporation, nucleate boiling, transition boiling and film boiling [63], can be observed from experiments, as shown in Fig. 1.5. Some researchers combine nucleate boiling and transition boiling to bubble boiling regime, in which pagoda-like bubble formation observed [64, 65], as shown in Fig. 1.6.

#### 1.3.1 Experimental phase diagram

For visual and systematical demonstrations of all experimental results, people usually plot a phase diagram to show the outcome of drop impact under various controlled parameters. Tran et al. [66] observed three regimes when surface temperature  $T_s$  higher than saturation temperature  $T_{sat}$  of liquid: contact boiling, gentle film boiling, and spraying film boiling,

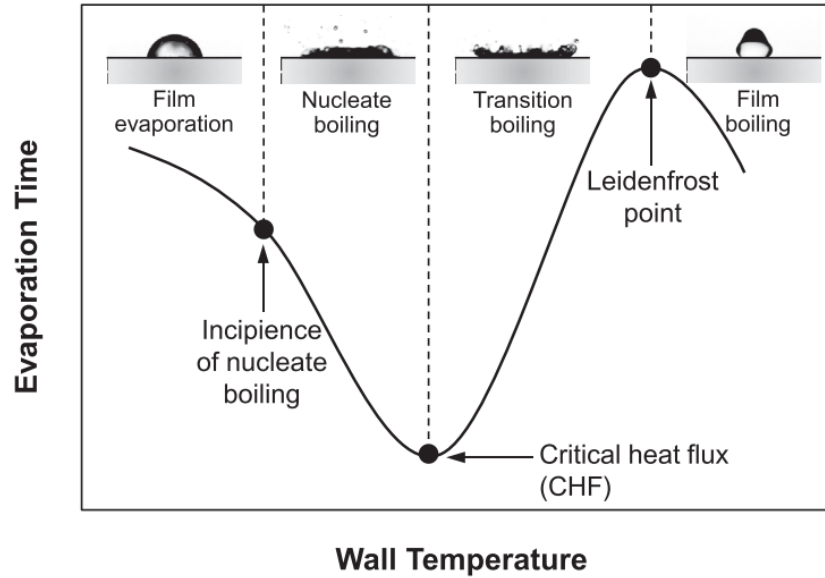


Figure 1.5. Heat transfer regimes associated with a drop impinging a hot surface. The diagram is from Liang et al. [9].

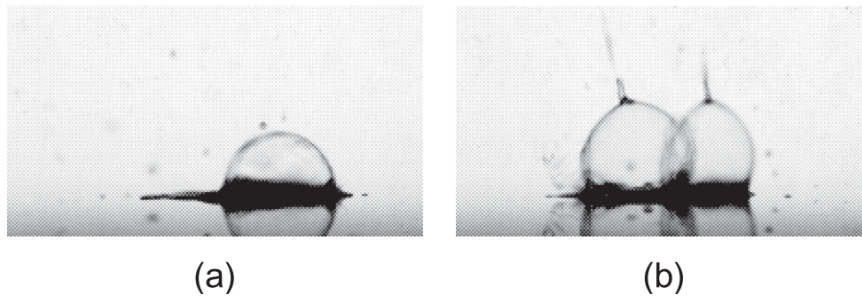


Figure 1.6. (a) Plain bubbles, and (b) pagoda-like bubbles in the bubble boiling regime. Pictures are from Liang et al. [9].

and plotted them based on  $T_s$  and  $We$  as shown in Fig. 1.7. Staat et al. [67] identified four different regimes of an ethanol droplet impact on a sapphire plate, such as deposition, contact-splash, bounce, and film-splash, as shown in Fig. 1.8.

### 1.3.2 Leidenfrost point

Leidenfrost effect, also called film boiling, can be observed when the surface temperature is higher than a critical temperature, so-called Leidenfrost point (temperature), whereby a micron-scale vapor layer is quickly formed between liquid and solid to keep the droplet

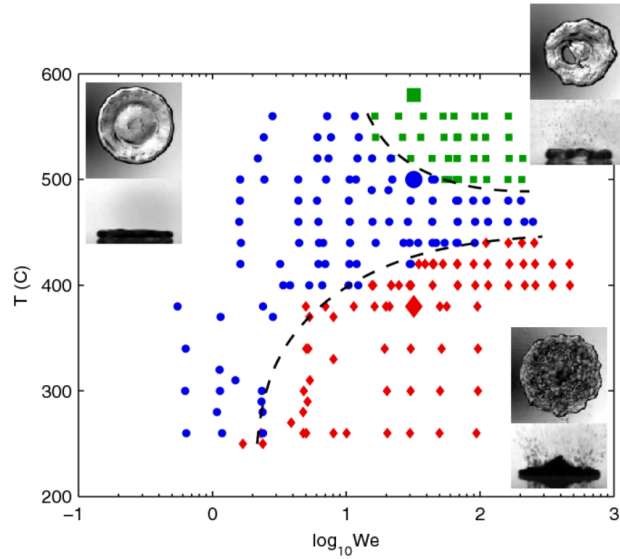


Figure 1.7. Phase diagram for water droplet impact on a heated surface showing three separate regions: contact boiling regime (red solid diamonds), gentle film boiling regime (blue solid circles), and spraying film boiling regime (green solid squares). The diagram is from Tran et al. [66].

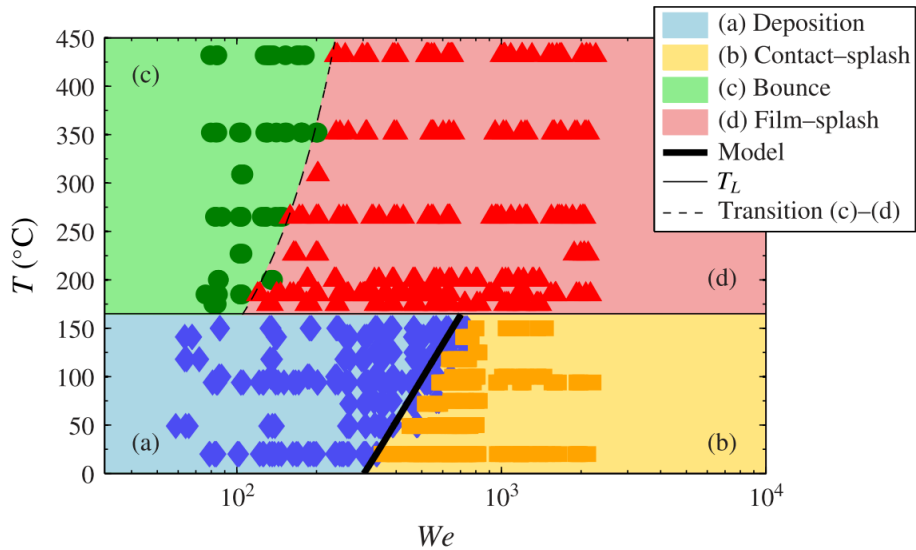


Figure 1.8. Phase diagram of the impact outcomes of an ethanol droplet on a sapphire plate with varying surface temperature and Weber number. Four regimes are identified from the high-speed recordings: deposition (blue diamonds), bounce (green circles), contact-splash (orange squares), and film-splash (red triangles). The diagram is from Staat et al. [67].

from directly contacting with the surface [68]. The insulating vapor film can result in a rebound, break up, and rolling on the surface, depending on different impact momentum [9]. Many studies have shown the difference between static Leidenfrost temperature  $T_L^S$  for a static sessile drop and dynamic Leidenfrost temperature  $T_L^D$  of an impacting drop with speed [66, 69, 70, 71].

Static Leidenfrost temperature,  $T_L^S$ , is found experimentally to depend on droplet and surface characteristics but mainly influenced by surface roughness [72]. Experimental results have shown that irregular nano-scale roughness, such as zirconium nanotubes [73], multiscale micro/nanostructured surface [74] and Si nanowire [75], increases  $T_L^S$ . However, micro-patterned structures may increase [76, 77] or decrease [78, 79]  $T_L^S$ , and the exact mechanism remains to be further investigated.

Concerning dynamic Leidenfrost temperature  $T_L^D$ , some researchers found it is influenced by impact velocity and impact angle experimentally [80, 81]. Yao et al. [80] fit the data and correlated  $T_L^D$  for water as:

$$T_L^D = T_{sat} + 135.6 We^{0.09}, \quad (1.16)$$

where  $T_{sat}$  is saturation temperature of the liquid. Bertola et al. [82] experimentally demonstrated their fitting results as:

$$T_L^D = 164.72 + 29.97 We^{0.38} \quad (1.17)$$

Surface characteristics have been found influencing  $T_L^D$  as well. Irregular nano-scale roughness makes  $T_L^D$  increase [79, 83, 84]. For micro-patterned structures, there is still no consistent conclusion, it may increase [79] or decrease [84, 85]  $T_L^D$ .

### 1.3.3 Temperature change

Monitoring the droplet and surface temperature fields during the interaction is vital for studying liquid-wall heat transfer. Recently, a feasible technology is Infrared (IR) camera, and researchers have used it to record the temperature of the droplet and substrate, as shown in Fig. 1.9 (b), and to validate associated heat transfer models [86, 87, 88]. However,

the currently reported results show that the infrared camera frame rate is relatively low (maximum 1250 fps) [87] compared to a standard high-speed imaging camera, while the accuracy is not adequate.

Recently, Castanet et al. [87] used two-color laser-induced fluorescence (2cLIF) thermometry to measure the droplet temperature change during the impact process, as shown in Fig. 1.9 (a), whose accuracy is better than an IR camera. Adera et al. used micro-electromechanical system (MEMS) technology to integrate heating and temperature measurement by bonding the heating device and thermocouple sensor directly to the back of transparent glass [89]. However, due to the limitation of MEMS technology, the maximum surface temperature could not exceed  $200^{\circ}\text{C}$ . Hence, the research on measuring droplet and surface temperature changes is limited in content and scope.

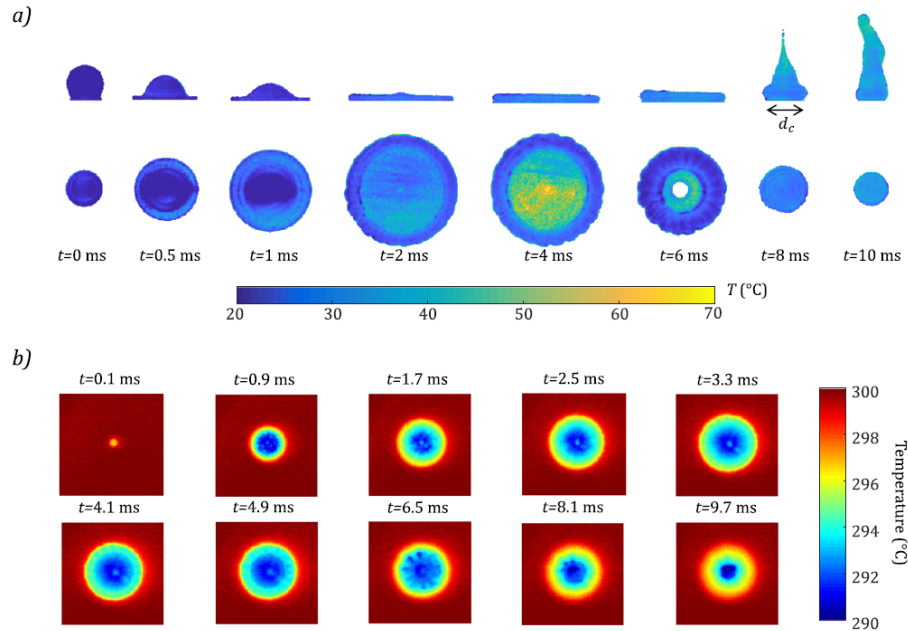


Figure 1.9. (a) Temperature distribution in the liquid drop obtained by 2cLIF imaging. (b) Temperature distribution at the solid surface measured by infrared thermography. Images are from Castanet et al. [87].

## 1.4 Overview of the thesis

The primary objective of this thesis is to study water drop impact dynamics on a solid surface numerically and experimentally, focusing on the influences of impact velocity, surface wettability, and surface temperature.

In Chapter 2, a numerical simulation based on a level-set method is used to simulate a water drop impacting unheated surfaces. The effects of impact velocity and surface wettability on impact outcomes are investigated. By taking advantage of the numerical model, a high-Weber number situation is achieved. The spreading factor has been taken as an essential parameter to validate the numerical codes and further analyze.

We extend the drop impact study to heated surfaces. A high-speed camera and IR (Infrared) camera are set from the side to capture the whole impact process of drop impact on heated surfaces. The sequential images of impact outcomes under various solid temperatures ( $T_s$ ) are demonstrated, and detailed discussions are described in Chapter 3.

Based on the experimental results obtained using high-speed cameras, a phase diagram has been plotted for heated surface situations. Moreover, the droplet and surface temperature changes are analyzed and compared with analytical solutions in Chapter 4.

The conclusions of the thesis work and some suggestions for future work are given in Chapter 5.

## Chapter 2

# Drop Impact Dynamics on Solid Surfaces of Different Wettability<sup>1</sup>

### 2.1 Introduction

Droplet impact on a solid surface is an omnipresent and fascinating multiphase flow problem commonly found in plentiful natural phenomena and industrial processes, e.g., aerospace, automobile, agriculture, metallurgy, combustion engines, as well as chemical and materials engineering. For instance, the drop impact dynamics directly affect the efficiency and outcomes of various applications, such as spraying, printing, painting, crop dusting, and falling raindrops [6, 7, 19]. The complex interplay of several factors, such as droplet speed and size, liquid properties (e.g., density and viscosity), surface parameters (e.g., roughness, wettability, stiffness, and temperature) as well as surrounding air or gas, makes it difficult to predict the drop impact outcomes in advance due to the vast parameter space. Therefore, some dimensionless numbers are commonly used to describe the interaction between surface and droplet, including Reynolds number ( $Re = \rho V_I D_0 / \mu$ ) and Weber number ( $We = \rho V_I^2 D_0 / \sigma$ ), where  $\rho$ ,  $V_I$ ,  $D_0$ ,  $\mu$ , and  $\sigma$  represent liquid density, impact velocity, droplet diameter, dy-

---

<sup>1</sup>The material presented in this chapter is based on Yichi Zhang\*, Yukai Ren\*, Lihui Liu, and Peichun Amy Tsai, “Drop Impact Dynamics on Solid Surfaces of Different Wettability”, submitted (2021). [\* Equally-contributing first authors]

dynamic viscosity, and surface tension, respectively.

Since Worthington’s study of drop impact [14], a broad spectrum of various impact events and dynamics has been discovered experimentally, typically encompassing deposition, spreading, complete rebound, partial rebound, and splashing as the impact velocity is increased [7, 19, 90]. Recently, investigations have demonstrated the significant influence of surface wettability on a variety of flow applications, such as emulsion dynamics [91], a sessile droplet wetting state and evaporation [92, 93], splashing caused by a falling sphere into a deep pool [94], slip flow on solid surfaces [95], fingering patterns during fluid-fluid displacement in microfluidics [96], as well as oil recovery factor during microfluidic EOR (enhanced oil recovery) [97].

Concerning the wettability effect on drop impact dynamics upon a solid surface, several experimental investigations have been carried out with hydrophilic, hydrophobic, and superhydrophobic surfaces [6, 7] (see also the references therein) and shown six primary impact outcomes (e.g., deposition, prompt splash, corona splash, receding break up, partial rebound and complete rebound) on dry surfaces and key influences of droplet diameter/speed, surface tension, and wettability on the six outcomes [15]. Particularly, Antonini et al. [8] have found wettability affects both maximum spreading factor and spreading time for moderate Weber number ( $We < 200$ ). For high-Weber ( $We > 200$ ), in contrast, the wettability effect is negligible during the spreading process. However, the relevant numerical studies are relatively rare because of computational and modeling challenges stem from multiphase flow [98]; it is essential for various applications to elucidate drop impact outcomes comprehensively with local velocity and pressure fields.

Recent insightful numerical simulations reveal that viscous dissipation dominates the energy budget at low impact velocity, but both surface energy and viscous dissipation affect the spreading regime for high-velocity impact [49]. Sun et al. [52] have found the relationship between impact velocity and rebound coefficient as well as with contact time when the droplet impacts on a superhydrophobic surface by using a coupled level-set and volume of fluid (CLSVOF) method. As the impact velocity increases, the contact time between droplet

and surface increases; subsequently, the energy loss increases, air resistance increases, and the rebound coefficient decreases. Researchers also have used different methods to model dynamic contact angle to vary or control surface wettability. Lunkad et al. [55] have found that for more wettable surfaces ( $\text{SCA} < 90^\circ$ ), the dynamic contact angle (DCA) model performed better in terms of predicting partial or complete rebound regime. Yokoi et al. [51] also found that a DCA model can describe the drop impact dynamics more accurately. However, it can only work precisely when using the experimental results of contact angle, implying that a simplified, general dynamic contact angle model is not available for all situations.

Air film/bubble entrapment is another interesting topic in drop impact [40, 58, 59, 60]. The pressure difference between liquid and gas leads to the dimple formation and, hence, a trapped air film formed underneath. An air film easily appears at high  $V_I$  due to the large differences of velocity and intersection angle between the liquid and air [99]. Both droplet size and impact velocity influence the size of the bubble entrapped. Bouwhuis et al. [62] have demonstrated an optimum diameter and impact velocity leading to the maximum air bubble entrapment theoretically, experimentally, and numerically. Numerical simulations are beneficial to analyze problems that are difficult to tackle experimentally, such as high-speed impact and micro- or nano-scale droplets. Visser et al. [48] studied the high-speed micro-drop impact with VOF method and successfully found the scaling laws of dimensionless boundary layer thickness [ $\delta_{\text{BL}} \sim D_0/\sqrt{Re}(t/\tau)^{0.45}$ ] and rim diameter [ $D_{\text{Rim}} \sim D_0/\sqrt{We}(t/\tau)^{0.68}$ ] with drop diameter  $D_0$  and inertial time scale  $\tau = D_0/V_0$ .

In this paper, we focus on comprehensive comparisons between experimental and numerical simulation results, particularly on the surface wettability effect, which has been relatively rarely addressed using numerical simulations. We carry out both experimental and numerical studies to systematically elucidate the drop impact dynamics, the flow and pressure fields simulated, and the influence of impact velocity and surface wettability, which is conveniently parameterized using the static wetting contact angle ( $\theta_w$ ). The numerical results generally show good quantitative agreement with experimental data. The simula-

tion data of pressure and flow fields elucidate intriguing drop impact dynamics observed in the experiments, e.g., complete rebound on SH surface, entrapping air bubble, and jetting. Furthermore, the numerical results suggest a universal scaling law of maximum spreading factor depending on  $We$ .

## 2.2 Numerical Simulation

### 2.2.1 Mathematical Model

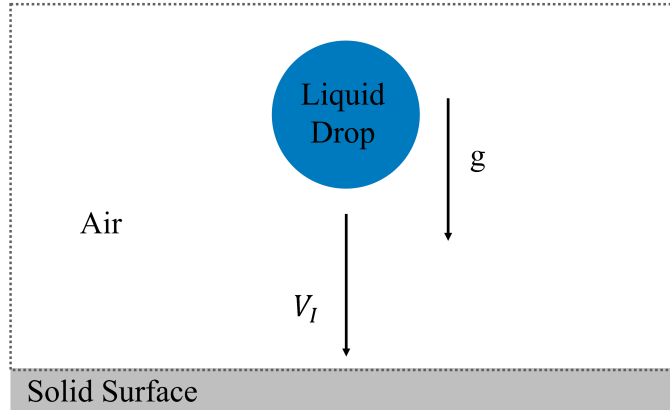


Figure 2.1. Schematic of a droplet impacting at a speed  $V_I$  on a solid surface.

We numerically and experimentally investigate the influence of the surface wettability on the dynamics of a Milli-Q water droplet with an initial diameter,  $D_0$ , impacting a flat surface at a constant speed,  $V_I$ . Fig. 2.1 shows the schematic of our computational domain, composed of both air and liquid regions. We vary the droplet impacting speed,  $V_I$ , and the wetting property regarding contact angle,  $\theta_w$ , of a water droplet on a flat solid surface. In addition to a gravity force downward, surface tension acts on the immiscible gas-liquid interface.

We consider an incompressible flow, and the governing equations of the droplet dynamics are based on the conservation of both mass and momentum. The flow field,  $\mathbf{u}$  can hence be

modeled by solving the Navier-Stokes (N-S) equations [100]:

$$\nabla \cdot \mathbf{u} = 0, \quad (2.1)$$

$$\rho \left( \frac{\partial \mathbf{u}}{\partial t} + (\mathbf{u} \cdot \nabla) \mathbf{u} \right) = -\nabla p + \mu \nabla^2 \mathbf{u} + \rho g \hat{\mathbf{z}} + \mathbf{F}_e, \quad (2.2)$$

where  $\mathbf{u}$  is velocity field,  $\rho$  is fluid density,  $p$  is pressure field,  $\mu$  is the fluid dynamic viscosity, and  $g$  is the gravitational acceleration;  $\mathbf{F}_e$  represents other external force. Since the flow is incompressible, the flow velocity field will be divergence free.

To simulate the two-phase flow problem, we employ a level-set model [101] to track the interface between the air and droplet. The air-liquid interface is modeled using a level set variable,  $\phi$ . The level set function shows the level-set variable related to position and time:  $\phi = \phi(r, t)$ ,  $r \in \Omega$ , where  $\Omega$  represents the domain of interest. The equation for the evolution of  $\phi$ , corresponding to the motion of the interface, is modeled by the convection equation [102]:

$$\frac{\partial \phi}{\partial t} + \nabla \cdot (\mathbf{u}\phi) = 0. \quad (2.3)$$

This level-set function is defined as a signed distance function from the interface. It shows the shortest distance between interface and a given point in the domain.

$$|\phi(r)| = d(r) = \text{Min}_{r_I \in I} (|r - r_I|), \quad (2.4)$$

where  $I$  represents the interface, so the level-set function is positive,  $\phi(r) > 0$ , on one side of the interface and negative on the other,  $\phi(r) < 0$ .

The Heaviside function [102] is usually used to represent the density and the viscosity in the two phases:

$$H(\phi) = \begin{cases} 0, & \phi < 0 \\ 1, & \phi > 0 \end{cases} \quad (2.5)$$

However, the abrupt jump in the fields will cause numerical instabilities in the Finite Element

Method. Therefore, a smeared out Heaviside function ( $H_{sm}$ ) [102] is often used instead:

$$H_{sm}(\phi) = \begin{cases} 0, & \phi < -\varepsilon \\ \frac{1}{2} + \frac{\phi}{2\varepsilon} + \frac{1}{2\pi} \sin \frac{\pi\phi}{\varepsilon}, & -\varepsilon \leq \phi \leq \varepsilon \\ 1, & \phi > \varepsilon \end{cases} \quad (2.6)$$

where  $\varepsilon$  corresponds to half the thickness of the interface. The interface thickness shall depend on the grid size of the mesh, such that simulations are sufficiently resolved. One can then define a new level set function

$$\bar{\phi}(r) = H_{sm}(\phi(r)). \quad (2.7)$$

The density and viscosity can then be calculated for the different phases using one single variable of the modified level-set function,  $\bar{\phi}$ , using:

$$\rho(r) = \rho_1 + (\rho_2 - \rho_1)\bar{\phi}(r), \quad (2.8)$$

$$\mu(r) = \mu_1 + (\mu_2 - \mu_1)\bar{\phi}(r). \quad (2.9)$$

In addition, the interface's normal vector ( $\mathbf{n}$ ) and curvature ( $\kappa$ ) need to be calculated [102], using

$$\mathbf{n} = \frac{\nabla\phi}{|\nabla\phi|}, \quad (2.10)$$

$$\kappa = -\nabla \cdot \mathbf{n} = -\nabla \cdot \frac{\nabla\phi}{|\nabla\phi|}. \quad (2.11)$$

To maintain the thickness of the interface, an intermediate step has to be performed in the numerical simulation [102]. This step adds an artificial compression and is implemented by solving the following conservation law [102]:

$$\frac{\partial\phi}{\partial\tau} + \nabla \cdot \mathbf{f}(\phi) = 0, \quad (2.12)$$

$$\mathbf{f} = \phi(1 - \phi)\mathbf{n} = \phi(1 - \phi) \frac{\nabla\phi}{|\nabla\phi|}, \quad (2.13)$$

where  $\tau$  is the artificial time, and  $\mathbf{f}$  is the artificial flux. The flux works in a region  $\phi$  between 0 and 1, in the normal direction of the interface. To avoid discontinuities at the interface, a

small amount of diffusion is added to Eq. (2.12)

$$\frac{\partial \phi}{\partial \tau} + \nabla \cdot \mathbf{f}(\phi) = \varepsilon \nabla^2 \phi. \quad (2.14)$$

When calculating Eq. (2.3) and (2.14) together, it is possible to combine these equations to one by setting the artificial time equal to the real time. The final  $\phi$ -Eq becomes:

$$\frac{\partial \phi}{\partial t} + \nabla \cdot \left( \mathbf{u}\phi + \phi(1-\phi) \frac{\nabla \phi}{|\nabla \phi|} - \varepsilon \nabla \phi \right) = 0. \quad (2.15)$$

This equation is coupled to the Navier-Stokes equations through the level-set function ( $\phi$ ) and the velocity field ( $\mathbf{u}$ ). Thus, the final governing equations of the multiphase flow problem are Eqs. (2.1), (2.2) and (2.15), solving for  $\mathbf{u}$ ,  $p$ , and  $\phi$ .

### 2.2.2 Numerical Modeling

The simulation model is solved by a finite element method using COMSOL Multiphysics 5.4 [103], employing a level-set model of two-phase flow. We consider symmetrical drop motion without circumferential movement, and hence employ two-dimensional, axis-symmetric numerical domain. The appropriate boundary conditions used include the following two parts. First, open boundary conditions at top and side (air) boundaries, implying that the fluid can enter or leave the domain on the boundaries without restriction by setting  $p$  as hydrostatic pressure at the boundaries. Second, slip and wetted wall conditions at bottom (solid) surface are implemented, modeled as:

$$\mathbf{u} \cdot \mathbf{n}_{\text{wall}} = 0, \quad (2.16)$$

$$\mathbf{F}_{\text{wall}} = \mathbf{F}_{\theta} + \mathbf{F}_{\text{fr}}, \quad (2.17)$$

$$\mathbf{F}_{\theta} = \sigma \delta(\mathbf{n}_{\text{wall}} \cdot \mathbf{n}_{\text{int}} - \cos(\theta_w)) \mathbf{n}_{\text{int}}, \quad (2.18)$$

$$\mathbf{F}_{\text{fr}} = -\frac{\mu}{b} [\mathbf{u} - (\mathbf{u} \cdot \mathbf{n}_{\text{wall}}) \mathbf{n}_{\text{wall}}], \quad (2.19)$$

where  $\sigma$  and  $\delta$  are the surface tension coefficient and Dirac delta function, respectively.  $\mathbf{n}_{\text{wall}}$  and  $\mathbf{n}_{\text{int}}$  are the normal directions of the wall and two-phase interface. The force acting on the fluid by the surface,  $\mathbf{F}_{\text{wall}}$ , consists of the surface frictional force  $\mathbf{F}_{\text{fr}}$  and the

boundary force  $\mathbf{F}_\theta$  that enforces a particular wetting contact angle  $\theta_w$  specified. The wetting condition of the wall is parameterized by contact angle,  $\theta_w$ , and the slip length,  $b$ . As the initial condition, the air is specified as  $\phi = 0$ , and water is  $\phi = 1$  to distinguish the two phases. An initial velocity is provided on the droplet to easily change impact velocity later. The problem is solved with a time-step size of  $4 \times 10^{-5}$  s.

### 2.2.3 Mesh-independence Examination

We carried out mesh-independence examination to verify sufficient numbers of meshes used and to ensure both accuracy and convergence of numerical results. In our model, the physics-controlled mesh type is used, which is automatically created by COMSOL to adapt current physical models and settings [103]. Four mesh schemes are used with their maximum and minimum mesh sizes are shown in Table 2.1.

Table 2.1

Summary of parameters for different mesh schemes.

Mesh Type	Mesh Size ( $\mu\text{m}$ )	Element #
Normal	(102, 219)	4,353
Fine	(80.7, 178)	6,790
Finer	(37.4, 79)	30,678
Extra Fine	(16.8, 42)	114,990

Droplet spreading diameter varying in time,  $D_t$ , is one of the important parameters for analyzing droplet impacting dynamics. The non-dimensional spreading factor,  $\beta$ , can be expressed as:

$$\beta = D_t/D_0, \tag{2.20}$$

where  $D_t$  is spreading diameter after droplet impacts on solid surface, and  $D_0$  is initial droplet diameter. When a water droplet ( $D_0 = 2.35$  mm) impacts on a hydrophillic surface ( $\theta_w = 56^\circ$ ) at a speed of 0.35 m/s, the spreading factor changing under different mesh schemes is shown in Fig. 2.2. For this hydrophillic surface case, the optimal slip length value was found to be  $b = 500$  nm, discussed in detailed in Section 2.3.1. After the calculations of

mean squared error,  $MSE = \frac{1}{n} \sum_{i=1}^n (Y_{\text{observed}} - Y_{\text{predicted}})^2$  [104], "Extra fine mesh" gives the minimum value of MSE of 0.0599, which is close to the value (of  $MSE = 0.0606$ ) for the "Finer mesh". Considering the computational time, the 'Finer mesh' scheme is the optimal choice to save computational time (since the "extra fine mesh" would take 10 times longer time than that for the "finer mesh").

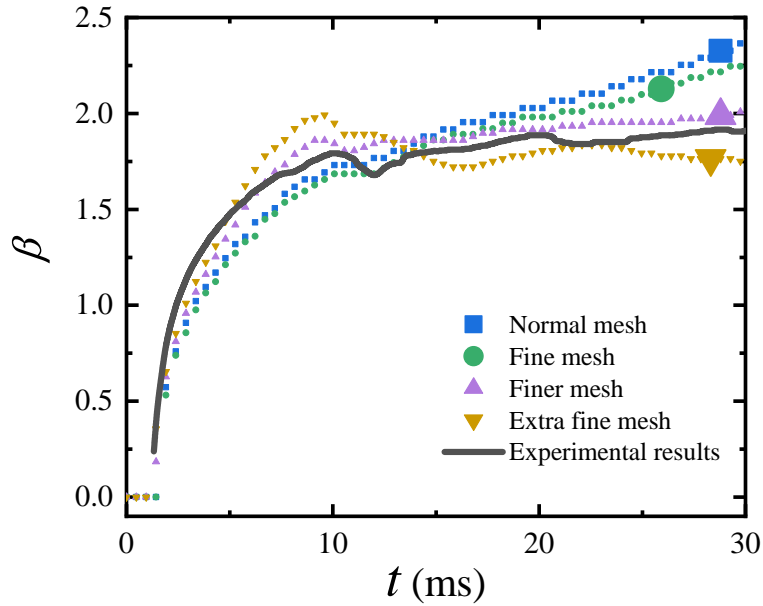


Figure 2.2. Simulation results of dimensionless spreading factor,  $\beta$ , changing with time for different mesh sizes, including normal, fine, finer, and extra fine mesh schemes examined. The mesh-independence check is done by comparing simulation results with experimental one (solid line) of a water droplet impacting on the hydrophilic surface of  $\theta_w = 56^\circ$ , at  $V_I = 0.35$  m/s.

#### 2.2.4 Validation

To validate the simulation results, we have performed a series of experiments of a droplet falling from different heights and hitting on solid surfaces. Experimentally, a Milli-Q droplet (of  $D_0 = 2.35$  mm) impacts a sapphire surface, whose static contact angle was experimentally measured to be  $56^\circ$  with a standard tangent estimation. Fig. 2.3 shows a good agreement between our numerical and experimental results of the drop shape varying in time after impacting on the surface. Here, the impact velocity is  $V_I = 0.35$  m/s, and the droplet

showed a deposition on the wetting surface.

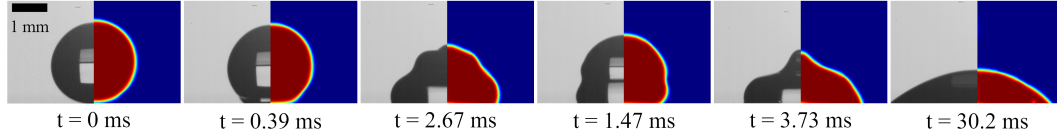


Figure 2.3. Sequential images of experimental (left) and numerical (right) results of water drop impact at  $V_I = 0.35$  m/s on a hydrophilic surface of  $\theta_w = 56^\circ$ . Good agreement of drop shape varying in time is found.

## 2.3 Results and Discussion

### 2.3.1 Slip Length Analysis

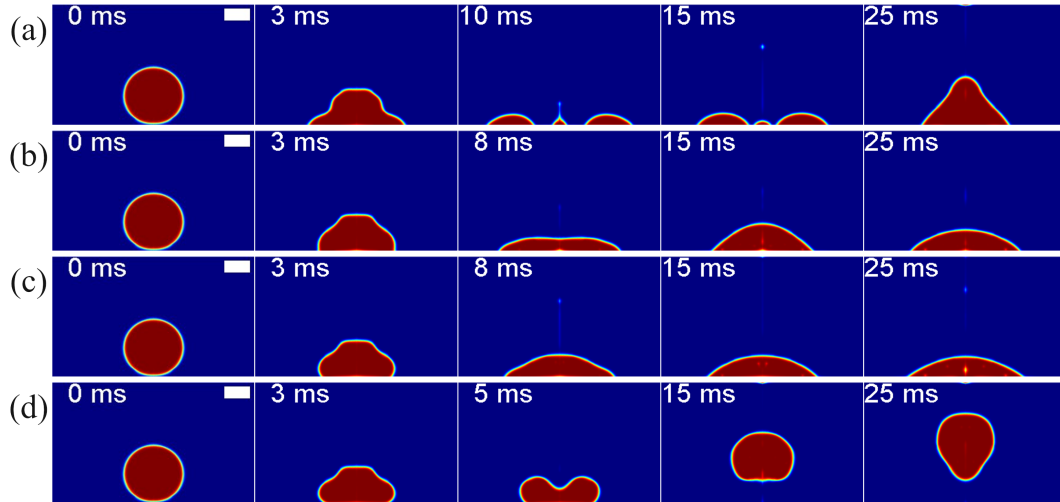


Figure 2.4. Sequential simulation snapshots of water droplet impacting at  $V_I = 0.35$  m/s on a wetting surface of  $\theta_w = 56^\circ$ . Here, the slip-length values used are (a)  $b = 5 \mu\text{m}$ , (b)  $b = 1 \mu\text{m}$  (c)  $b = 500 \text{ nm}$ , and (d)  $b = 10 \text{ nm}$ , from top to bottom, respectively. Different  $b$  values lead to distinct drop shapes and dynamics, transiting from a spreading (b-c) to a complete rebound (d) with decreasing  $b$ . The length bars represent 1 mm.

The slip length  $b$ , parameterized by the flow velocity boundary conditions and related to the friction force  $\mathbf{F}_{\text{wall}}$  [in Eq. (2.17)] at the bottom surface, turns out to be an important parameter to control the motion of droplets on the surface. We systematically investigated the influence of this numerical parameter,  $b$ , on the drop impact dynamics simulated. Shown

in Fig. 2.4 are time-varying drop shapes and motions when a water droplet ( $D_0 = 2.35$  mm) impacting on a hydrophilic surface of  $\theta_w = 56^\circ$  at  $V_I = 0.35$  m/s, using different slip length values. As decreasing  $b$  from  $5 \mu\text{m}$  to  $10$  nm, the droplet motions reveal three distinct impacting events, changing from a central separation of the drop (in Fig. 2.4a), spreading (in Fig. 2.4b-c), and totally rebound (in Fig. 2.4d).

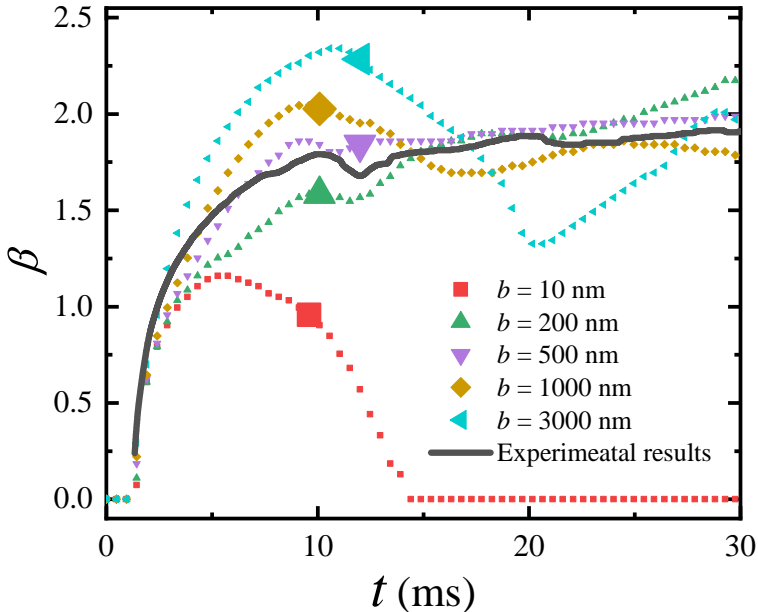


Figure 2.5. The simulation results of spreading factor,  $\beta$ , changing with time for different slip-length values ( $b$ ), compared with experimental results of a water droplet impacting on the hydrophilic surface of  $\theta_w = 56^\circ$  at  $V_I = 0.35$  m/s.

Experimentally, for these parameters ( $V_I = 0.35$  m/s,  $\text{CA} = 56^\circ$ ), the droplet showed a spreading as illustrated in Fig. 2.5. Therefore, the optimal value of  $b$  lies within  $b = 10$  nm –  $5 \mu\text{m}$  to reproduce the experimental results. To find out the best  $b$ -value, a systematical analysis of the spreading dynamics has been done.

Using the spreading factor,  $\beta$ , as the vital outcome to compare, Fig. 2.5 shows the variations with different slip length values,  $b$ , varying between  $10$  and  $3000$  nm. By calculating and comparing mean squared error (MSE), slip length  $b = 500$  nm is the optimal one with the lowest MSE value for this low-Weber number impact on a hydrophilic surface. By the same token with the same systematic analyses, the optimal slip length values are  $b = 100$  nm

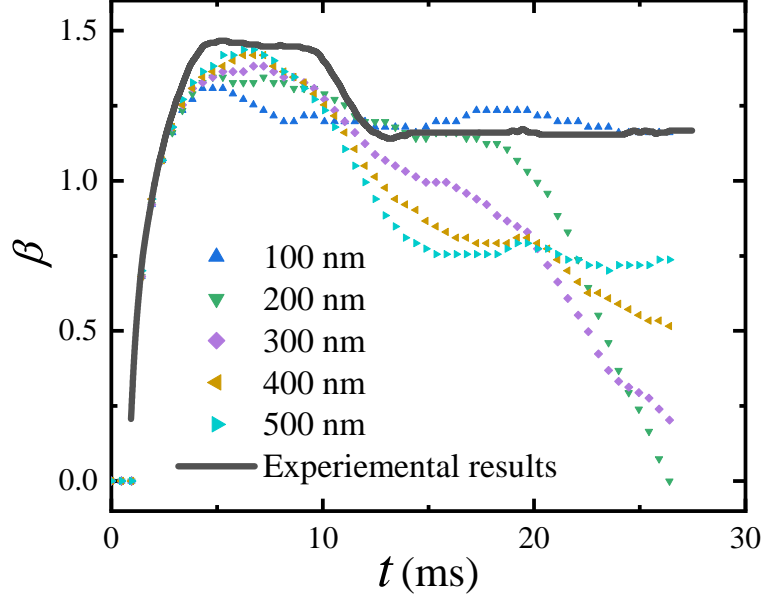


Figure 2.6. The simulation results of spreading factor,  $\beta$ , changing in time with different slip-length values ( $b$ ), comparing with experimental results of a water droplet impacting on the wetted surface of  $\theta_w = 110^\circ$  at  $V_I = 0.5$  m/s.

and  $b = 10$  nm for a hydrophobic ( $\theta_w = 110^\circ$ ) and an ultrahydrophobic surface ( $\theta_w = 158^\circ$ ), respectively. These corresponding simulation results are presented in Fig. 2.6 and 2.7.

### 2.3.2 Effect of Impact Velocity

After the proper slip length values have been chosen, a series of systematical simulations varying impact velocity and wettability were carried out. Shown in Fig. 2.8 is a summary of the phase diagram of various impact dynamics, including both the experimental (open symbols) and simulation (filled symbols) results, under different  $We$  and three different  $\theta_w$ . Overall, the simulation results show consistent impact dynamics with experimental observations (see Fig. 2.8 insets for the characteristic snapshots), especially for low- $We$  ( $\lesssim 100$ ) regime. Generally, we observe mostly spreading for  $\theta_w = 56^\circ$  at  $2 < We < 400$  experimentally, whereas spreading at low- $We$  and a complete rebound, partial rebound, jetting, or splashing at high- $We$  and greater  $\theta_w$  (of  $110^\circ$  and  $156^\circ$ ). Some discrepancies are observed, especially at a high- $We$  ( $\gtrsim 100$ ) where shifted regime boundaries are noticed.

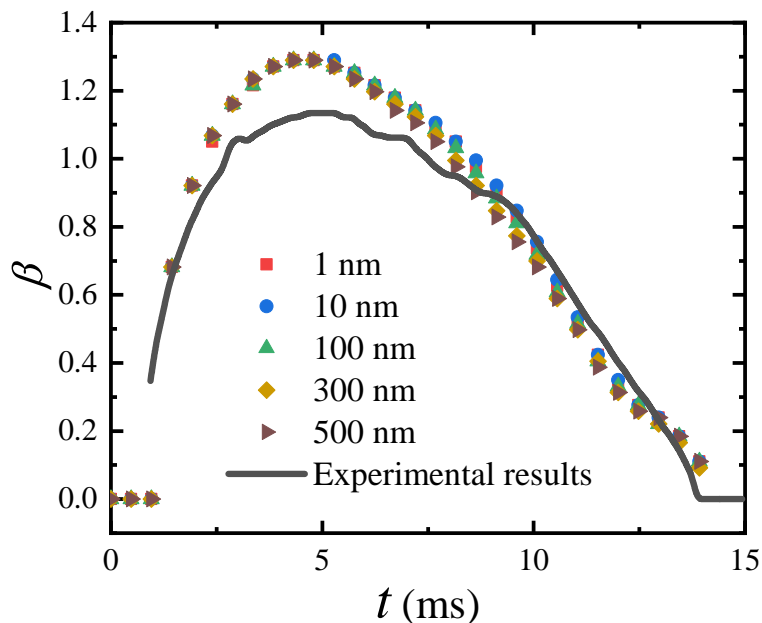


Figure 2.7. The simulation results of spreading factor,  $\beta$ , changing in time with different slip-length values ( $b$ ), comparing with experimental results of a water droplet impacting on the wetted surface of  $\theta_w = 158^\circ$  at  $V_I = 0.5$  m/s.

For a Milli-Q water drop impacting on a hydrophilic surface with  $\theta_w = 56^\circ$ , the typical droplet motions found by our simulations are spreading at  $V_I = 0.35$  m/s and  $V_I = 1.0$  m/s (see Fig. 2.9 a and b), jetting at  $V_I = 2.0$  m/s (see Fig. 2.9 c), and splashing at  $V_I = 3.0$  m/s (see Fig. 2.9 d) as  $V_I$  is increased. The spreading event agrees well with experimental observation at low- $We$ . However, the simulation results of jetting and splashing at high  $We$  are not consistent with our experimental data (see the phase diagram comparison in Fig. 2.8). Guo et al.[105] have numerically found the splashing dynamics on a hydrophilic surface when  $We = 695$ , in line with our simulation results. Thus, the trend from spreading to splashing when increasing  $V_I$  is consistent, but the splashing threshold may differ between the experimental and simulation data.

For impacting on a hydrophobic surface with  $\theta_w = 110^\circ$ , the droplet spreads and deposits on the surface at small  $V_I = 0.5$  m/s (see Fig. 2.10 a). In contrast, when  $V_I = 1$  m/s the drop kinetic energy increases and sufficiently overcomes the gravity, and the droplet rebound

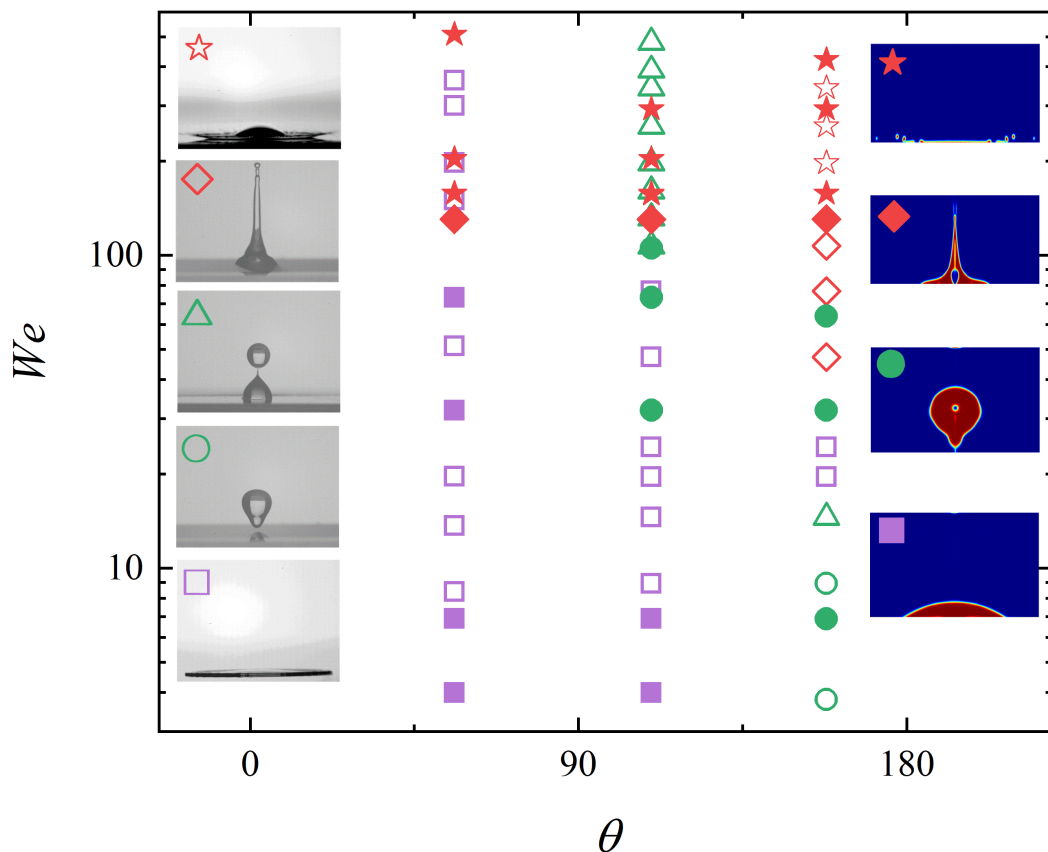


Figure 2.8. Phase diagram summarizing both experimental (open symbols) and simulation (filled symbols) results. The observed impact outcomes include spreading ( $\square$ ,  $\blacksquare$ ), complete rebound ( $\circ$ ,  $\bullet$ ), partial rebound ( $\triangle$ ), jetting ( $\diamond$ ,  $\blacklozenge$ ), and splashing ( $\star$ ,  $\blackstar$ ).

after the collision (see Fig. 2.10 b). As the impact velocity continues increasing to  $V_I = 2.0$  m/s, there is a trend to prompt droplet break up and splash, but under surface tension it still shows recoiling after reaching the maximum spreading diameter and then jetting (e.g. Fig. 2.10 c). Finally, above  $V_I = 2.5$  m/s, water droplet breaks up into small pieces and splashes after the impact (e.g. Fig. 2.10 d-e). Similar to  $\theta_w = 56^\circ$  cases, the simulation results for  $\theta_w = 110^\circ$  agree well with the experimental at low  $V_I$ , but some inconsistent at high  $V_I$ . These discrepancy suggests a different slip length value used for high- $We$  regime.

When impacting on a flat but ultra-hydrophobic surface with  $\theta_w = 158^\circ$ , the droplet starts to fully rebounds at small  $V_I = 0.5$  m/s (see Fig. 2.11 a). Continue increasing the velocity to  $V_I = 1.5$  m/s, despite being more elongated, the whole droplet still fully rebound

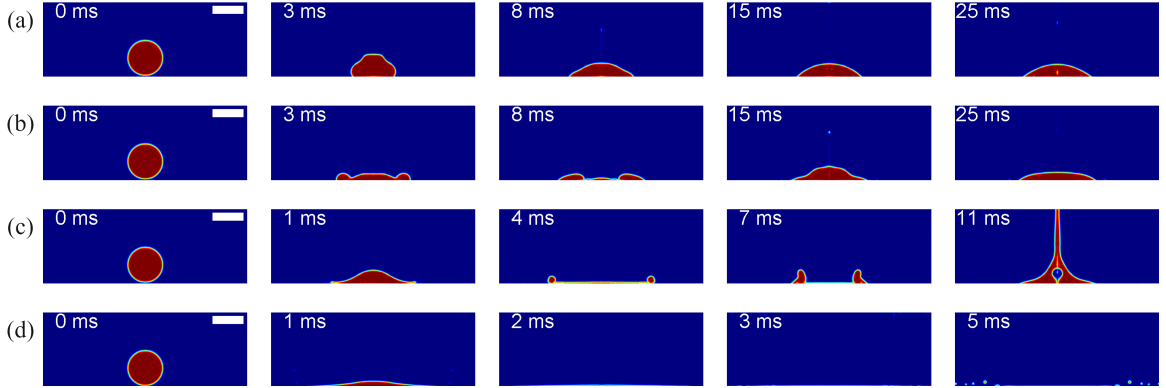


Figure 2.9. Sequential simulation snapshots of water droplet impacting on a hydrophilic flat surface (of  $\theta_w = 56^\circ$ ) reveal different impact events: spreading in (a) and (b), jetting in (c), and splashing in (d), with increasing impact velocity  $V_I$ , at (a) 0.35 m/s, (b) 1.0 m/s, (c) 2.0 m/s, and (d) 3.0 m/s, respectively. The length bars represent 2 mm.

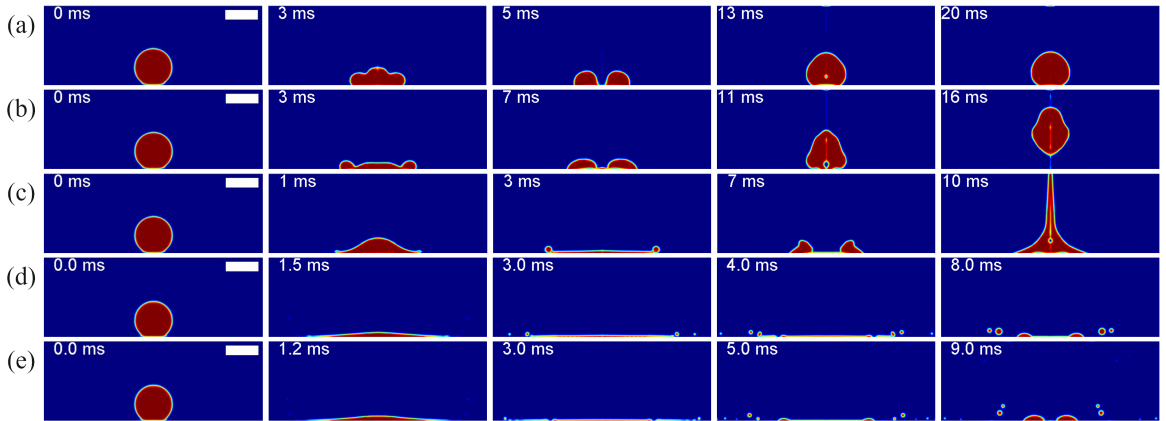


Figure 2.10. Sequential simulation snapshots of water droplet impacting on a hydrophobic surface ( $\theta_w = 110^\circ$ ) reveal different impact events: spreading in (a), rebound in (b), jetting in (c) and splashing in (d)-(e), with increasing impact velocity  $V_I$ , at (a) 0.5 m/s, (b) 1.0 m/s, (c) 2.0 m/s, (d) 2.5 m/s, and (e) 3.0 m/s. The length bars represent 2 mm.

from the surface (see Fig. 2.11 b). When  $V_I = 2.0$  m/s, the droplet shows jetting after spreading and recoiling (see Fig. 2.11 c). Until  $V_I = 2.5$  m/s the droplet starts to splash outward (see Fig. 2.11 d). These simulation results are consistent with experimental as shown in Fig. 2.8.

We further analyze pressure and velocity fields to elucidate the underlying mechanisms of intriguing impact outcomes observed. Taking the ultra-hydrophobic cases, Fig. 2.12–

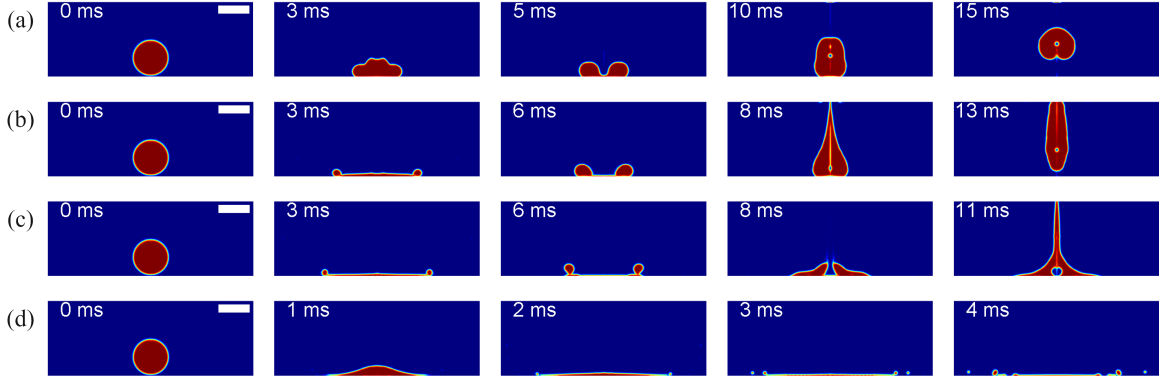


Figure 2.11. Sequential simulation snapshots of water impacting on an ultrahydrophobic surface ( $\theta_w = 158^\circ$ ) reveal different impact events: rebound in (a) and (b), jetting in (c) and splashing in (d), with increasing impact velocity  $V_I$ , at (a) 0.5 m/s, (b) 1.5 m/s, (c) 2.0 m/s, and (d) 2.5 m/s. The length bars represent 2 mm.

2.14 reveal the perspective pressure and velocity fields when  $V_I$  is increased from 0.5 m/s to 2.5 m/s. The pressure field shown is gauge pressure, and the surrounding air pressure is zero at the initial time. The color bars' ranges are adjusted appropriately to demonstrate the details better. Thus, the values shown do not represent the minimum and maximum pressure values. Some regions may be over-saturated; for example, Fig. 2.12c the pressure in the small red circle is about 1300 Pa. All the velocity vectors are normalized, so they have the same length and only describe flow direction.

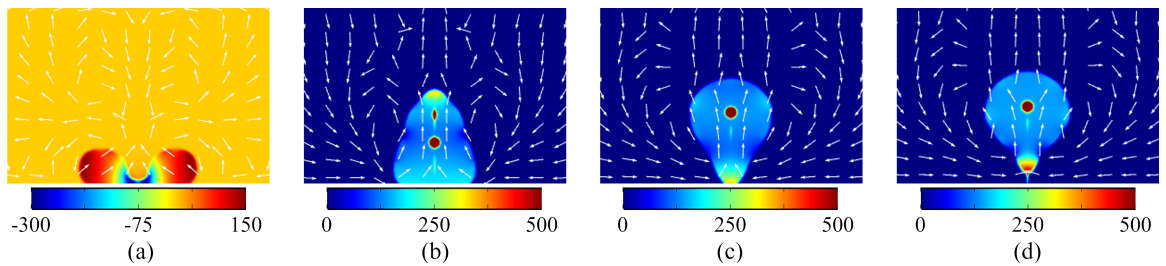


Figure 2.12. The pressure field (rainbow color) and normalized velocity vectors (white arrow) simulated for drop impact on ultrahydrophobic surface ( $\theta_w = 158^\circ$ ) with  $V_I = 0.5$  m/s at different time (a) 5 ms, (b) 9 ms, (c) 13 ms, and (d) 14 ms. The unit of pressure is Pascal (Pa).

How and why does a complete rebound occur at a low  $V_I$  for  $\theta_w = 158^\circ$ ? According to

simulation snapshots for  $V_I = 0.5$  m/s (see Fig. 2.11 a), we find the impact dynamics at 5 ms plays a role in generating the subsequent, complete rebound. As shown in Fig. 2.12a, the drop edge reaches the maximum pressure, with negative pressure and a concave drop shape at the center. The arrows (in Fig. 2.12a) show the flow vectors and indicate that the droplet would recoil towards the center at this time (at  $t \approx 5$  ms), with an average speed about 0.5 m/s. The central air escaped quickly with a maximum speed about 6 m/s, but some central air is entrapped due to the central concave drop deformation. Subsequently, when the lamella recoils due to the surface tension, the droplet entraps an air bubble (shown by the red central bubble in Fig. 2.12 b-d), moving towards the upper droplet surface. During bubbles moving towards the surface, the initial air bubble is also stripped to form secondary bubbles. When bubbles reach the surface of the droplet, they release pressure and then disappear. Thus, the relatively high pressure at the tip at  $t = 9$  ms is caused by the secondary bubble release and high curvature (see Fig. 2.12 b). High curvature also causes high pressure at the drop bottom at  $t = 14$  ms; see Fig. 2.12 d. During the rebounding process, the surrounding air on the two sides falls from the upper to lower position and merges underneath the droplet. The central fluid moves upward mainly, and the early-time flow field causes and explains the subsequent droplet shape. For example, in Fig. 2.12 b, the droplet shows wider at the bottom and thinner at the tip, while the flow field arrows at the center indicate continued recoil to the center and expansion of the upper drop towards the sides. Subsequently, in Fig. 2.12 c, the droplet shape changes and becomes a more inverted triangle. Due to the surface tension, the bottom tip moves toward center fast to make droplets spherical with an average speed around 1 m/s. The surrounding air flows with average speed less than 0.05 m/s, while the liquid flow in central droplet shows an average speed about 0.5 m/s moving upward. Hence, the droplet rebound is mainly related to droplet flow motion since the remaining kinetic energy of the droplet is sufficient to overcome the gravity.

As for a jetting event (e.g. Fig. 2.11 c), the detailed  $P$  and  $\vec{u}$  analysis is shown in Fig. 2.13. As the droplet reaches the maximum spreading diameter, it starts to recoil and forms a crown shape around 6 ms. The surrounding flow direction indicates that the droplet

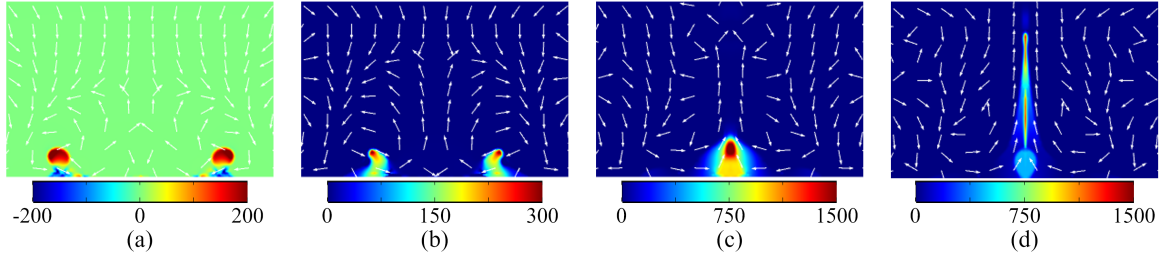


Figure 2.13. The pressure field (rainbow color) and normalized velocity vectors (white arrow) simulated of drop impact on ultrahydrophobic surface ( $\theta_w = 158^\circ$ ) with  $V_I = 2.0$  m/s at different time (a) 6 ms, (b) 7 ms, (c) 8 ms, and (d) 9 ms. The unit of pressure is Pascal (Pa).

would start to recoil instead of continuous spreading. Due to the fast recoiling back, the area under the crown tips shows negative pressure (in Fig. 2.13 a). Airflow hence moves from the zero (gauge pressure) region to the negative pressure region. When the two crown tips recoil, they subsequently merge at the center (Fig. 2.13 c), with a high-pressure (around 1700 Pa) tip producing a jet upward. Due to the fast speed of jetting, the droplet carries surrounding air ejects straightly towards the top boundary as arrows shown in Fig. 2.13 d.

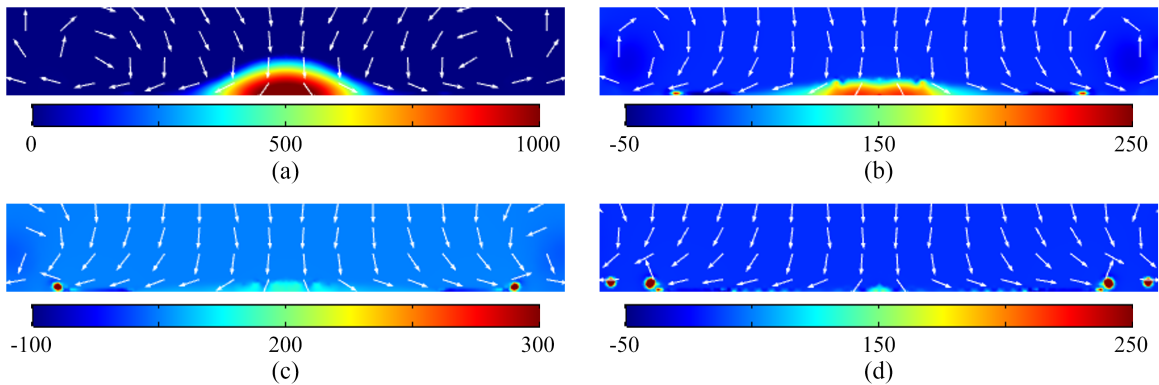


Figure 2.14. The pressure field (rainbow color) and normalized velocity vectors (white arrow) simulated of drop impact on ultrahydrophobic surface ( $\theta_w = 158^\circ$ ) with  $V_I = 2.5$  m/s at different time (a) 1 ms, (b) 1.5 ms, (c) 2 ms, and (d) 3 ms. The unit of pressure is Pascal (Pa).

For a splashing event (e.g., Fig. 2.11 d), the droplet impacts the surface with a considerable speed, so the drop center shows high pressure at 1 ms (see Fig. 2.14 a). During the subsequent drop spreading, the pressure inside gradually decreases as shown in Fig. 2.14 b.

As the local pressure reaches around 800 Pa at the rim (see Fig. 2.14 c), the surface tension is not strong enough to maintain the drop shape, so tiny droplets start to emit, forming splashing. The upper surrounding airflow presses the droplet onto the surface during the spreading phase, as revealed by the flow field arrows. Furthermore, once the tiny droplets at the edge are formed and broke up from the main droplet, the flow field indicates satellite droplets moving outward.

### 2.3.3 Effect of wettability

The dynamic behavior of a droplet impinging on a solid hydrophilic ( $\theta_w = 56^\circ$ ), hydrophobic ( $\theta_w = 110^\circ$ ), and ultra-hydrophobic surface ( $\theta_w = 158^\circ$ ) is numerically investigated. The surface is assumed to be smooth and flat in the simulation, while the only parameter to control the wettability is through the wetting contact angle,  $\theta_w$ . The wettability effect on the drop impact dynamics at  $V_I = 0.5$  m/s is demonstrated through the different events, such as spreading and rebound, observed in Fig. 2.15. At low  $V_I$ , the water droplet spreads, recoils, and finally deposits on the hydrophilic surface with a flattened shape (see Fig. 2.15 a). On the flat, hydrophobic surface, the droplet avoids spreading extensively while keeping its shape more spherical (see Fig. 2.15 b). Finally, on the flat surface of  $\theta_w = 158^\circ$ , the contact line seems not to spread further (between 3 ms to 5 ms), and eventually, the droplet rebounds to minimize surface energy (see Fig. 2.15 c).

Different surface wettability leads to different spreading dynamics and further affects the impact dynamics. As  $\theta_w$  increases, the droplet demonstrates less spreading as to minimize the surface energy, as shown in Fig. 2.16 (a) where three distinct trends of spreading factor ( $\beta$ ) are found for the three surfaces. Theoretically, the initial kinetic energy of the droplet is constant for the same impact velocity, and the kinetic energy is dissipated by the viscosity effect and the friction force exerted on the surface during the spreading process. The droplets spread further until an equilibrium state is reached between surface tension and inertia at the maximum spreading [49]. So less spreading makes more kinetic energy remain. Once the remaining kinetic energy is enough to overcome the gravity of the droplet, it shows a

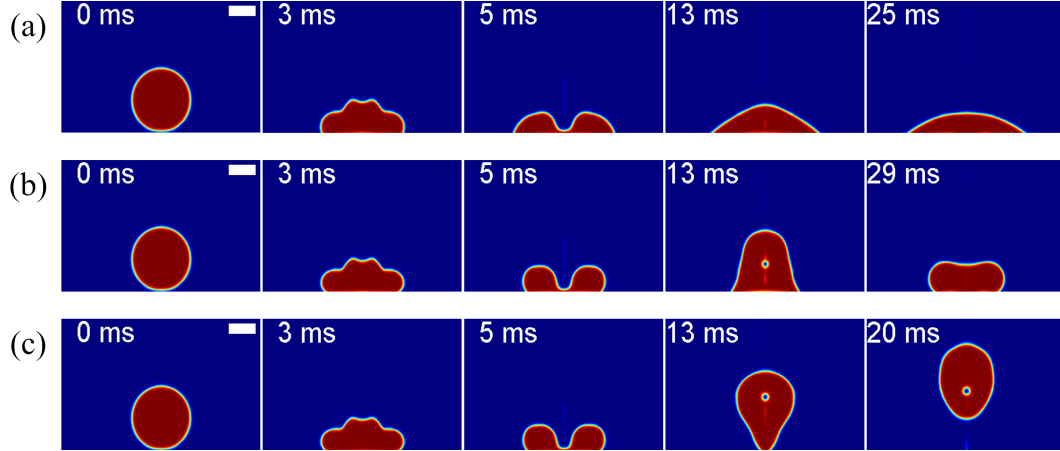


Figure 2.15. Sequential numerical snapshots of a falling droplet evolution at  $V_I = 0.5$  m/s on surfaces with different wetting contact angles: (a)  $\theta_w = 56^\circ$ , (b)  $\theta_w = 110^\circ$ , (c)  $\theta_w = 158^\circ$ . For different  $\theta_w$ , their corresponding optimal slip length values have been investigated and subsequently used, with (a)  $b = 500$  nm, (b)  $b = 100$  nm, (c)  $b = 10$  nm for  $\theta_w = 56^\circ, 110^\circ$ , and  $158^\circ$ , respectively. The length bars represent 1 mm.

total rebound.

At high- $We$  condition ( $We = 398$ ), larger impact velocity leads to the droplet maximum spreading diameter earlier and more extensively on all the surfaces. In Fig. 2.16, for both low and high  $We$ , we can observe a region that the wettability is not influential. The droplet is inertial dominant in this early moment, within the inertial timescale  $\tau \sim D_0/V_I$  [48, 106, 107]. The inertial timescale for our case is estimated to be  $\tau = 5$  ms for low  $We$  and  $\tau = 0.6$  ms for high  $We$ .

Additionally, we have analyzed the relation between the maximum spreading factor and the Weber number, as shown in Fig. 2.17. In the literature, motivated by practical applications various models have been developed to study the maximum  $\beta$  depending on various parameters, e.g.,  $We$ ,  $Re$ , CA, and rheological parameters [3, 19, 20, 21, 22, 23, 24, 26, 28, 29, 33, 35]. For instance, based on energy conservation, when all the kinetic energy is dissipated by viscosity (so-called viscous regime),  $\beta \sim Re^{1/5}$  is derived for  $Re > 100$  [7, 26, 28, 29]. In contrast, when viscous dissipation is negligible, the kinetic energy is transferred to surface energy, yielding  $\beta \sim We^{1/2}$  but found to be inconsistent with some experimental re-

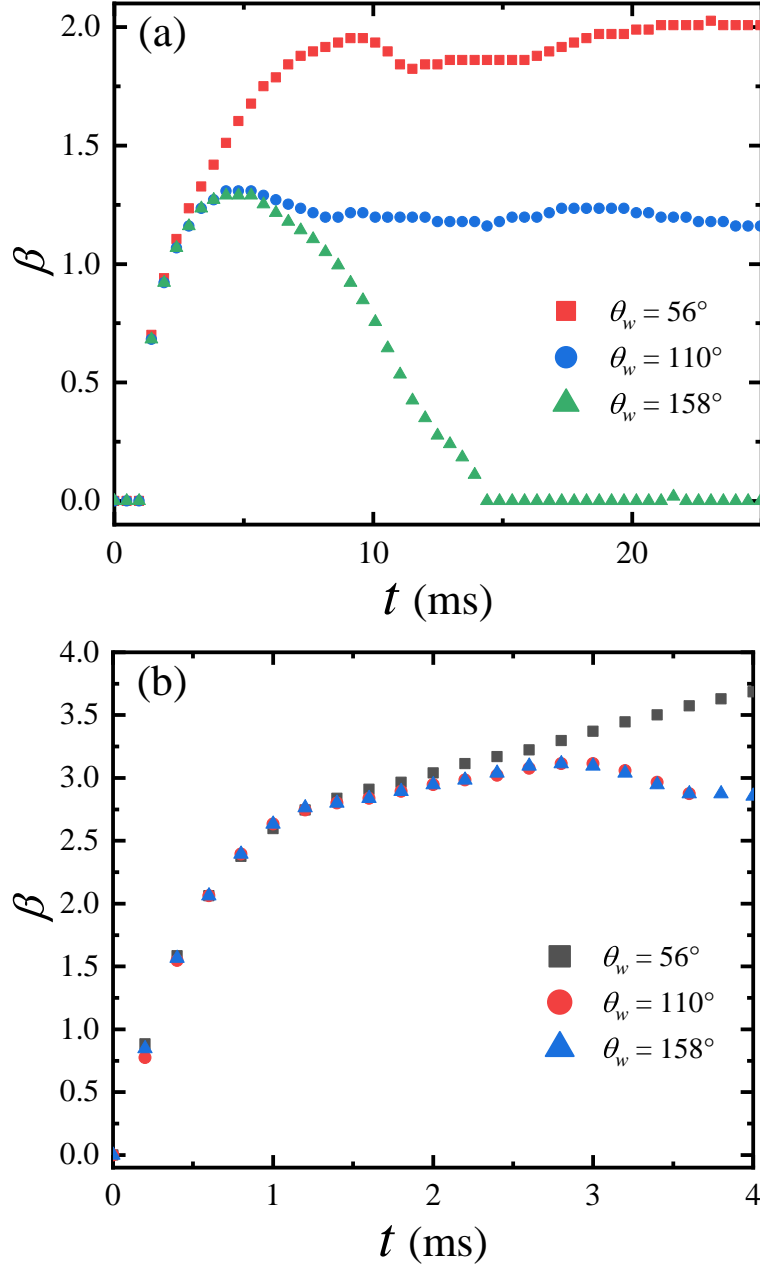


Figure 2.16. The simulation results of spreading factor,  $\beta$ , changing in time ( $t$ ) for different surface wettability ( $\theta_w$ ), under low and high Weber number situations of (a)  $We = 6.9$  and (b)  $We = 398$ .

sults [3, 24, 33]. To obtain a universal law of spreading factor, considering momentum conservation, Eggers et al. [24] derived equation relating spreading factor and function of

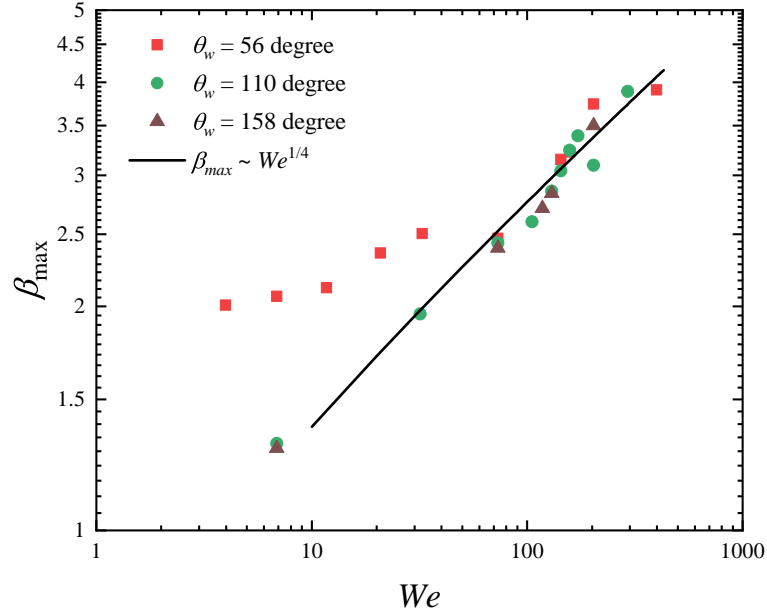


Figure 2.17. The relation between the maximum spreading factor,  $\beta_{max}$ , and  $We$  for different surfaces.

impact number  $P$ , as  $\beta = Re^{1/5} f(P)$ , where  $P = WeRe^{-4/5}$  and found droplet inertia dominants when  $P < 1$  but viscous dominants for  $P > 1$ . Lann et al. [28] further modified the definition of  $P$  to  $p = We \cdot Re^{-2/5}$ , so  $\beta = Re^{1/5} f(p)$  based on energy conservation and found a good agreement with experimental data using a non-Newtonian fluid [28]. Considering dynamic contact angle ( $\theta_d$ ), Pasandideh et al. [21] developed an expression based on energy conservation. Ukiwe et al. [22] improved Pasandideh's expression for surface energy and obtained a better agreement (with errors less than 10%) comparing with experimental data, as  $(We + 12)\beta = 8 + \beta^3(3(1 - \cos\theta_d) + 4We/\sqrt{Re})$ . Overall, the above expressions are found to be consistent with the authors' respective experimental or numerical data under various parameters.

For our numerical results on hydrophobic and superhydrophobic surfaces, the maximum spreading factor shows a nearly power-law relation that  $\beta_{max} \sim We^{1/4}$ . The same trend is found on the hydrophilic surface in the high- $We$  region. The 1/4 scaling law was modeled by Clanet et al. [23]. When the drop reaches its maximum spreading diameter in this model, the droplet deforms into a pancake shape. The droplet velocity reduces from  $V_I$

to zero within the time  $t = D_0/V_I$ , so this deceleration can be expressed as  $\gamma \sim V_I^2/D_0$ . They assumed the thickness of puddle similar to the capillary length,  $h \sim \sqrt{\sigma/(\rho\gamma)}$ , so based on volume conservation the spreading factor deduced as  $\beta_{max} \sim We^{1/4}$  [23]. Recent studies of drop impact on hydrophobic surface (with  $10 < We < 500$  experimentally) [31] and on superhydrophobic surfaces (with  $10^2 < We < 10^3$  experimentally and  $8 < We < 90$  numerically) [34, 54] are also consistent with this modeling of  $\beta \sim We^{1/4}$  power-law. Although this scaling law is used to fit experimental results, it yields a better agreement for hydrophobic surfaces. Furthermore, our numerical data suggest different scaling laws for a hydrophilic vs. (ultra)hydrophobic surface and, hence, the surface wettability effect should be taken into consideration for a unifying model for  $\beta$ .

## 2.4 Conclusions

We investigate drop dynamics and lamella spreading of a water droplet impacting onto hydrophilic, hydrophobic, and ultrahydrophobic surfaces using experiments and simulations. Our numerical model successfully reproduces almost all the dynamic events as the experimental results, especially with good agreement at the low- $We$  ( $< 30$ ) regime. We find that the slip length  $b$ , accounting for the friction force exerted on the droplet by the flat solid surface, is a vital factor to control the dissipation and thus affects impact dynamics. The slip length value should be varied as the surface wettability changes. By bench-marking with experimental spreading factor, the optimal  $b$ -values in the simulations are found to be 500 nm, 100 nm, and 10 nm for  $\theta_w = 56^\circ$ ,  $110^\circ$  and  $158^\circ$  respectively.

Through simulations, we find that as the impact speed increases, the droplet deformed extensively and moves violently in the vertical direction. In general, as  $V_I$  and, hence kinetic energy, is increased, the impact dynamics changes from deposition (at  $V_I = 0.35$  m/s) to splashing (at  $V_I = 2.5$  m/s) for both hydrophilic and hydrophobic surfaces. By contrast, a complete rebound occurs for SH surface at low and moderate  $V_I$  ( $= 0.5$  m/s), while splashing at large  $V_I$  ( $= 2.5$  m/s). At moderate speed ( $1$  m/s  $< V_I \lesssim 2$  m/s), bubble entrapment and subsequent jetting can be observed for all the surfaces, stem from lamella recoil due

to surface tension. The numerical results of flow and pressure fields, which are rarely obtained in experiments, provide insights into the droplet deformation and flow movement and explaining the resultant impact events under various parameters.

Surface wettability can significantly change the impact dynamics as well, especially in low- $We$  ( $= 6.9$ ) situations as shown in Fig.2.16(a). Most of our simulation results show a scaling law between the spreading factor and Weber number,  $\beta_{\max} = We^{1/4}$ , consistent with a simplified theoretical prediction. In this work, we provide a convenient simulation framework modeling the surface wettability with the direct input of the experimental wetting contact angle (i.e., static contact angle) without prior information of experimental dynamical contact angle. Furthermore, with slip length modeling the friction force at the wall, our simulation results show quantitative agreements of impact dynamics and spreading factor at low- $We$ , while qualitative at the high- $We$  regime. This slight discrepancy at high  $V_I$  suggests near-future investigations of (i)  $We$  (or  $Re$ )-dependent slip length and (ii) surface roughness effect, particularly  $\theta_w = 158^\circ$  to mimic realist superhydrophobic surfaces, commonly comprising of both hydrophobic coating and surface roughness or micro/nano-structures.

## Chapter 3

# Drop Impact Dynamics on a Heated Surface<sup>1</sup>

### 3.1 Introduction

Drop impact on heated surfaces has a broad range of applications, such as spray cooling [2], metallurgy [3] and fire fighting [5]. In addition to fluid flow, this case includes heat transfer and phase change and makes it more complex. Film evaporation, nucleate boiling, transition boiling, and film boiling are four distinct evaporation regimes observed experimentally [63]. Leidenfrost effect [68] is another interesting phenomenon to be observed and study. With the technology development, recent sophisticated tools make it possible to record impact dynamics and temperature fields during the whole process.

### 3.2 Experimental

The experimental setup of the drop impact on a heated surface is shown in Fig. 3.1. The Milli-Q water is used to generate a liquid droplet with density of  $\rho = 998 \text{ kg/m}^3$ , kinematic viscosity of  $\nu = 1 \times 10^{-6} \text{ m}^2/\text{s}$ , and surface tension of  $\sigma = 72 \times 10^{-3} \text{ N/m}$  under standard

---

<sup>1</sup>The material presented in this chapter is based on Yichi Zhang, Lihui Liu, and Peichun Amy Tsai, “High-speed drop dynamics and temperature variation during a water droplet impacting onto a heated flat surface,” in preparation (2021).

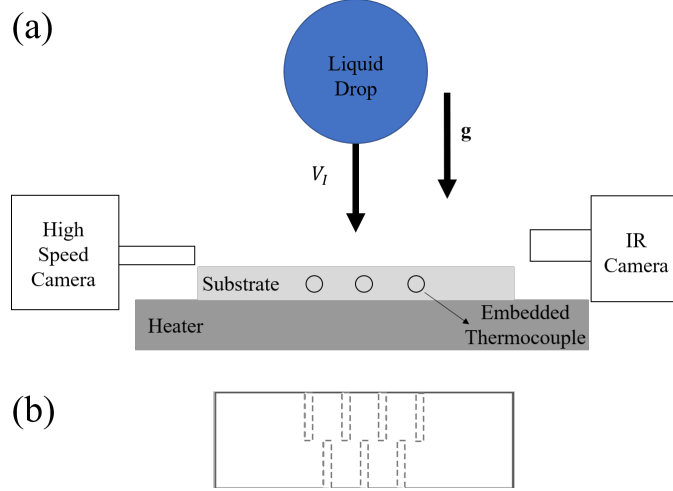


Figure 3.1. (a) Schematic experimental setup of temperature measurements during drop impact on a heated surface. (b) Embedded thermocouple position in glass.

atmosphere at room temperature ( $20^\circ\text{C}$ ). The droplet of an initial diameter of  $D_o = 2.35$  mm free falls from a certain initial height, in the range between 5 and 305 mm. The corresponding impact velocity varies between  $0.22 \leq V_I \leq 1.99$  m/s, determined by image analysis of tracking droplet trajectories. The dimensionless Weber and Reynolds numbers are estimated to be  $1.6 \leq We \leq 129.0$  and  $546.0 \leq Re \leq 4964.5$ . The former compares the droplet kinetic to surface energy, defined as:

$$We = \frac{\rho U^2 D}{\sigma}, \quad (3.1)$$

where  $\rho$ ,  $U$ ,  $D$  and  $\sigma$  represent liquid density, impact velocity, droplet diameter, and surface tension, respectively. The latter characterizes the inertia to viscous effect and is defined as:

$$Re = \frac{\rho U D}{\mu}, \quad (3.2)$$

where  $\mu$  represents the dynamic viscosity of the liquid.

The solid surface (of the size of  $40 \text{ mm} \times 20 \text{ mm} \times 7 \text{ mm}$ ) is a quartz glass, which is placed on a commercial heater (C-MAG HP 7, IKA Corp) to achieve the desired surface temperature,  $T_s$ , varied between 100 and  $450^\circ\text{C}$ . To monitor the surface temperature change, there are seven holes ( $\varnothing = 1.1 \times 10 \text{ mm}$ ) drilled 1.1 mm below the surface to embed

k-type thermocouple with diameter of  $\varnothing = 1$  mm and spacing of 2.5 mm as shown in Fig. 3.1b. A portable USB data acquisition module (OM-DAQ-USB-2401) is used to record the measurements of surface temperature. The maximum sample rate is 1000 Hz but divided across all active channels. Due to drop spreading and uncertain fixed spot for the initial impact point, all seven channels are used to record the solid temperature. The measurement ranges for the module and thermocouple are between  $-129$  and  $1372$  °C, with the accuracies are  $1.2$  °C and  $1.0$  °C, respectively. Hence, overall the temperature measuring accuracy is about  $2$  °C.

In addition, an Infrared(IR) camera (X8500sc MWIR, FLIR) was placed from the side to record droplet temperature change. All objects at temperatures above absolute zero emit thermal radiation. An IR camera can detect this radiation by receiving signal in the specific infrared spectral band [108]. By default, the IR camera will stream data in signal mode, producing values called 'counts'. These 'counts' values cannot easily be converted to a temperature value. The 'temperature' mode is then used directly, allowing the conversion from 'count' to 'temperature' on the camera [109]. Moreover, the amount of thermal radiation emitted depends on the emissivity of the object's surface. For our case, water is the object with a high emissivity (of  $\approx 0.95$ ), with which reflected temperature from other objects has a less influence. Although the droplet is semi-transparent, we assured the background with lower temperature than that of the droplet. Proper parameters of emissivity and surrounding temperature were input in IR camera for adjustment and compensation calculation. Different combinations of lenses can lead to different measuring ranges, but in our experiments, we only selected four settings listed in Table 3.1. The calibration of the camera is done by the company; the accuracy is about  $\pm 2^\circ\text{C}$  for temperature  $T \leq 100^\circ\text{C}$ , while 2% of reading for  $T > 100^\circ\text{C}$ . The lens (FPO Manual Bayonet [3-5  $\mu\text{m}$ , 50mm, f/2.5]) used for the IR camera is with a spectral band of 3-5  $\mu\text{m}$ , a focal length of 50 mm, the aperture of f/2.5, the full resolution of  $1280 \times 1024$  pixels, field of view of  $17.46^\circ$ , and close focus 0.5 m. Simultaneously, the combination of a high-speed camera (Photron Nova S9) and zoom lens (Navitar 12 $\times$  zoom combination) records the side-view of the entire impact-

ing process at 10,000 fps with the working distance 165 mm and magnification of 0.58× to 7×. For each condition, three independent experiments were carried out to ensure the data reproducibility.

Table 3.1

Summary of IR camera measuring range and corresponding accuracy.

Measurement range (°C)	Frame rate (fps)	Accuracy
10 – 90	500	±2°C
35 – 150	1000	≈ 2% of Reading
80 – 200	1000	≈ 2% of Reading
150 – 350	1000	≈ 2% of Reading

### 3.3 Results and discussion

In this section, we will systematically demonstrate and discuss the results of water drop impact on a heated surface at different  $T_s$ , ranging from 100°C to 450°C. These are high-speed images separated into 3 groups by different  $We$  values: low- $We$  ( $We = 1.6$ ), medium- $We$  ( $We = 27$ ), and high- $We$  ( $We = 129$ ), recorded by a high-speed camera and an IR camera.

#### 3.3.1 High-speed-imaging results of drop impact dynamics

The impact dynamics recorded by the high-speed camera are shown in Fig. 3.2 – 3.4. To better analyze the effect of surface temperature on the impact dynamics, results of the droplet with the same initial height (i.e., same  $We$ ) are plotted together. The sequential images varying with time are plotted in the same row, surface temperature  $T_s$  is increased from the top to bottom (from 100°C to 450°C). Due to the heated surfaces, all the liquid droplets evaporated at the end, but we focused on the early-time impact events before complete evaporation.

At low- $We$  situation (i.e.,  $We = 1.6$ ), as shown in Fig. 3.2 (a), the liquid drop impacts on the heated surface and subsequently deposits on it while evaporating at  $T_s = 100^\circ\text{C}$ . As  $T_s$  increased to  $200^\circ\text{C}$ , the whole dynamics similar to the previous one, but starting from 10 ms, small air bubbles associated with boiling/evaporation appear inside the droplet. This is reasonable since the evaporation happens earlier as  $T_s$  is increased.

When surface temperature continues increasing to  $T_s = 350^\circ\text{C}$ , another specific event of rebound is observed. After impact, the droplet quickly recoils and then totally bounces up, which is the result of the Leidenfrost effect [70]. As the surface temperature,  $T_s$ , is higher than the Leidenfrost point [70, 110], an insulating vapor layer is produced underneath, keeps the droplet from direct contact with the heated surface, and hinders the heat transfer from the surface. The vapor layer eventually levitates the droplets and inhibits fast evaporation. Our result reveals that the Leidenfrost temperature for this liquid-solid combination (of water and glass) is between  $200^\circ\text{C}$  to  $350^\circ\text{C}$ . More experiments in this temperature range are needed to locate  $T_L^D$  precisely. When  $T_s$  reaches to  $450^\circ\text{C}$ , the impact dynamics are similar to  $T_s = 350^\circ\text{C}$ , showing a complete rebound within 15 ms as well.

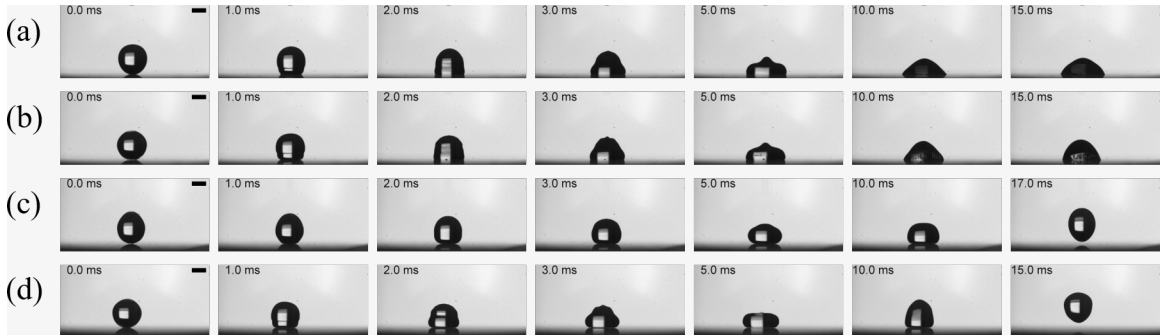


Figure 3.2. Sequential high-speed snapshots of water drop impacting at  $We = 1.6$  on a flat, heated glass surface. The surface temperature is increased from top to bottom, with (a)  $T_s = 100^\circ\text{C}$ , (b)  $T_s = 200^\circ\text{C}$ , (c)  $T_s = 350^\circ\text{C}$  and (d)  $T_s = 450^\circ\text{C}$ . The length bars represent 1 mm.

When the initial position of droplets moved higher, the corresponding  $We$  increased to a specified medium value ( $We = 27$ ). Fig. 3.3 shows the sequential images for  $We = 27$  ( $V_I = 0.9$  m/s) at various high  $T_s$ . When surface temperature  $T_s \leq 200^\circ\text{C}$ , the impact

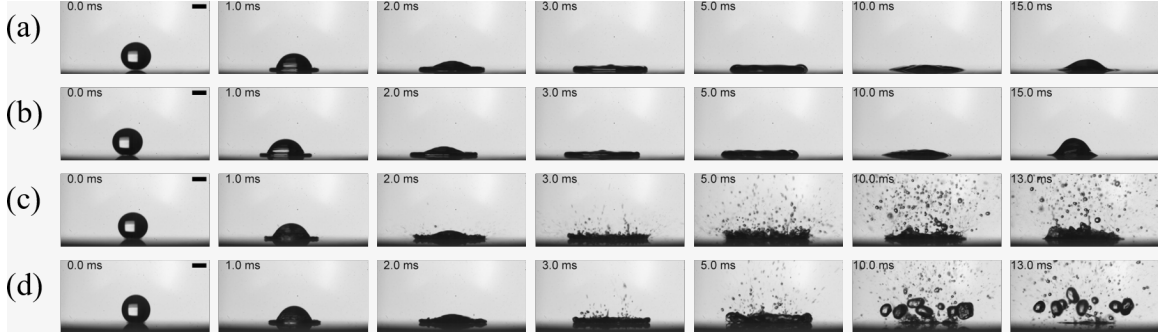


Figure 3.3. Sequential images of high-speed recordings of water drop impact at  $We = 27$  on a heated surface. The surface temperature is increasing from top to bottom that, (a)  $T_s = 100^\circ C$ , (b)  $T_s = 200^\circ C$ , (c)  $T_s = 350^\circ C$  and (d)  $T_s = 450^\circ C$ . The length bars represent 1 mm.

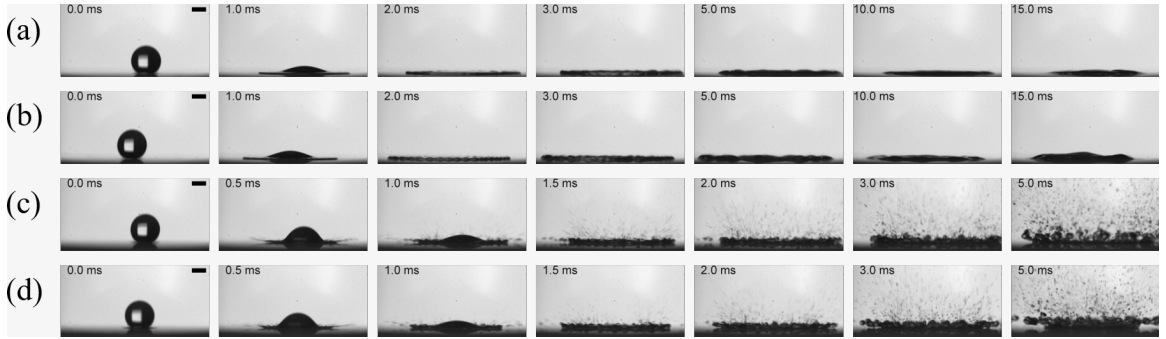


Figure 3.4. Sequential images of high speed camera results of water drop impact at  $We = 129$ , on heated surface. The surface temperature is increasing from top to bottom that, (a)  $T_s = 100^\circ C$ , (b)  $T_s = 200^\circ C$ , (c)  $T_s = 350^\circ C$  and (d)  $T_s = 450^\circ C$ . The length bars represent 1 mm.

dynamics is similar to that at low  $We$  situation, forming a spreading and subsequently a deposition. However, the higher impact velocity makes the drop spreading more. As  $T_s$  is above the saturation (or boiling) temperature ( $T_{sat} = 100^\circ C$ ), bubbles are created at the liquid-solid interface due to the nucleate boiling [9]. In this nucleate boiling region, isolated bubbles form at nucleate sites when the surface temperature is slightly above  $T_{sat}$  (see Fig. 1.5). When  $T_s$  becomes sufficiently high (around  $300^\circ C$  in our experiment), a large number of bubbles are formed and ejected violently from the free surface, resulting in secondary atomization, as shown in Fig. 3.3 (c). This event is denoted as spreading with

atomization, with tiny droplets of a typical size of  $\approx 10\mu\text{m}$ . When  $T_s = 400^\circ\text{C}$ , in addition to secondary atomization, liquid droplet also breaks up into several secondary droplets (of the typical size of  $\approx 100\mu\text{m}$ ) and then splashes outwards; we term this event as splashing breakup with atomization.

As  $We$  is increased to a high value ( $We = 129$ ), the impact dynamics can be easily split into two typical outcomes: (i) spreading at low  $T_s$  and (ii) splashing breakup with atomization at high  $T_s$ . When  $T_s$  is relatively low ( $T_s \leq 200^\circ\text{C}$ ), as  $We$  increased, the droplet spreads more widely and even shows the fingering, which might be the omen of splashing. It can be anticipated that when  $We$  continues to increase, the splashing event may finally happen at low  $T_s$ . At high  $T_s$  ( $T_s \geq 350^\circ\text{C}$ ), because of the high  $We$  and high  $T_s$ , splashing can be observed in the early stage. Moreover, the secondary droplets seem smaller but more than those at medium  $We$  ( $= 27$ ). At the same  $T_s = 450^\circ\text{C}$ , secondary droplets can be observed at both  $We = 27$  and  $We = 129$ , but the droplets' sizes become smaller and more at high  $We$ . Larger  $We$ , corresponding to higher kinetic energy, makes the droplet break up into smaller pieces. Since the total drop volume is conserved, the number of secondary droplets enlarges at high  $We$ .

### 3.3.2 High-speed IR recordings of drop impact dynamics

The droplet temperature variation is recorded by IR camera and shown in Fig. 3.5 to 3.7. Similar to discussion of high-speed camera results, we grouped the results with the same  $We$  together to clearly show the temperature effect. In each image set, surface temperature  $T_s$  is increased from the top to bottom row. As listed in Table. 3.1, we mainly use measuring range of  $10^\circ\text{C} - 90^\circ\text{C}$  and  $35^\circ\text{C} - 150^\circ\text{C}$  to focus on droplet temperature variation.

The bottom red and yellow regions in Fig. 3.5 to 3.7 are heated quartz glass surfaces, whose temperature is usually above the temperature range set. Since the IR side-view cannot read the surface temperature accurately, the measurement of  $T_s$  is reported based on the thermocouple recordings. However, if  $T_s$  is within the range, the IR recording agrees with the thermocouple results within a difference of  $2^\circ\text{C}$ .

At low-Weber ( $We = 1.6$ ), the IR high-speed recordings shown in Fig. 3.5 reveal a droplet spreading for low  $T_s$  range ( $T_s = 100^\circ\text{C}$  and  $200^\circ\text{C}$ ) and totally rebound for high- $T_s$  range ( $T_s = 350^\circ\text{C}$  and  $450^\circ\text{C}$ ), in agreement with high-speed camera results. As the lower half of the droplet is closer to the hot surfaces, it shows higher temperature compared to the upper part and is increased with  $T_s$ . When  $T_s = 100^\circ\text{C}$ , the upper and lower drop show different temperature before impact, the whole droplet temperature gradually increases and becomes similar everywhere around  $40^\circ\text{C}$  at 12 ms.

As  $T_s$  is increased to  $200^\circ\text{C}$ , higher surface temperature makes the droplet temperature  $T_d$  increase faster and reach a higher temperature around  $70^\circ\text{C}$  in same time period (within 12 ms). At high surface temperature ( $T_s = 350$  and  $450^\circ\text{C}$ ), the totally rebound is observed from the IR recordings as well. Due to the low initial position of the droplet, the green rectangular shown in Fig. 3.3 (c) is the metal needle whose tip is heated and similar to  $T_s$  because of the close distance and high conductivity of the metal. The IR results show that the region beneath the complete rebound is a vapor layer created, preventing the droplet from direct contact with the heated surface. Therefore, the IR images show insignificant change of the droplet temperature  $T_d$ . We will show and discuss the detailed recordings analyzed in Section 4.3.

Revealed in Fig. 3.6 are the high-speed recordings of drop impact on a heated surface at  $We = 27$ , at various high  $T_s$ . In a few images, droplets were not captured clearly due to higher velocity. As listed in Table. 3.1, the frame rate of the IR camera is much less than the high-speed camera. In the low- $T_s$  range ( $T_s = 100^\circ\text{C}$  and  $200^\circ\text{C}$ ), the droplet spreads and then recoils. Because of higher impact velocity (or higher  $We$ ), droplet spreads more and becomes thinner from the side-view recordings. Unlike high-speed black and white recordings with a high degree of contrast, the temperature field changes gradually and continuously, and the droplet shape is not clear within the spreading process from 4 ms to 12 ms in Fig. 3.6 (a) and (b). A droplet shows a similar spreading dynamics in both low- $We$  and medium- $We$  at  $T_s = 100^\circ\text{C}$  and  $200^\circ\text{C}$ , as shown in Fig. 3.5 a-b and Fig. 3.6 a-b, while the droplet temperatures are similar around  $70^\circ\text{C}$ . Therefore, different  $We$  seems to have an

insignificant effect on  $T_d$  due to similar impact events, while the surface temperature seems to be a dominant factor.

As demonstrated in the high-speed results, in the high- $T_s$  range ( $T_s = 350^\circ\text{C}$  and  $450^\circ\text{C}$ ), the atomization is observed (at  $\approx 4$  ms) from the IR results as well, which agrees with time-stamp shown in Fig. 3.3. The atomization is more violent compared to high-speed image results. In addition, secondary droplets could be found in the IR results with small circular shape.

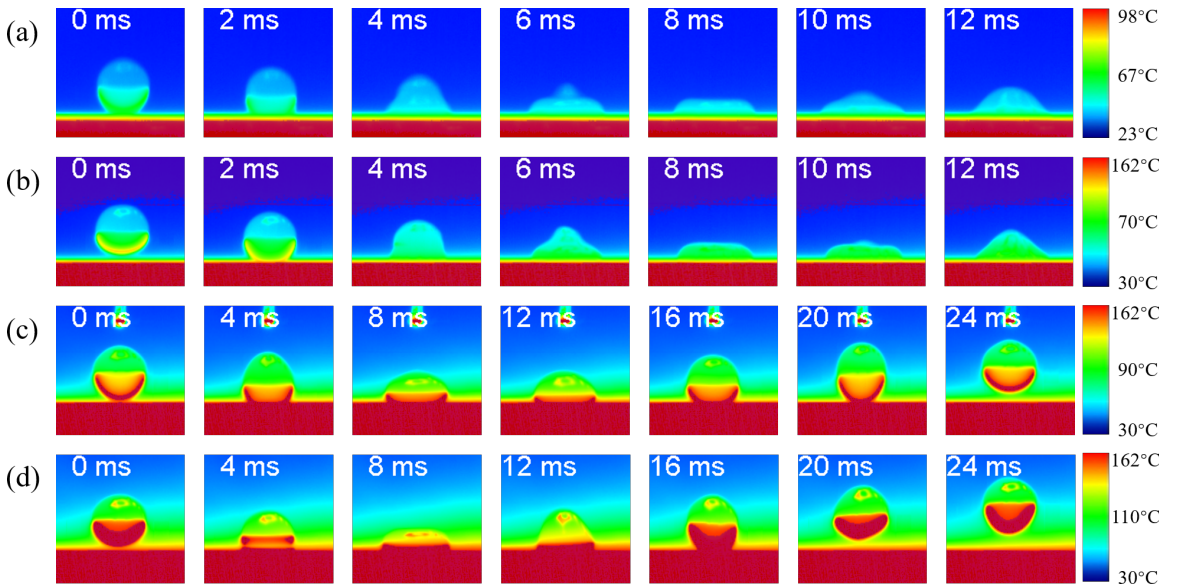


Figure 3.5. Sequential images of high-speed IR results of water drop impact at  $We = 1.6$ , on a heated glass surface. The surface temperature is increasing from top to bottom that, (a)  $T_s = 100^\circ\text{C}$ , (b)  $T_s = 200^\circ\text{C}$ , (c)  $T_s = 350^\circ\text{C}$ , and (d)  $T_s = 450^\circ\text{C}$ .

The initial fuzzier high-speed IR images in Fig. 3.7 is due to a faster impact at a greater  $We = 129$ . High- $We$  impact makes the droplet spread more and become thinner shape at low  $T_s$  range ( $T_s = 100^\circ\text{C}$  and  $200^\circ\text{C}$ ), which is not easy to observe by IR camera. The droplet temperature  $T_d$  is similar to those of medium- and low-  $We$ ,  $T_d \approx 70^\circ\text{C}$ , droplet still spread at same  $T_s$ , but higher  $We$ . Fig. 3.7 (c) and (d) show violent atomization as well in the high- $T_s$  range, but higher  $T_s$  may leads to drop splash more wildly, which cannot be easily read from the high-speed images at these parameters (e.g., Fig. 3.4).

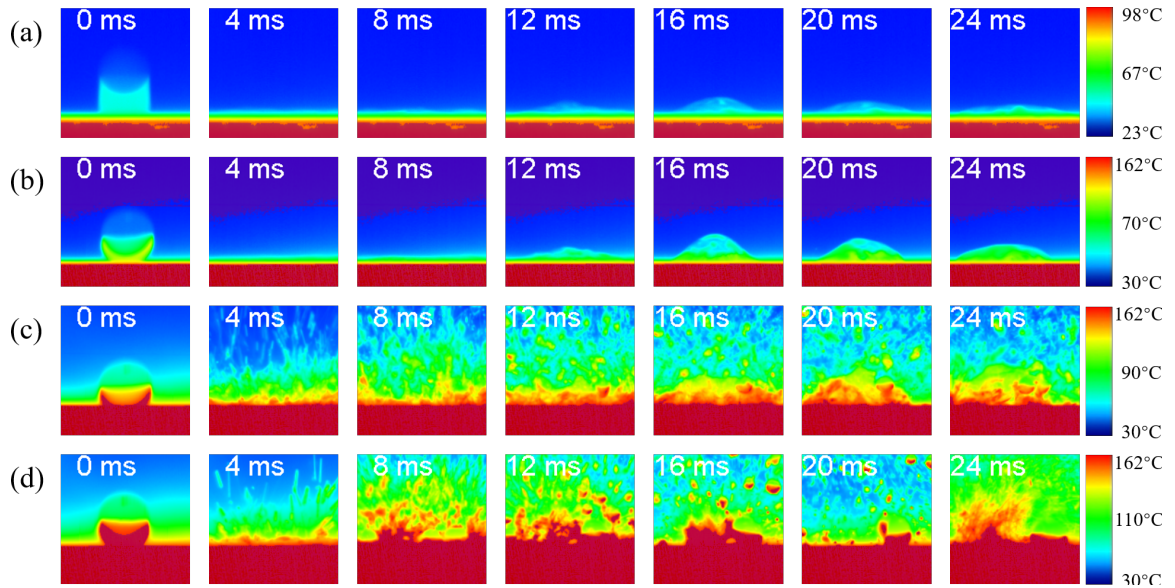


Figure 3.6. Sequential images of IR results of water drop impact at  $We = 27$ , on heated surface. The surface temperature is increasing from top to bottom that, (a)  $T_s = 100^\circ\text{C}$ , (b)  $T_s = 200^\circ\text{C}$ , (c)  $T_s = 350^\circ\text{C}$  and (d)  $T_s = 450^\circ\text{C}$ .

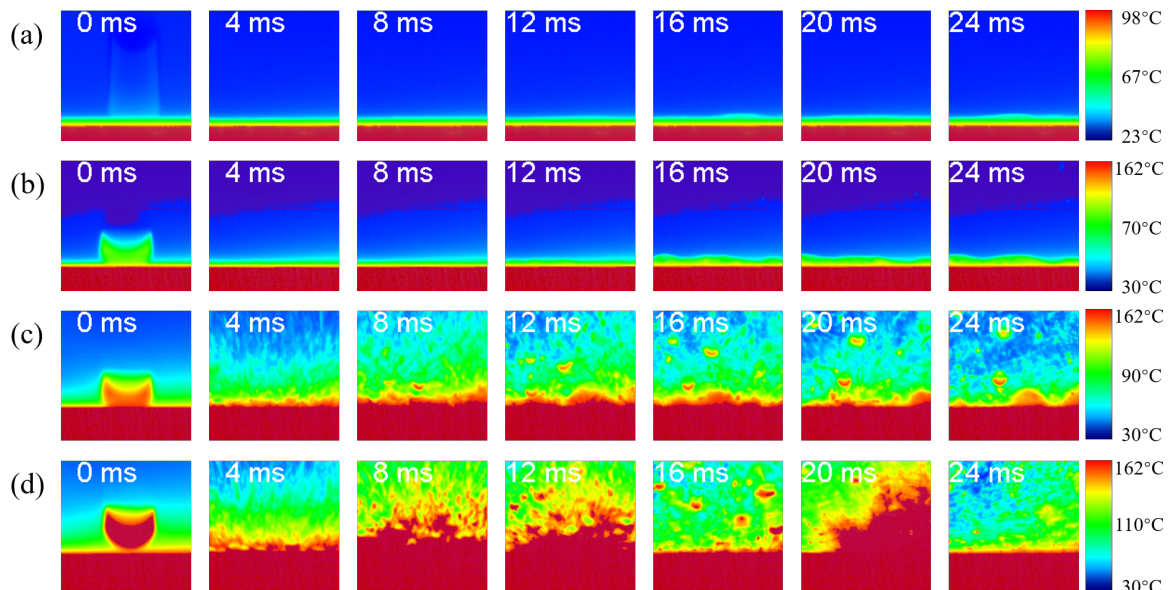


Figure 3.7. Sequential images of high-speed IR results of water drop impact at  $We = 129$ , on a flat, heated glass surface. The surface temperature is increasing from top to bottom: (a)  $T_s = 100^\circ\text{C}$ , (b)  $T_s = 200^\circ\text{C}$ , (c)  $T_s = 350^\circ\text{C}$ , and (d)  $T_s = 450^\circ\text{C}$ .

### 3.4 Summary

In this Chapter, systematic experimental results of drop impact events on heated surfaces recorded by a high-speed camera and an IR camera are demonstrated. The high-speed camera with a relatively high recording rate enables clear observations of various drop impact dynamics on a heated, flat surface. With the increase of surface temperature  $T_s$  (100°C to 450°C) and  $We$  (1.6 to 129), spreading, totally rebound, spreading with atomization and splashing breakup with atomization are observed experimentally. The dynamic Leidenfrost point  $T_L^D$  for our experiments is found to be in the range between 200°C and 350°C at  $We = 1.6$ . The IR camera recordings reveal temperature variations of the droplet and surface. During the spreading phenomenon, the droplet temperature is around 70°C for all  $We$ . For the completely rebound event occurring at  $We = 1.6$ ,  $T_s = 350^\circ\text{C}$  and  $450^\circ\text{C}$ , the droplet temperature does not seem to change since an insulating vapor film hinders the heat transfer process due to the Leidenfrost effect. The detailed temperature analysis will be described in the next Chapter.

## Chapter 4

# Temperature Variation during Drop Impact on a Heated Surface <sup>1</sup>

### 4.1 Introduction

It is vital to investigate the temperature variation of both drop and solid surfaces during drop impact processes to understand liquid-wall heat transfer phenomena, which have numerous spraying, cooling, coating, and fire suppression applications. However, there are relatively limited data and measurements of temperature profiles and changes, compared to drop motion and dynamics recordings, during impact on heated surfaces. Recently, one of the feasible technologies for temperature measurements is an Infrared (IR) camera, which has been commonly used to measure temperature remotely without direct contact and to validate associated heat transfer models [86, 111, 87, 88]. However, due to an IR camera's relatively low frame rate compared to a standard high-speed imaging camera, the IR measurements' accuracy is not adequate. Researchers also have tried to use other methods to achieve accurate temperature measurements, such as two-color laser-induced fluorescence (2cLIF) [87] and micro-electromechanical system (MEMS) [89] albeit with some technical

---

<sup>1</sup>The material presented in this chapter is based on Yichi Zhang, Lihui Liu, and Peichun Amy Tsai, "High-speed drop dynamics and temperature variation during a water droplet impacting onto a heated flat surface," in preparation (2021).

limitations. Furthermore, due to the above experimental limitations, the measurements of temperature field for the drop impact problem on a heated surface is relatively rare in the literature, while most of the studies report high-speed imaging recordings of the drop impact dynamics. In this chapter, we analyze the experimental IR images presented in the previous chapter, mainly focusing on the temperature changes for the droplet and solid surface. In addition, a heat transfer analytical model is presented and compared with our experimental results.

## 4.2 Theoretical models

### 4.2.1 Convective heat transfer model of a heating droplet when impacting on a heated surface

In this subsection, we discuss the fluid and heat transport processes modeling a droplet impacting on a heated surface, depicted in Fig. 4.1. The relevant fluid and heat transport problems have been studied lately [87], and we discuss below the key theoretical modeling leading to the important results of droplet temperature change so as to compare with our experimental results. The temperature field,  $T$ , can be determined through the conservation of energy concept, and the heat transfer equation becomes to [87, 111]

$$\frac{\partial T}{\partial t} + \mathbf{U} \cdot \nabla T - a_l \nabla^2 T = 0, \quad (4.1)$$

where  $a_l = k_l/(\rho_l c_{p,l})$  is the thermal diffusivity of the liquid,  $T$  is temperature,  $U$  is velocity field, and  $k_l$ ,  $\rho_l$  and  $c_{p,l}$  are the thermal conductivity, liquid density and specific heat of the liquid, respectively.

As shown in Fig. 4.1, we can assume a 2D (axisymmetric) problem and neglect the inertia effect in the Navier-Stokes equations [100] when droplet impacting on the heated surface, since the thermal boundary layer thickness is far less than the droplet spreading and the problem can be modeled using the lubrication theory [87]. Hence, the thermal gradient in  $\hat{z}$  direction is much larger than that in the radial direction  $\hat{r}$ , i.e.,  $\frac{\partial T}{\partial z} \gg \frac{\partial T}{\partial r}$ . The liquid velocity in  $\hat{z}$  direction ( $v_{z,l}$ ) has been calculated by Yarin and Weiss (1995) [112], that in

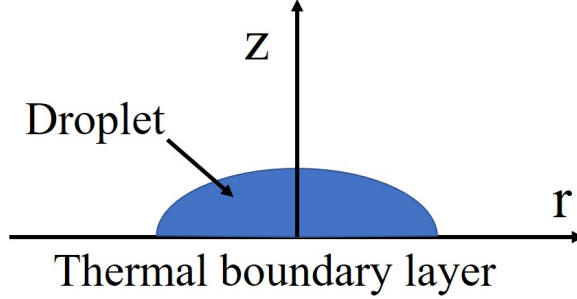


Figure 4.1. Schematic diagram of droplet spreading on a heated surface.

cylindrical coordinate system the inviscid remote asymptotic solution:

$$v_{z,l} = \frac{-2z}{t}, \quad (4.2)$$

where  $t$  is time.

The energy Eq. (4.1), hence, can be expressed as:

$$\frac{\partial T}{\partial t} - \frac{2z}{t} \frac{\partial T}{\partial z} = a_l \frac{\partial^2 T}{\partial z^2}. \quad (4.3)$$

The thickness of the thermal boundary layer has been denoted as  $\theta \sim \sqrt{a_l t}$  [111]. The typical time scale is  $t = D_0/U \approx 10^{-3}$  s. In our experiment, we use milli-Q water droplet, with  $\rho_l = 997$  kg/m<sup>3</sup>,  $k_l = 0.6$  W/(m · K), and  $c_{p,l} = 4200$  J/(kg · K). Since  $a_l = k_l/(\rho_l c_{p,l})$ , the corresponding thermal boundary layer thickness for the water drop is about  $\theta_d \sim \sqrt{a_l t} = \sqrt{1.42 \times 10^{-7} t} \approx 10^{-5}$  m. This justifies the reasonable assumption of small thickness of the thermal boundary layer.

To obtain the solution for  $T$ , a self-similar solution can be calculated by defining a similarity variable,  $\xi = \frac{z}{\sqrt{a_l t}}$ :

$$T'' + \frac{5}{2} \xi T' = 0. \quad (4.4)$$

The appropriate boundary conditions for  $T$  are given below. First, the temperature at the liquid-vapor interface is the saturation temperature:

$$T = T_{sat} \quad \text{at} \quad \xi = 0. \quad (4.5)$$

Because the thermal layer thickness is small in comparison to the drop thickness,

$$T = T_{d0} \quad \text{at } \xi \longrightarrow \infty, \quad (4.6)$$

where  $T_{d0}$  is the droplet temperature before impacting on the (heated) solid surface. The solution of Eq. (4.4) is [87]

$$T(z, t) = T_{sat} + (T_{d0} - T_{sat}) \cdot \operatorname{erf}\left(\frac{\sqrt{5}z}{2\sqrt{a_l t}}\right), \quad (4.7)$$

where erf is the error function.

The heat flux entering the liquid can be calculated by [87]

$$q_L = k_l \left(\frac{dT}{dz}\right)\Big|_{z=0^+} = \frac{\sqrt{5}e_l(T_{sat} - T_{d0})}{\sqrt{\pi}} t^{-1/2}. \quad (4.8)$$

Here,  $e_l = \sqrt{\rho_l c_{p,l} k_l}$  is the thermal effusivity of the liquid. The change of  $\Delta T_d$  in the mean temperature of the drop  $T_m$  can be calculated by

$$\Delta T_d = T_m - T_{d0} = \frac{1}{m c_{p,l}} \int_0^t q_L(t) \cdot S_e(t) dt, \quad (4.9)$$

where  $m = \frac{\pi}{2} \rho_l d_c^2 l_c$  is the droplet mass,  $S_e = \pi d_c^2 / 4$  is effective surface,  $l_c = \sqrt{\gamma / \rho_l g}$  is the capillary length,  $\gamma$  is the surface tension of the liquid, and  $d_c$  is contact diameter.

### 4.3 Results and discussion

Based on the high-speed and IR imaging results shown in Chapter 3, in this section, we summarize the drop impact dynamics and analyze the droplet and surface temperature changes. The analyses here aim at answering the following key research questions? How do the impact velocity ( $V_I$ ) and surface temperature ( $T_s$ ) affect the drop impact dynamics and outcomes? How much does the temperature change during the drop spreading or rebound? These questions are essential for associated technological applications, such as spray cooling, coating, and combustion.

### 4.3.1 Phase diagram of drop impact dynamics on a heated, flat surface

Fig. 4.2 shows the phase diagram of drop impact outcomes under the influence of  $We$  and  $T_s$  by analyzing all the high-speed camera recordings obtained at different experimental parameters of  $T_s$  and  $V_I$ . We observe and classify the drop impact events on a heated surface into four different types: spreading/deposition, totally rebound, spreading with atomization, and splashing breakup with atomization.

For the experimental parameter ranges explored ( $0 < We \leq 129$  and  $0 < T_s \leq 450^\circ\text{C}$ ), *spreading* is the only result observed in relatively low surface temperature range ( $T_s = 100$  and  $200^\circ\text{C}$ ). When  $T_s = 300^\circ\text{C}$ , higher  $T_s$  leads to the atomization, manifested in small tiny droplets shown in Fig. 4.2 snapshot ( $\bullet$ ), due to nucleate boiling besides drop spreading. When  $T_s$  reaches  $350^\circ\text{C}$ , a totally rebound ( $\blacktriangle$ ), the so-called Leidenfrost effect [70], can be observed at low- $We$  situation ( $We \approx 1.6-4.5$ ). In our experiments, the dynamic Leidenfrost point [70, 110] is between  $300^\circ\text{C}$  and  $350^\circ\text{C}$ , indicating a high temperature-so-called film boiling-regime [9].

At high ( $T_s \geq 350^\circ\text{C}$ ),  $We$  can affect the impact outcome significantly. As  $We$  increases, the impact event changes from totally rebound to spreading with atomization, and finally to splashing breakup with atomization, as higher kinetic energy makes the droplet motion more wildly. Although the rebound behavior here is similar to rebound on unheated surfaces, the fundamental mechanism is different [9]. For unheated hydrophobic surfaces, the rebound is influenced by the liquid-solid contact angle [113, 114]. As for a total rebound on heated surfaces at high- $T_s$ , it is affected by pressure from the vapor layer [9]. When  $T_s = 350^\circ\text{C}$  and  $400^\circ\text{C}$ , we can only observe totally rebound at very low  $We$  ( $We = 1.6$ ), but as  $T_s$  increases, the this complete-rebound region expands to higher  $We$ .

The critical Weber number  $We_c$  required for water drop breakup after impact on the heated wall in the film boiling regime is reported to be significantly lower than it for impact on unheated dry wall [9]. Besides totally rebound, the (phase-diagram) region of splashing breakup with atomization (shown by  $\blacktriangledown$  in Fig. 4.2) expands as well when  $T_s$  increases. When  $T_s = 350^\circ\text{C}$ , the critical Weber number for the splashing breakup with atomization

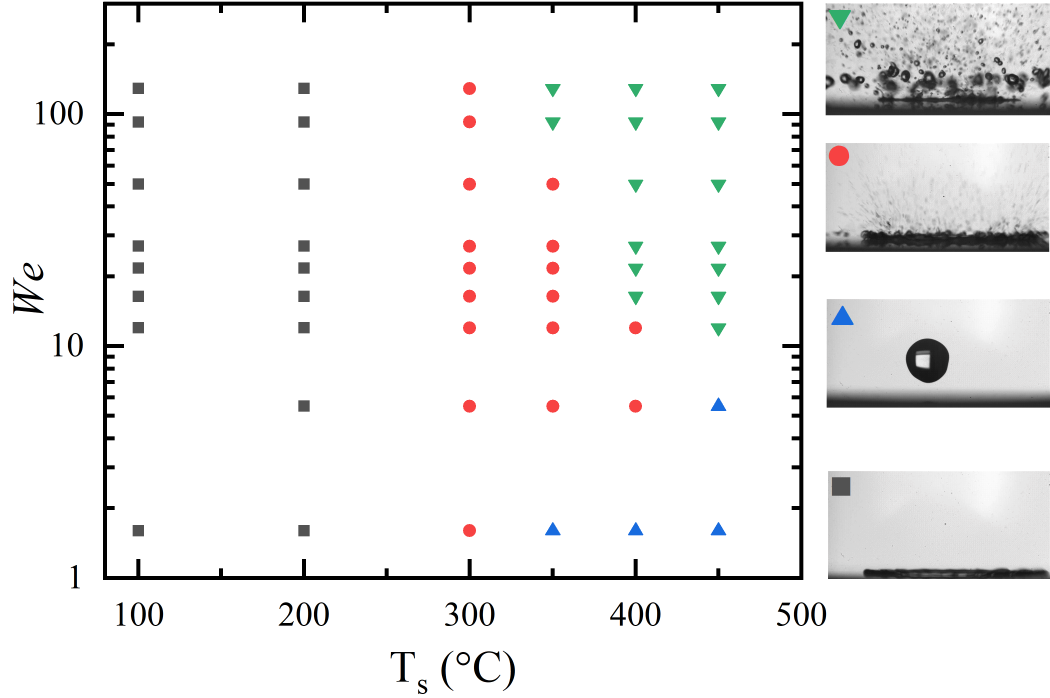


Figure 4.2. Phase diagram summarizing the dynamic events of drop impact on a heated flat surface. Four typical events are observed and shown on the right: spreading (■), totally rebound (▲), spreading with atomization (●), and splashing breakup with atomization (▼) (from bottom to top).

starts to be observed at  $We_c \approx 92.6$ . As  $T_s$  increases, the critical  $We_c$  continue decreases to  $We_c = 12$  at  $T_s = 450^\circ\text{C}$ . Corresponding to the expansion of these two events, the possibility of the presence of spreading with atomization decreases continually to zero at  $T_s = 450^\circ\text{C}$ . However, it is the only event to be observed at  $T_s = 300^\circ\text{C}$  when  $1.6 < We < 129$ . When the surface is unheated, spreading is influenced significantly by contact angle and surface roughness. However, for heated surfaces with  $T_s > T_L^D$ , the spreading is far less dependent on surface roughness with the existence of a vapor layer underneath the drop [9].

### 4.3.2 Droplet contact diameter

Based on the phase diagram in Fig. 4.2, the high temperature range ( $T_s \geq 350^\circ\text{C}$ ) is an interesting region to analyze in detail because the impact dynamics various significantly by

$We$ . As Eq. (4.9) shown, effective surface ( $S_e = \pi d_c^2/4$ ) of heat exchange is a key parameter determining the droplet temperature change during the impact. Therefore, the contact diameter ( $d_c$ ) plays an important role and has been analyzed from high-speed images and shown in Fig. 4.3.

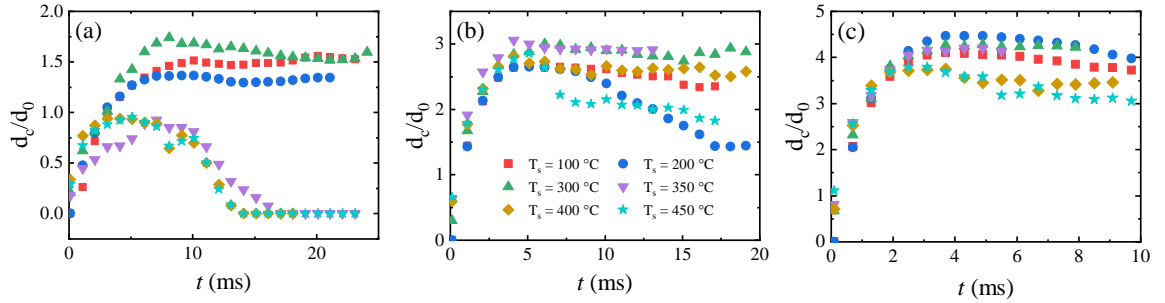


Figure 4.3. Time evolution of contact diameter  $d_c$  for different  $We$ , (a)  $We = 1.6$ , (b)  $We = 27$  and (c)  $We = 129$  at surface temperature  $T_s = 100^\circ\text{C}$ ,  $200^\circ\text{C}$ ,  $300^\circ\text{C}$ ,  $350^\circ\text{C}$ ,  $400^\circ\text{C}$ , and  $450^\circ\text{C}$  respectively.

The ratio of contact diameter ( $d_c$ ) and droplet initial diameter ( $d_0$ ) is plotted varying with time for  $T_s = 100^\circ\text{C}$  to  $450^\circ\text{C}$  at three different  $We$ . In Fig. 4.3 (a), the data shows a complete rebound for  $T_s = 350^\circ\text{C}$ ,  $400^\circ\text{C}$  and  $450^\circ\text{C}$  so the ratio increases first and decreases to zero (at  $t > 15$  ms). When  $T_s = 100^\circ\text{C}$  and  $200^\circ\text{C}$ , spreading is the major outcome, hence  $d_c$  increases in the early time, showing the spreading event. When  $T_s = 300^\circ\text{C}$ , a droplet spreading with atomization happens, similar spreading process can be read from the figure, but then the ratio decreases more as the droplet recoils more after the maximal spreading. When  $We = 27$ , the results on all surface temperature looks similar, except  $T_s = 200^\circ\text{C}$  and  $450^\circ\text{C}$ , which decreases significantly after reaching maximal point. When  $We = 129$ , all results almost overlap. Additionally, the maximum point increased by  $We$ . High kinetic energy makes the drop spreading more, so the maximum contact diameter increases by  $We$ .

### 4.3.3 Droplet Temperature Change

From Eq. (4.8) and Eq. (4.9) the change of droplet temperature ( $\Delta T_d$ ) can be calculated theoretically once we have the time evolution data of effective surface,  $S_e$ . As described in previous section,  $S_e = \pi d_c^2/4$  [87], the results of  $S_e$  can be ready calculated after the analysis of contact diameter  $d_c$ . Fig. 4.4 shows the comparison between the experimental results and theoretical predictions of the droplet temperature change at three different  $We$  at  $T_s = 100^\circ\text{C}$ . Overall, a good agreement between experimental results and theoretical model can be obtained. Within about 15 ms, the mean droplet temperature increases about  $2^\circ\text{C}$  through all different  $We$  conditions. When  $T_s = 100^\circ\text{C}$ , the main outcome of drop impact is spreading, and the corresponding results needed to be analyzed from images are more accurate. Although the temperature around the Leidenfrost is of interest, violent drop motion (e.g., atomization) makes both droplet temperature and contact diameter hard to analyze. Overall, the experimental measurements of drop temperature change shows an increase by  $We$  from 1.6 to 27 – 129 and also increased by  $T_s$  from  $350^\circ\text{C}$  to  $400 - 450^\circ\text{C}$ . These data are overall consistent with theoretical predictions in terms of the order of magnitude. Due to an insulated vapor layer formed underneath the droplet when  $T_s$  after Leidenfrost point, the droplet avoids directly contacting with heated surfaces, then droplet temperature almost keeps the same after impact when  $We = 1.6$ , see Fig. 4.5(a).

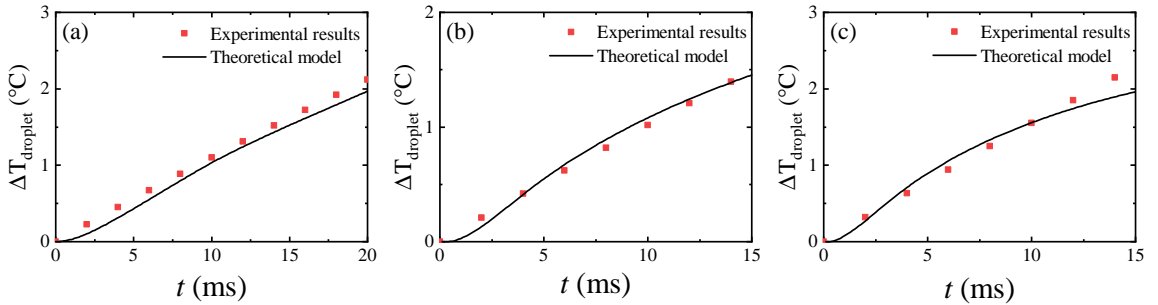


Figure 4.4. Time evolution of droplet temperature  $T_d$  change for different  $We$ , (a)  $We = 1.6$ , (b)  $We = 27$  and (c)  $We = 129$  at surface temperature  $T_s = 100^\circ\text{C}$ .

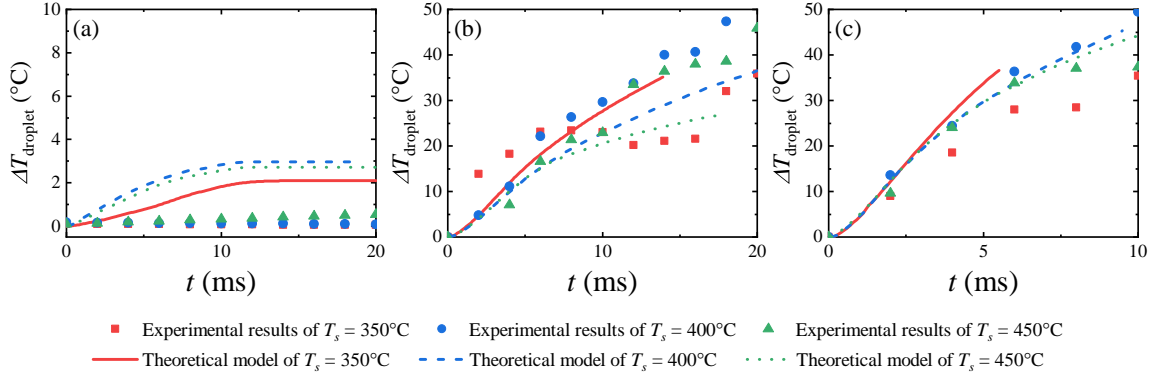


Figure 4.5. Time evolution of droplet temperature  $T_d$  change for different  $We$ , (a)  $We = 1.6$ , (b)  $We = 27$  and (c)  $We = 129$  at surface temperature  $T_s = 300^\circ\text{C}$ .

#### 4.3.4 Surface temperature change

The surface temperature is measured using thermocouples, which yield better accuracy than an IR camera. Due to different time taking for droplets fully evaporated, we control the time variable. We only focus on the surface temperature change in 2 seconds after the droplet contacts with the surface. Since we open all seven channels of the acquisition module and temperature recording. The voltage difference takes the differential signal from the two-wire. the maximum recording rate for our experiment is about 71.4 Hz, corresponding to a time difference is about 14 ms.

The thermocouple recording of surface temperature is shown in the following figures (Fig. 4.6 – Fig. 4.9). When  $T_s = 100^\circ\text{C}$ , droplet spreads on the surface at  $We = 1.6$ , some channels clearly capture the surface temperature decreasing (maximum  $\approx 12^\circ\text{C}$ ), especially channel 2 and 6 (see Fig. 4.6). As  $We$  increases to 129, the maximum cooling is similar to that at low- $We$  (see Fig. 4.7). When  $T_s = 450^\circ\text{C}$ , above the Leidenfrost point, the droplet fully rebounds after impact at  $We = 1.6$  caused by an insulating vapor layer underneath the droplet. Hence, the droplet is not directly in contact with the heated surface. Therefore, the change of surface temperature is within  $1^\circ\text{C}$  and can be neglected (see Fig. 4.8). As  $We$  is increased to 129, the impact outcome is splashing breakup with atomization. The drop's violent motion and large deformation lead to a surface temperature change (captured by

four channels) with a maximum difference of about  $9^\circ\text{C}$ . However, the time required for the surface cooling (including the water evaporation process) to a minimum value is different for different impact dynamics. Here, we focus on the impact of droplet motion and dynamics on surface cooling and consider the recordings within the first two seconds after the impact.

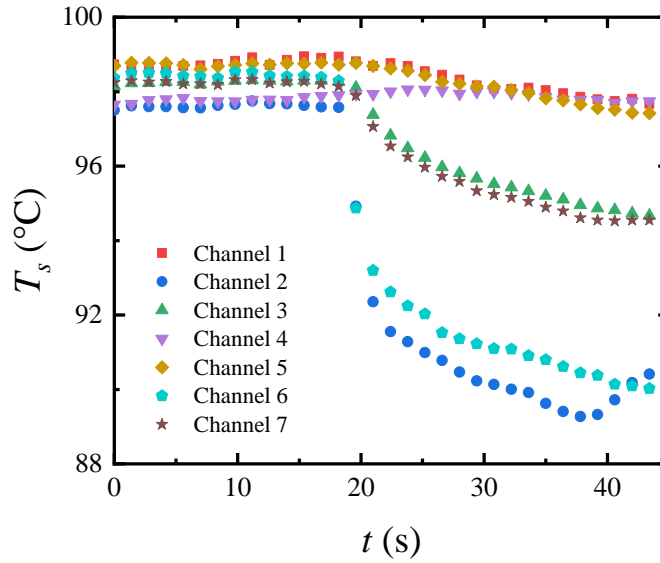


Figure 4.6. The surface temperature recorded by thermocouples at  $T_s = 100^\circ\text{C}$  and  $We = 1.6$ .

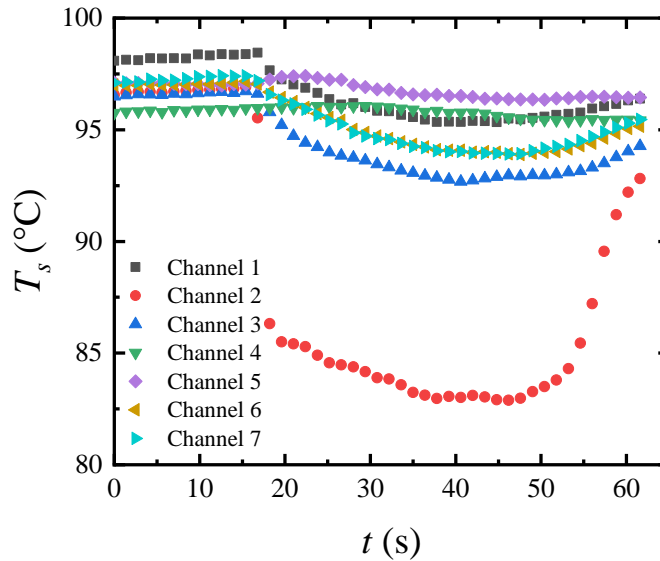


Figure 4.7. The surface temperature recorded by thermocouples at  $T_s = 100^\circ\text{C}$  and  $We = 129$ .

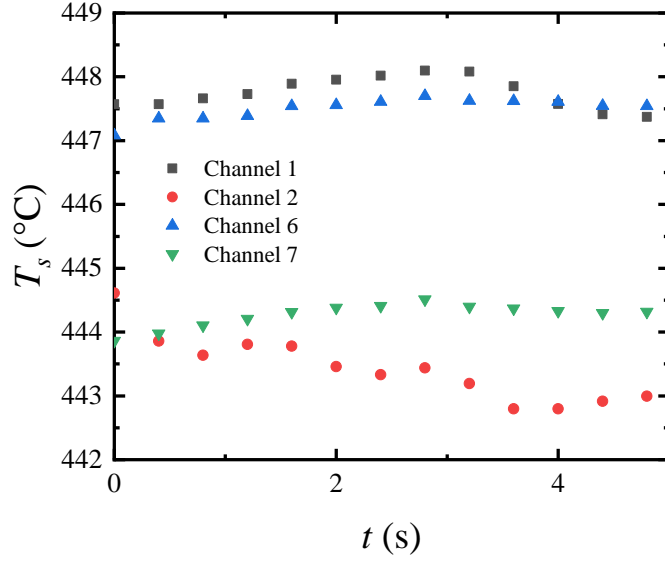


Figure 4.8. The surface temperature recorded by thermocouples at  $T_s = 450^\circ\text{C}$  and  $We = 1.6$ .

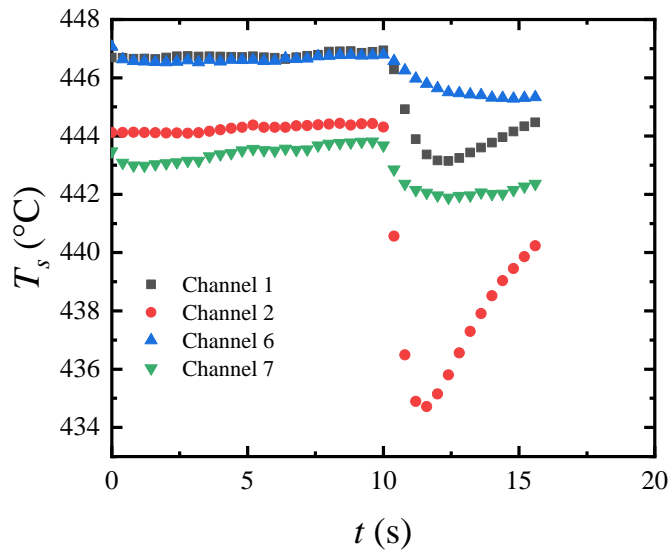


Figure 4.9. The surface temperature recorded by thermocouples at  $T_s = 450^\circ\text{C}$  and  $We = 129$ .

Besides the early stage, such as spreading, the evaporation process occurs and needs to be taken into consideration. The heated surface is cooling by drop impact, and we present the absolute value of surface temperature change in Fig. 4.10. From the experimental results, the solid temperature change by the drop impact cooling depends on both  $We$  and  $T_s$ .

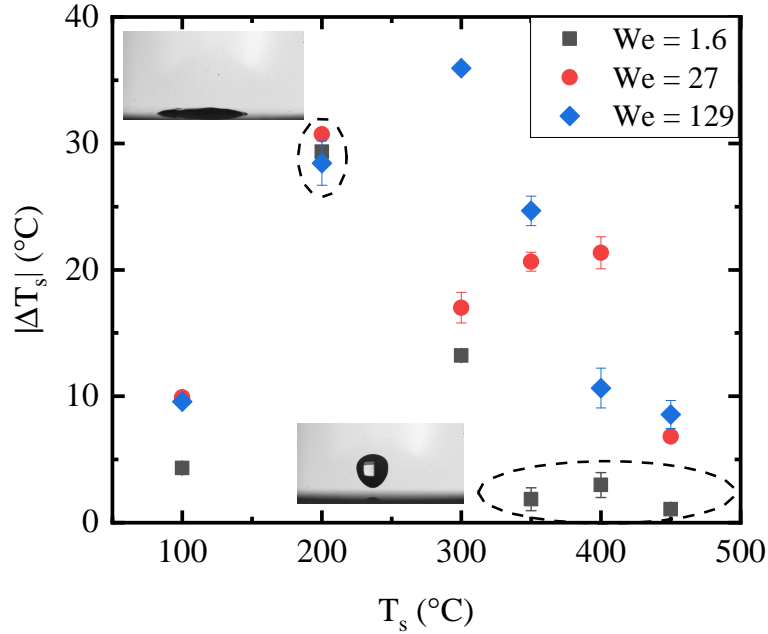


Figure 4.10. Surface temperature change in two seconds after drop impact on the surface at different setting temperature. The error bar represents standard error of experiments three times per condition.

Overall, a higher initial surface temperature does not lead to a greater surface temperature change all the time. As  $T_s$  is increased, the cooling temperature increases at first and then decreases. When  $T_s = 100$  and  $200^\circ\text{C}$ , the typical drop impact dynamic is spreading and the surface temperature changes are almost the same between different  $We$  for the same initial  $T_s$ , but  $|\Delta T_s|$  shows an increasing trend as  $T_s$  increases from  $100$  to  $200^\circ\text{C}$ . This would imply the typical spreading process observed for  $We = 1.6, 27, 129$  yields similar cooling for the same  $T_s$  ( $= 100$  or  $200^\circ\text{C}$ ).

Starting from  $T = 300^\circ\text{C}$ , the effect of  $We$  on the cooling temperature is noticeable; generally a higher  $We$  leads to a greater temperature change,  $|\Delta T_s|$ . This can be explained by that a higher  $We$  droplet usually results in a wider contact area between droplet and surface, so more heat transfer rate occurs. Intriguingly, for low- $We$  ( $= 1.6$ ), insignificant cooling temperature ( $|\Delta T_s| \approx 3^\circ\text{C}$ ) is measured for  $350^\circ\text{C} < T_s < 500^\circ\text{C}$  due to droplet's complete rebound stem from the Leidenfrost effect [68]. During this completely rebound

process, because the vapor layer formed underneath the droplet keeps droplet from direct contact with the heated surface, little heat transfer occurs from surface to water. Hence, the surface temperature remains nearly constant.

## 4.4 Summary

In this chapter, we discuss various water drop impact dynamics observed on the heated quartz glass surface in a phase diagram under various  $We$  and  $T_s$ . Typical events observed include spreading, spreading with atomization, and splashing break up with atomization as  $T_s$  is increased from 100 to 450 °C for  $We \geq 1.6$ . Intriguing total rebound is observed at high  $T_s$  ( $> 350$  °C) but low  $We$  ( $< 10$ ) due to the Leidenfrost effect as an insulating vapor layer is formed underneath the droplet on a superheated surface.

In high temperature region ( $T_s \geq 350^\circ\text{C}$ ), impact dynamics varies more significantly by increasing  $We$ . Moreover, at  $T_s = 350^\circ\text{C}$  we start to observe Leidenfrost effect, so our dynamic Leidenfrost point is found between  $300^\circ\text{C}$  and  $350^\circ\text{C}$ . We further focus on heat transfer and temperature change during the drop impact process. The droplet temperature is analyzed by IR camera results and compared to a theoretical model introduced by Castanet et al. [87]. At low surface temperature region ( $T_s = 100^\circ\text{C}$ ), the experimental results show good agreement with the model but discrepancy for high temperature region ( $T_s \geq 300^\circ\text{C}$ ).

The violent droplet motion makes it difficult to analyze droplet contact diameter and temperature accurately, so both experimental and theoretical results have errors. In addition to improving experimental methods and tools, it is desirable to simplify droplet temperature by changing the equation in the future by including static parameters or dynamical parameters that are easier to measure. The surface temperature changing  $|\Delta T_s|$  analysis is based on the thermocouple results. When  $T_s$  increases, the surface temperature change increases in the low- $T_s$  regime but decreases in the high- $T_s$  regime.

As the similar drop impact dynamics (spreading) and contact diameter observed at low- $T_s$ , the more considerable difference between droplet and surface results in more significant surface temperature change,  $|\Delta T_s|$ . However, when impact dynamics are different, the con-

tact area and contact time may govern the surface temperature change. Therefore, research on the temperature changes of the drop and surface needs more systematic and accurate temperature measurements, particularly in the high- $T_s$  regime, while our results show good agreement for the low- $T_s$  regime (see Fig. 4.4).

## Chapter 5

# Conclusions and Outlook

### 5.1 Conclusions

In this thesis work, water drop impact on solid surfaces problem has been analyzed numerically and experimentally by varying different control parameters, particularly focusing on the effects of impact velocity, surface wettability, and surface temperature. First, a numerical model is built to simulate impact problems on unheated flat surfaces, emphasizing the velocity and wettability effect. The corresponding  $We$  varies from 4 to 510, and three kinds of surfaces are studied (hydrophilic, hydrophobic, and ultrahydrophobic surfaces). Navier-Stokes equations are the governing equations in the mathematical model, and we use a level-set method to track the interface between liquid and air. Our numerical model successfully reproduces almost all the dynamic events as the experimental results, especially with good agreement at the low- $We$  ( $< 30$ ) regime. We find that the slip length  $b$ , accounting for the friction force exerted on the droplet by the flat solid surface, is a key factor to control the dissipation and thus affects the impact dynamics and should be varied as the surface wettability changes in the model. The velocity and pressure fields, which are challenging to obtain with experiments, under various parameters are revealed by our numerical results and provide insights into different impact dynamics and outcomes observed. The primary outcomes observed include spreading, rebound, jetting, and splashing as the impact velocity

$V_I$  increases. When  $V_I$ , and hence kinetic energy, is increased, the impact dynamics changes from deposition/spreading ( $V_I = 0.35$  m/s) to splashing ( $V_I = 3$  m/s) on both hydrophilic and hydrophobic surfaces. A totally rebound is observed on ultrahydrophobic surface at  $V_I < 1.5$  m/s, but splashing at  $V_I = 2.5$  m/s. At moderate impact velocity ( $1$  m/s  $< V_I < 2$  m/s), jetting and bubble entrapment are observed for all surfaces, with negative pressure at the center during rapid recoiling of drop lamella. During a droplet rebound, air from the top and side fills the gaps underneath, while the droplet carries surrounding air moving upwards during a jetting event. In our explored parameter range, most simulation results show a scaling law between the spreading factor and Weber number,  $\beta \sim We^{1/4}$ , especially on hydrophobic and ultrahydrophobic flat surfaces.

We further investigate the impact dynamics on a heated flat surface experimentally. Using a high-speed camera and an Infrared (IR) camera, the entire ultrafast impact process is observed, and the temperature field is recorded as well. With the increase of surface temperature  $T_s$  (100°C to 450°C) and  $We$  (1.6 to 129), four typical regimes: spreading, totally rebound, spreading with atomization, and splashing breakup with atomization are observed experimentally, and a phase diagram is established to help understand the triggering conditions by the surface temperature  $T_s$  and  $We$ . The Leidenfrost effect was observed to be  $T_s \geq 350^\circ\text{C}$  at low  $We$  ( $1.6 < We < 4.5$ ), implying the dynamic Leidenfrost point ( $T_L^D$ ) in the range of 300°C to 350°C. The vapor film formed underneath the drop hinders heat transfer between the liquid and heated solid. The droplet temperature does not change during the impact, and the dynamic outcome is a total rebound. Based on the IR camera results, the droplet temperature has been analyzed and compared with a theoretical model introduced by Castanet et al. [87] considering the energy equation with a lubrication flow inside the spreading drop and thermal boundary layer. Our experimental results droplet temperature change at low surface temperature ( $T_s = 100^\circ\text{C}$ ) shows good agreement with the theoretical predictions. However, violent fluid motion at high temperature hinders clear high-speed IR images for accurate analysis. Therefore, the surface temperature is measured by the embedded thermocouple, and the difference  $|\Delta T_s|$  is analyzed within two seconds after impact.

As  $T_s$  increases, the surface temperature change increases in the low  $T_s$  region and then decreases in the high  $T_s$  region. The impact outcome of a total droplet rebound leads to negligible  $|\Delta T_s|$  due to an insulating vapor layer. In contrast, spreading (at  $T_s = 200^\circ\text{C}$ ) results in relatively large surface cooling ( $\approx 30^\circ\text{C}$ ) due to a larger contact area and longer contact time of the spreading lamella on the surface.

## 5.2 Future work

We have found many relevant topics worthy of further investigations during the research and some improvement that can be made, based on our current results. The numerical simulations of drop impact on a flat unheated surface, first utilizing dynamic contact angle, which requires experimental measurements, might provide more agreeable results of impact dynamics to real experimental situations. Second, since the numerical model is helpful to simulate high-speed impact, an investigation of splashing threshold can be conducted on surfaces with different wettability and roughness. Third, the design of complex surfaces in numerical simulations will be helpful to understand impact regimes with different surface structures, wettability, and roughness. Fourth, the properties of liquid can be easily modified by tuning some key parameters (such as density, viscosity, and surface tension) to simulate complex fluids. In general, one of the essential advantages of numerical simulation models is that it is relatively easy to adjust the parameters and thus change the properties. It is even possible to simulate scenarios that are difficult to achieve experimentally in practice. Various influences of liquid properties and surface characteristics, particularly roughness, on drop impact dynamics can be investigated in the future to provide a better understanding of roughness effects.

For the experimental investigations of drop impact on a heated surface, the design of the experiment on heated surfaces could be improved that enable equipment to record the temperature field more accurately. For example, one can employ at least two tools to measure the specific temperature of a single object that the error is known by comparison and then controlled. The dynamic Leidenfrost point can be analyzed more systematically to a more

precise value in the future. Besides temperature field and  $T_L^D$ , some other quantities are of interest, for instance, the critical Weber number  $We_c$  for the droplet disintegration. It has been reported that surface temperature affects  $We_c$  required for shattering a droplet [9], and hence a specific empirical correlation can be obtained with experiments.

Furthermore, the Leidenfrost effect and residence time of drop, defined as the duration from first contact with to first bounce from the wall, have attracted recent interest [9]. Although some correlations between the residence time and droplet size (or  $We$ ) are found, there is no universal law found for most fluids and various cases. The thickness of the Leidenfrost vapor film created between the droplet and surface is worthy of further investigations using an advanced method such as reflection interference microscopy (RIM).

# References

- [1] R Andrade, O Skurtys, and F Osorio. Drop impact behavior on food using spray coating: Fundamentals and applications. *Food Res. Int.*, 54(1):397–405, 2013.
- [2] W Jia and H-H Qiu. Experimental investigation of droplet dynamics and heat transfer in spray cooling. *Exp. Therm Fluid Sci.*, 27(7):829–838, 2003.
- [3] EW Collings, AJ Markworth, JK McCoy, and JH Saunders. Splat-quench solidification of freely falling liquid-metal drops by impact on a planar substrate. *J. Mater. Sci.*, 25(8):3677–3682, 1990.
- [4] B Derby. Inkjet printing ceramics: From drops to solid. *J. Eur. Ceram. Soc.*, 31(14):2543–2550, 2011.
- [5] G Grant, J Brenton, and D Drysdale. Fire suppression by water sprays. *Prog. Energy Combust. Sci.*, 26(2):79–130, 2000.
- [6] A. L. Yarin. Drop impact dynamics: Splashing, spreading, receding, bouncing.. *Annu. Rev. Fluid Mech.*, 38:159–192, 2006.
- [7] Christophe Josserand and Sigurdur T Thoroddsen. Drop impact on a solid surface. *Annu. Rev. Fluid Mech.*, 48:365–391, 2016.
- [8] Carlo Antonini, Alidad Amirfazli, and Marco Marengo. Drop impact and wettability: From hydrophilic to superhydrophobic surfaces. *Phys. Fluids*, 24(10), 2012.
- [9] Gangtao Liang and Issam Mudawar. Review of drop impact on heated walls. *Int. J. Heat Mass Transf.*, 106:103–126, 2017.
- [10] Yuehua Yuan and T Randall Lee. Contact angle and wetting properties. In *Surface science techniques*, pages 3–34. Springer, 2013.

- [11] Thomas Young. Iii. an essay on the cohesion of fluids. *Philos. Trans. R. Soc. London*, (95):65–87, 1805.
- [12] Daniel Y Kwok and August W Neumann. Contact angle measurement and contact angle interpretation. *Adv. Colloid Interface Sci.*, 81(3):167–249, 1999.
- [13] Lasse Makkonen. Young’s equation revisited. *J. Phys.: Condens. Matter*, 28(13):135001, 2016.
- [14] Arthur Mason Worthington. Xxviii. on the forms assumed by drops of liquids falling vertically on a horizontal plate. *Proc. R. Soc. London*, 25(171-178):261–272, 1877.
- [15] Romain Rioboo, Cameron Tropea, and Marco Marengo. Outcomes from a drop impact on solid surfaces. *Atomization Sprays*, 11(2), 2001.
- [16] Hiromi Minemawari, Toshikazu Yamada, Hiroyuki Matsui, Jun’ya Tsutsumi, Simon Haas, Ryosuke Chiba, Reiji Kumai, and Tatsuo Hasegawa. Inkjet printing of single-crystal films. *Nature*, 475(7356):364–367, 2011.
- [17] Lee Hulse-Smith, Navid Z Mehdizadeh, and Sanjeev Chandra. Deducing drop size and impact velocity from circular bloodstains. *J. Forensic Sci.*, 50(1):JFS2003224–10, 2005.
- [18] Jun Fukai, Z Zhao, Dimos Poulikakos, Constantine M Megaridis, and O Miyatake. Modeling of the deformation of a liquid droplet impinging upon a flat surface. *Phys. Fluids A*, 5(11):2588–2599, 1993.
- [19] Martin Rein. Phenomena of liquid drop impact on solid and liquid surfaces. *Fluid Dyn. Res.*, 12(2):61–93, 1993.
- [20] Brian L Scheller and Douglas W Bousfield. Newtonian drop impact with a solid surface. *AIChE J.*, 41(6):1357–1367, 1995.
- [21] M Pasandideh-Fard, YM Qiao, Sanjeev Chandra, and Javad Mostaghimi. Capillary effects during droplet impact on a solid surface. *Phys. Fluids*, 8(3):650–659, 1996.
- [22] Chijioke Ukiwe and Daniel Y Kwok. On the maximum spreading diameter of impacting droplets on well-prepared solid surfaces. *Langmuir*, 21(2):666–673, 2005.
- [23] Christophe Clanet, Cédric Béguin, Denis Richard, and David Quéré. Maximal defor-

- mation of an impacting drop. *J. Fluid Mech.*, 517:199, 2004.
- [24] Jens Eggers, Marco A Fontelos, Christophe Josserand, and Stéphane Zaleski. Drop dynamics after impact on a solid wall: theory and simulations. *Phys. Fluids*, 22(6):062101, 2010.
- [25] Ilia V Roisman, Andreas Lembach, and Cameron Tropea. Drop splashing induced by target roughness and porosity: The size plays no role, 2015.
- [26] S Chandra and CT Avedisian. On the collision of a droplet with a solid surface. *Proc. R. Soc. London, Ser. A*, 432(1884):13–41, 1991.
- [27] Daniel A Bolleddula. *Droplet impact and spreading of viscous dispersions and volatile solutions*. University of Washington, 2011.
- [28] Nick Laan, Karla G de Bruin, Denis Bartolo, Christophe Josserand, and Daniel Bonn. Maximum diameter of impacting liquid droplets. *Phys. Rev. Appl.*, 2(4):044018, 2014.
- [29] J Madejski. Solidification of droplets on a cold surface. *Int. J. Heat Mass Transfer*, 19(9):1009–1013, 1976.
- [30] Ilia V Roisman, Romain Rioboo, and Cameron Tropea. Normal impact of a liquid drop on a dry surface: model for spreading and receding. *Proc. R. Soc. London, Ser. A*, 458(2022):1411–1430, 2002.
- [31] Denis Bartolo, Christophe Josserand, and Daniel Bonn. Retraction dynamics of aqueous drops upon impact on non-wetting surfaces. *J. Fluid Mech.*, 545:329–338, 2005.
- [32] Denis Richard, Christophe Clanet, and David Quéré. Contact time of a bouncing drop. *Nature*, 417(6891):811–811, 2002.
- [33] T Bennett and D Poulidakos. Splat-quench solidification: estimating the maximum spreading of a droplet impacting a solid surface. *J. Mater. Sci.*, 28(4):963–970, 1993.
- [34] Peichun Tsai, Maurice HW Hendrix, Remko RM Dijkstra, Lingling Shui, and Detlef Lohse. Microscopic structure influencing macroscopic splash at high weber number. *Soft Matter*, 7(24):11325–11333, 2011.
- [35] Ilia V Roisman. Inertia dominated drop collisions. ii. an analytical solution of the navier–stokes equations for a spreading viscous film. *Phys. Fluids*, 21(5):052104, 2009.

- [36] CHR Mundo, M Sommerfeld, and C Tropea. Droplet-wall collisions: experimental studies of the deformation and breakup process. *Int. J. Multiphase Flow*, 21(2):151–173, 1995.
- [37] Randy L. Vander Wal, Gordon M. Berger, and Steven D. Mozes. The splash/non-splash boundary upon a dry surface and thin fluid film. *Exp. Fluids*, 40(1):53–59, 2006.
- [38] Sigurdur T Thoroddsen, M-J Thoraval, K Takehara, and TG Etoh. Droplet splashing by a slingshot mechanism. *Phys. Rev. Lett.*, 106(3):034501, 2011.
- [39] Marco Marengo, Carlo Antonini, Ilia V Roisman, and Cameron Tropea. Drop collisions with simple and complex surfaces. *Curr. Opin. Colloid Interface Sci.*, 16(4):292–302, 2011.
- [40] Shreyas Mandre, Madhav Mani, and Michael P Brenner. Precursors to splashing of liquid droplets on a solid surface. *Phys. Rev. Lett.*, 102(13):134502, 2009.
- [41] Michelle M Driscoll and Sidney R Nagel. Ultrafast interference imaging of air in splashing dynamics. *Phys. Rev. Lett.*, 107(15):154502, 2011.
- [42] Guillaume Riboux and José Manuel Gordillo. Experiments of drops impacting a smooth solid surface: a model of the critical impact speed for drop splashing. *Phys. Rev. Lett.*, 113(2):024507, 2014.
- [43] Miguel A Quetzeri-Santiago, Kensuke Yokoi, Alfonso A Castrejón-Pita, and J Rafael Castrejón-Pita. Role of the dynamic contact angle on splashing. *Phys. Rev. Lett.*, 122(22):228001, 2019.
- [44] Prashant R Gunjal, Vivek V Ranade, and Raghunath V Chaudhari. Dynamics of drop impact on solid surface: experiments and vof simulations. *AIChE J.*, 51(1):59–78, 2005.
- [45] Sang Hyuk Lee, Nahmkeon Hur, and Seongwon Kang. A numerical analysis of drop impact on liquid film by using a level set method. *J. Mech. Sci. Technol.*, 25(10):2567, 2011.
- [46] X Li, N Massarotti, P Nithiarasu, Bahni Ray, Gautam Biswas, Ashutosh Sharma, and Samuel WJ Welch. Clsvof method to study consecutive drop impact on liquid pool.

*Int. J. Numer. Methods Heat Fluid Flow*, 2013.

- [47] Shiladitya Mukherjee and John Abraham. Investigations of drop impact on dry walls with a lattice-boltzmann model. *J. Colloid Interface Sci.*, 312(2):341–354, 2007.
- [48] Claas Willem Visser, Philipp Erhard Frommhold, Sander Wildeman, Robert Mettin, Detlef Lohse, and Chao Sun. Dynamics of high-speed micro-drop impact: numerical simulations and experiments at frame-to-frame times below 100 ns. *Soft Matter*, 11(9):1708–1722, 2015.
- [49] Jae Bong Lee, Dominique Derome, Ali Dolatabadi, and Jan Carmeliet. Energy budget of liquid drop impact at maximum spreading: Numerical simulations and experiments. *Langmuir*, 32(5):1279–1288, 2016.
- [50] S Oukach, M Elganaoui, B Pateyron, and H Hamdi. Deformation behavior of a liquid droplet impacting a solid surface. In *Proc. COMSOL Conf.*, pages 2–7, 2010.
- [51] Kensuke Yokoi, Damien Vadillo, John Hinch, and Ian Hutchings. Numerical studies of the influence of the dynamic contact angle on a droplet impacting on a dry surface. *Phys. Fluids*, 21(7):072102, 2009.
- [52] Jin Sun, Qi Liu, Yunhong Liang, Zhaohua Lin, and Chunbao Liu. Three-dimensional vof simulation of droplet impacting on a superhydrophobic surface. *Bio-Des. Manuf.*, 2(1):10–23, 2019.
- [53] Michael Griebel and Margrit Klitz. Simulation of micron-scale drop impact. *Comput. Math. Appl.*, 78(9):3027–3043, 2019.
- [54] Rui Zhang, Samaneh Farokhirad, Taehun Lee, and Joel Koplik. Multiscale liquid drop impact on wettable and textured surfaces. *Phys. Fluids*, 26(8):082003, 2014.
- [55] Siddhartha F. Lunkad, Vivek V. Buwa, and K. D.P. Nigam. Numerical simulations of drop impact and spreading on horizontal and inclined surfaces. *Chem. Eng. Sci.*, 62(24):7214–7224, 2007.
- [56] Xin Wang, Dong-Liang Sun, Xiao-Dong Wang, and Wei-Mon Yan. Dynamics of droplets impacting hydrophilic surfaces decorated with a hydrophobic strip. *Int. J. Heat Mass Transfer*, 135:235–246, 2019.

- [57] Kuo-Long Pan, Kun-Cheng Tseng, and Ching-Hua Wang. Breakup of a droplet at high velocity impacting a solid surface. *Exp. Fluids*, 48(1):143–156, 2010.
- [58] E Klaseboer, J Ph Chevaillier, C Gourdon, and Olivier Masbernat. Film drainage between colliding drops at constant approach velocity: experiments and modeling. *J. Colloid Interface Sci.*, 229(1):274–285, 2000.
- [59] John M Kolinski, Shmuel M Rubinstein, Shreyas Mandre, Michael P Brenner, David A Weitz, and L Mahadevan. Skating on a film of air: drops impacting on a surface. *Phys. Rev. Lett.*, 108(7):074503, 2012.
- [60] Jolet De Ruiter, Rudy Lagraauw, Dirk Van Den Ende, and Frieder Mugele. Wettability-independent bouncing on flat surfaces mediated by thin air films. *Nat. Phys.*, 11(1):48–53, 2015.
- [61] Dashu Li, Duo Zhang, Zhiwei Zheng, and Xiaoshuai Tian. Numerical analysis on air entrapment during a droplet impacts on a dry flat surface. *Int. J. Heat Mass Transfer*, 115:186–193, 2017.
- [62] Wilco Bouwhuis, Roeland CA van der Veen, Diederik L Tuan Tran, Koen G Keij, Ivo R Winkels, Devaraj van der Meer Peters, Chao Sun, Jacco H Snoeijer, and Detlef Lohse. Maximal air bubble entrainment at liquid-drop impact. *Phys. Rev. Lett.*, 109(26):264501, 2012.
- [63] John D Bernardin, Clinton J Stebbins, and Issam Mudawar. Mapping of impact and heat transfer regimes of water drops impinging on a polished surface. *Int. J. Heat Mass Transf.*, 40(2):247–267, 1997.
- [64] GE Cossali, Marco Marengo, and Maurizio Santini. Secondary atomisation produced by single drop vertical impacts onto heated surfaces. *Exp. Therm Fluid Sci.*, 29(8):937–946, 2005.
- [65] GE Cossali, M Marengo, and M Santini. Thermally induced secondary drop atomisation by single drop impact onto heated surfaces. *Int. J. Heat Fluid Flow*, 29(1):167–177, 2008.
- [66] Tuan Tran, Hendrik J.J. Staat, Andrea Prosperetti, Chao Sun, and Detlef Lohse. Drop

- impact on superheated surfaces. *Phys. Rev. Lett.*, 108(3):2–5, 2012.
- [67] Hendrik J.J. Staat, Tuan Tran, Bart Geerdink, Guillaume Riboux, Chao Sun, José Manuel Gordillo, and Detlef Lohse. Phase diagram for droplet impact on superheated surfaces. *J. Fluid Mech.*, 779:1–12, 2015.
- [68] Johann Gottlob Leidenfrost. On the fixation of water in diverse fire. *Int. J. Heat Mass Transf.*, 9(11):1153–1166, 1966.
- [69] Fabian M. Tenzer, Julian Hofmann, Ilia V. Roisman, and Cameron Tropea. Leidenfrost temperature in sprays: role of the substrate and liquid properties. *arXiv preprint arXiv:2001.05426*, pages 1–9, 2020.
- [70] David Quéré. Leidenfrost dynamics. *Annu. Rev. Fluid Mech.*, 45:197–215, 2013.
- [71] Anne Laure Biance, Christophe Clanet, and David Quéré. Leidenfrost drops. *Phys. Fluids*, 15(6):1632–1637, 2003.
- [72] J D Bernardin and I Mudawar. The Leidenfrost Point: Experimental Study and Assessment of Existing Models. *J. Heat Transfer*, 121(4):894–903, 1999.
- [73] Seol Ha Kim, Ho Seon Ahn, Joonwon Kim, Massoud Kaviani, and Moo Hwan Kim. Dynamics of water droplet on a heated nanotubes surface. *Appl. Phys. Lett.*, 102(23):233901, 2013.
- [74] Corey Kruse, Troy Anderson, Chris Wilson, Craig Zuhlke, Dennis Alexander, George Gogos, and Sidy Ndao. Extraordinary shifts of the Leidenfrost temperature from multiscale micro/nanostructured surfaces. *Langmuir*, 29(31):9798–9806, 2013.
- [75] M Auliano, D Auliano, M Fernandino, P Zhang, and C A Dorao. Water droplet dynamics on a heated nanowire surface. *Appl. Phys. Lett.*, 113(25):253703, 2018.
- [76] Hyuk-min Kwon, James C Bird, and Kripa K Varanasi. Increasing leidenfrost point using micro-nano hierarchical surface structures. *Appl. Phys. Lett.*, 103(20):201601, 2013.
- [77] Seol Ha Kim, Gicheol Lee, HyungMo Kim, and Moo Hwan Kim. Leidenfrost point and droplet dynamics on heated micropillar array surface. *Int. J. Heat Mass Transf.*, pages 1–9, 2019.

- [78] Daniel Arnaldo del Cerro, Álvaro G Marín, Gertwillem R B E Römer, B Pathiraj, Detlef Lohse, and Albertus J Huis in 't Veld. Leidenfrost Point Reduction on Micropatterned Metallic Surfaces. *Langmuir*, 28(42):15106–15110, 2012.
- [79] Il Woong Park, Maria Fernandino, and Carlos Albert Dorao. Effect of Micropillar Characteristics on Leidenfrost Temperature of Impacting Droplets. In *ASME 2016 14th Int. Conf. Nanochannels, Microchannels, Minichannels collocated with ASME 2016 Heat Transf. Summer Conf. ASME 2016 Fluids Eng. Div. Summer Meet.*, page V001T09A001. American Society of Mechanical Engineers, 2016.
- [80] Shi-Chune Yao and Kang Yuan Cai. The dynamics and leidenfrost temperature of drops impacting on a hot surface at small angles. *Exp. Therm Fluid Sci.*, 1(4):363–371, 1988.
- [81] Gian Piero Celata, Maurizio Cumo, Andrea Mariani, and Giuseppe Zummo. Visualization of the impact of water drops on a hot surface: effect of drop velocity and surface inclination. *Heat Mass Transfer*, 42(10):885–890, 2006.
- [82] V Bertola and K Sefiane. Controlling secondary atomization during drop impact on hot surfaces by polymer additives. *Phys. Fluids*, 17(10):108104, 2005.
- [83] Hrudya Nair, Hendrik JJ Staat, Tuan Tran, Arie van Houselt, Andrea Prosperetti, Detlef Lohse, and Chao Sun. The leidenfrost temperature increase for impacting droplets on carbon-nanofiber surfaces. *Soft Matter*, 10(13):2102–2109, 2014.
- [84] Dong Eok Kim. Dynamic Leidenfrost temperature behaviors on uniformly distributed micropillars. *Exp. Therm. Fluid Sci.*, 111:109954, 2020.
- [85] Tuan Tran, Hendrik JJ Staat, Arturo Susarrey-Arce, Tobias C Foertsch, Arie van Houselt, Han JGE Gardeniers, Andrea Prosperetti, Detlef Lohse, and Chao Sun. Droplet impact on superheated micro-structured surfaces. *Soft Matter*, 9(12):3272–3282, 2013.
- [86] Samira Shiri and James C Bird. Heat exchange between a bouncing drop and a superhydrophobic substrate. *Proc. Natl. Acad. Sci. U.S.A.*, 114(27):6930–6935, 2017.
- [87] G. Castanet, W. Chaze, O. Caballina, R. Collignon, and F. Lemoine. Transient evolu-

- tion of the heat transfer and the vapor film thickness at the drop impact in the regime of film boiling. *Phys. Fluids*, 30(12), 2018.
- [88] Chunfang Guo, Daniel Maynes, Julie Crockett, and Danyang Zhao. Heat transfer to bouncing droplets on superhydrophobic surfaces. *Int. J. Heat Mass Transfer*, 137:857–867, 2019.
- [89] Solomon Adera, Rishi Raj, Ryan Enright, and Evelyn N Wang. Non-wetting droplets on hot superhydrophilic surfaces. *Nat. Commun.*, 4(1):1–7, 2013.
- [90] Guillaume Riboux and José Manuel Gordillo. The diameters and velocities of the droplets ejected after splashing. *J. Fluid Mech*, 772:630–648, 2015.
- [91] Qiang Meng, Yali Zhang, Jiang Li, Rob GH Lammertink, Haosheng Chen, and Peichun Amy Tsai. Altering emulsion stability with heterogeneous surface wettability. *Sci. Rep.*, 6(1):1–8, 2016.
- [92] Nadia Shardt, Masoud Bozorg Bigdeli, Janet A.W. Elliott, and Peichun Amy Tsai. How Surfactants Affect Droplet Wetting on Hydrophobic Microstructures. *J. Phys. Chem. Lett.*, 10(23):7510–7515, 2019.
- [93] Ahmed Aldhaleai, Faheem Khan, Thomas Thundat, and Peichun Amy Tsai. Evaporation dynamics of water droplets on superhydrophobic nanoglass surfaces. *Int. J. Heat Mass Transf.*, 160:42–47, 2020.
- [94] Cyril Duez, Christophe Ybert, Christophe Clanet, and Lyderic Bocquet. Making a splash with water repellency. *Nat. Phys.*, 3(3):180–183, 2007.
- [95] Peichun Tsai, Alisia M. Peters, Christophe Pirat, Matthias Wessling, Rob G.H. Lammertink, and Detlef Lohse. Quantifying effective slip length over micropatterned hydrophobic surfaces. *Phys. Fluids*, 21(11):1–8, 2009.
- [96] Benzhong Zhao, Christopher W. MacMinn, and Ruben Juanes. Wettability control on multiphase flow in patterned microfluidics. *Proc. Natl. Acad. Sci. U. S. A.*, 113(37):10251–10256, 2016.
- [97] Marzieh Saadat, Junyi Yang, Marcin Dudek, Gisle Øye, and Peichun Amy Tsai. Microfluidic investigation of enhanced oil recovery: The effect of aqueous floods and

- network wettability. *J. Pet. Sci. Eng.*, 203, 2021.
- [98] Christopher E. Brennen. *Fundamentals of multiphase flow*. Cambridge university press, 2005.
- [99] Dashu Li, Zhiwei Zheng, and Xiaoshuai Tian. Numerical analysis on air entrapment during a droplet impacts on a dry flat surface. *Int. J. Heat Mass Transfer*, 115:186–193, 2017.
- [100] Roger Temam. *Navier-Stokes equations: theory and numerical analysis.*, volume 343. American Mathematical Society, 2001.
- [101] Stanley Osher and Ronald Fedkiw. *Level Set Methods and Dynamic Implicit Surfaces*, volume 153. Springer Science & Business Media, 2006.
- [102] Elin Olsson and Gunilla Kreiss. A conservative level set method for two phase flow. *J. Comput. Phys.*, 210(1):225–246, 2005.
- [103] COMSOL Inc. Comsol multiphysics reference manual, version 5.5, 2019.
- [104] Bruno Goffinet. Daniel Wallach. Mean squared error of prediction as a criterion for evaluating and comparing system models. *Ecol. Modell.*, 44(3-4):299–306, 1989.
- [105] Yisen Guo, Yongsheng Lian, and Mark Sussman. Investigation of drop impact on dry and wet surfaces with consideration of surrounding air. *Phys. Fluids*, 28(7), 2016.
- [106] R. Rioboo, M. Marengo, and C. Tropea. Time evolution of liquid drop impact onto solid, dry surfaces. *Exp. Fluids*, 33(1):112–124, 2002.
- [107] Laurent Courbin, James C Bird, Mathilde Reyssat, and HA Stone. Dynamics of wetting: from inertial spreading to viscous imbibition. *J. Phys.: Condens. Matter*, 21(46):464127, 2009.
- [108] Jen-Hong Tan, EYK Ng, U Rajendra Acharya, and Caroline Chee. Infrared thermography on ocular surface temperature: a review. *Infrared Phys. Technol.*, 52(4):97–108, 2009.
- [109] FLIR Systems Inc. Temperature linear mode. [https://flir.custhelp.com/app/answers/detail/a\\_id/1021/~temperature-linear-mode](https://flir.custhelp.com/app/answers/detail/a_id/1021/~temperature-linear-mode).
- [110] An-Bang Wang, Chih-Hung Lin, and Chi-Chang Chen. The critical temperature of dry

- impact for tiny droplet impinging on a heated surface. *Phys. Fluids*, 12(6):1622–1625, 2000.
- [111] Jan Breitenbach, Ilia V Roisman, and Cameron Tropea. Heat transfer in the film boiling regime: Single drop impact and spray cooling. *Int. J. Heat Mass Transfer*, 110:34–42, 2017.
- [112] Alexander L Yarin and Daniel A Weiss. Impact of drops on solid surfaces: self-similar capillary waves, and splashing as a new type of kinematic discontinuity. *J. Fluid Mech.*, 283:141–173, 1995.
- [113] R Kannan and D Sivakumar. Drop impact process on a hydrophobic grooved surface. *Colloids Surf., A*, 317(1-3):694–704, 2008.
- [114] R Rioboo, M Voué, A Vaillant, and J De Coninck. Drop impact on porous superhydrophobic polymer surfaces. *Langmuir*, 24(24):14074–14077, 2008.